Développement du modèle d'ion polarisable pour la modélisation de BaTiO3

Cintia Hartmann

To cite this version:

Cintia Hartmann. Développement du modèle d'ion polarisable pour la modélisation de BaTiO3. Autre. Université Paris Saclay (COmUE), 2018. Français. NNT : 2018SACLC012 . tel-02144323

HAL Id: tel-02144323
https://theses.hal.science/tel-02144323

Submitted on 30 May 2019

université
PARIS-SACLAY

CentraleSupélec

NNT : 2018SACLC012

Thèse de doctorat

Development of a polarizable ion model for Barium Titanate

Thèse de doctorat de l'Université Paris-Saclay
préparée à CentraleSupelec

École doctorale n°(573) Interfaces : approches interdisciplinaires, fondements, applications et innovation
Spécialité de doctorat: Physique

Thèse présentée et soutenue à Gif-sur-Yvette, le 26.01.2018, par

Cintia Hartmann

Composition du Jury :

Grégory Geneste Chercheur CEA HDR, CEA/DAM, DIF	Président
Xavier Rocquefelte Professeur, Institut des Sciences Chimiques de Rennes (UMR 6226)	Rapporteur
Rodolphe Vuilleumier Professeur, ENS - Département de chimie (UMR 8640)	Rapporteur
Guilhem Dezanneau Statut, Laboratoire SPMS, Centralesupelec (UMR CNRS 8580)	Directeur de thèse
Mathieu Salanne Professeur, Université Pierre et Marie Curie (UMR 8234)	Invité
Igor Kornev Professeur, Laboratoire SPMS, Centralesupelec (UMR CNRS 8580)	Invité

À mon père

Remerciements

Tout d'abord un grand remerciement va à mon directeur de thèse pour son soutien au cours de ces dernières années sur le plan scientifique et humain. Il a su me donner de très bons conseils dans des moments difficiles qui montrent une grande expérience de la vie. Je tiens également à remercier vivement Mathieu Salanne qui mérite une profonde gratitude pour son initiation dans le modèle d'ion polarisables, et pour ses innombrables discussions d'une aide très précieuse et son grand engagement. De même je tiens à remercier chaleureusement Igor Kornev pour ses discussions pertinentes. J'adresse également mes remerciements aux deux rapporteurs, Rodolphe Vuilleumier et Xavier Rocquefelte, pour avoir accepté ce travail. Au même titre un grand merci à Grégory Geneste pour la fonction de président de jury. Merci également aux membres de ma famille pour leurs encouragements et leur soutien ; à mes collègues formidables du laboratoire SPMS et PHENIX sans qui l'atmosphère de travail n'aurait pas été aussi agréable. Je remercie tous mes amis en dehors du contexte de travail pour leur soutien de près ou de loin !

Contents

Nomenclature

AIM	Aspherical Ion Model
$BaTiO_3$	Barium titanate
BZ	Brillouin Zone
B1-WC	hybrid functional of Bilc et al. [1]
B3LYP	Becke, 3-parameter, Lee-Yang-Parr
CASTEP	Cambridge Serial Total Energy Package
CLUS	cation shell density
CRYS	Point charge crystal lattice on the anion polarizability
DAIM	Dipolar Aspherical Ion Model
DFT	Density Functional Theory
DIPPIM	Dipole Polarizable Ion Model
E_{XC}	exchange energy
FF	force field
FREE	free state
GGA	Generalized Gradient Approximation
Heff	effective Hamiltonian
HSE	Heyd-Scuseria-Ernzerhof
HSE06	modified HSE functional [2]
KS	Kohn-Sham
LDA	Local Density Approximation
LO	longitudinal optical mode
MC	Monte Carlo
MD	Molecular Dynamics
MIGRAD	minimizer algorithms implemented in MINUIT
MINUIT	numerical minimization computer program [3]
MLWF	Maximally Localized Generalized Wannier Function
MP	Monkhorst-Pack
NPT	constant moles and isothermal-isobaric ensemble
NVE	constant moles and isochore-adiabatic ensemble
NVT	constant moles and isochore-isothermic ensemble

PAW	Projector Augmented-wave method
PBE	Perdew, Burke, Ernzerhof
PBEsol	solid Perdew, Burke, Ernzerhof
PBE0	hybrid Perdew, Burke, Ernzerhof functional [4]
PIM	Polarizable Ion Model
RIM	Rigid Ion Model
SM	Shell Model
TO	transverse optical mode
UFF	Ultrathin Ferroelectric Films
VASP	Vienna Ab-Initio Simulation
WC	Wu-Cohen functional

Introduction

Since the discovery of ferroelectricity in 1920, ferroelectrics gained in attention because of their particular physical properties, which are of fundamental and industrial interest.

Ferroelectric crystals do not possess inversion symmetry and are characterized by having a spontaneous polarization that can be switched in direction by applying an electric field. The relationship between the macroscopic polarization and the applied electric field is non-linear and depends on the history, whose signature is the hysteresis loop. Furthermore, ferroelectrics are strongly coupled to stress and temperature, which lead to the piezoelectric and the pyroelectric effect. The range of technological applications for nano-scale is great because of the interplay between polarization, stress, electric field and temperature. For example, the non-linear behaviour between polarization and electric field is employed in tunable capacitors. The commonly high permittivity of ferroelectrics, in particular close to the phase transition temperature, makes ferroelectric capacitors small-sized compared to dielectric capacitors. The hysteresis is for instance used in ferroelectric-based memories (FeRAM). The piezoelectric effect can be used in sensors, in actuators or in resonant wave devices such as radio-frequency filters. The pyroelectric effect can be employed in infra-red detectors.

Complex ferroelectric based structures at nano-scale are desired for various technical applications. Therefore, it is of great interest to describe the relationship between the complex ferroelectric-based structures and the resulting physical properties. Thus, efficient numerical methods able to simulate complex ferroelectric structures are requested. In the current numerical methods limitations are observed: Density functional theory (DFT)-calculation are limited in time and length-scale; the effective Hamiltonian reduces the number of degrees of freedom making it hard to apply to complex structures; the Shell Model uses commonly non-physical core-shell charges making this type of interaction potentials less transferable.

The objective of this thesis is to develop a new family of interaction potentials for the ferroelectric materials based on the polarizable ion model (PIM). In the PIM the ions are treated as polarizable species with nominal charge. In comparison to current modelisation techniques, the use of nominal charges should facilitate the inclusion of various materials composition and the study of defect and surface effects. For a first step towards ferroelectric modeling with PIM, the focus lies on the development of an interaction potential for the prototype ferroelectric $BaTiO_3$. $BaTiO_3$ is the most widely studied ferroelectric of the family of perovskite structure of general formula of ABO_3. It undergoes by cooling three successive structural transitions from paraelectric cubic phase to ferroelectric tetragonal, orthorhombic and rhombohedral phase.

In the first chapter the state of the art of modelling ferroeletrics is presented by introducing the most common modelling methods going from first principle methods over the effective Hamiltonian approach and the Shell Model. For each method, its contribution to the advance in modelling ferroelectrics and its limitations are discussed, which motivate the development of PIM models for this class of materials. In the second chapter Polarizable Ion Model (PIM) is presented and the different terms of the interaction potential are explained. A particular emphasis is placed on how polarization effects in ionic materials are treated in this model. The in literature existent methods for the parametrization of the PIM model are described and explicitly presented through some literature examples. On the basis of these examples, additional insight into the quality and the possible range of application of PIM models is gained.

The third chapter deals with the development of a PIM model for $BaTiO_3$. The chapter is divided into two different parts. The first part concerns the reference DFT calculations and preliminary investigations to answer, if the use of nominal charged ions is meaningful for the modelling of ferroelectric $BaTiO_3$. The second part of the third chapter is dedicated to the parametrization of an interaction potential for $BaTiO_3$. A modified parametrization procedure is introduced that may reduce compensation errors during the fitting procedure. In the fourth chapter the quality of two developed models are investigated on a series of zero temperature properties. For the better of both models, further studies at finite temperature are carried out. The thesis is terminated with a conclusion about the work and possible prospects for the development of PIM models for ferroelectric materials.

Chapter 1

Barium Titanate Modelling

Contents

THIS chapter gives an introduction to the modelling techniques for $BaTiO_3$. In fact, modelling materials are of great interest, because the many-body Schrödinger equation that governs the dynamics of atoms in solids are unfortunately too complex for analytical resolution.

There exist two classes of modelling methods which have been successfully applied to $BaTiO_3$: first principle methods and second principle methods. First principle methods start from the fundamental interaction between electrons and nuclei and therefore require as input only chemical formula and atomic numbers of the elements of the material. First principle methods based on the Density Functional Theory (DFT) have been widely used for the study of ferroelectric materials. Second principle methods are based on first principle calculations and simplify the problem by focusing on effective interactions, that enables the reduction of the computational cost. These effective interactions depend on a set of parameters, which are derived from first principle calculations. The most popular methods are the effective Hamiltonian (Heff) and the Shell Model (SM). Both methods can calculate energies and forces that can then be coupled to other methods such as molecular dynamics (MD) and Monte Carlo (MC) simulations for finite temperature calculations. In this Chapter, first and second principle methods are presented and their efficiency is reviewed in the specific case of $BaTiO_3$ by highlighting their assets and drawbacks, which will conduct to the interest in an alternative model. The development of the alternative model, the Polarisable Ion Model (PIM), and its application to $BaTiO_3$ constitute the main objective of this thesis.

1.1 Density functional theory

In the framework of quantum mechanics, Density Functional Theory (DFT) is an approach that allows to determine the properties of many-body electron systems. In the first subsection, the Born-Oppenheimer approximation is presented. It allows separating the Schrödinger equation into two equations under two assumptions, one for the nuclei degrees of freedoms and the other for the electrons degrees of freedom. The many-electron equation can then be reformulated in terms of functionals by applying the Hohenberg-Kohn theorems, which form the basis of DFT and are the subject of the second subsection. Then the method of resolution introduced by Kohn-Sham (KS) is presented. It contains an universal functional, named Exchange-correlation functional, which is unknown and has to be approximated. In the third subsection, different approximations of this term are reviewed. In the last subsection, the results of DFT calculations applied to $BaTiO_3$ for different approximations of the Exchange-correlation functional are presented.

1.1.1 Born-Oppenheimer Approximation

The time-independent, non relativistic Schrödinger equation for a system of N_n nuclei and N_e electrons in interactions is given by:

$$\hat{H}\Psi = E\Psi \tag{1.1}$$

where E is the energy of the state Ψ and where the corresponding Hamiltonian $\hat{H}$ in atomic units is:

$$\hat{H} = -\sum_{A} \frac{1}{2M_A}\nabla_A^2 + \sum_{A<B} \frac{Z_A Z_B}{r_{AB}} - \sum_{i} \frac{1}{2}\nabla_i^2 - \sum_{i,A} \frac{Z_A}{r_{iA}} + \sum_{i>j} \frac{1}{r_{ij}}. \tag{1.2}$$

The suffixes A, B run over the N_n nuclei, while i, j refers to the N_e electrons with mass m. Z denotes the nuclear charge and M the nuclear mass. The first term is the kinetic energy operator of nuclei $\hat{T}_n$, the second term is the nuclear-nuclear interaction $\hat{V}_{nn}$. The third term is the electronic kinetic energy operator $\hat{T}_e$, the forth the electron-nuclear interaction $\hat{V}_{ne}$ and the last term the electron-electron interaction $\hat{V}_{ee}$. In 1927, Born and Oppenheimer introduced their approximation in order to explain theoretically the energy spectrum of molecules [5]. The Born-Oppenheimer approximation is based on the assumption that the motion of electrons and nuclei can be separated. Thus, the total wavefunction is given by a product of a nuclear wavefunction and an electron wavefunction $\Psi = \psi_n(\mathbf{R}) \times \psi_e(\mathbf{r}, \mathbf{R})$, where $\mathbf{r}$ denotes the electron position vector $\{r_i\}$ and $\mathbf{R}$ the position vector for the nuclei $\{r_A\}$.

This assumption is motivated by the observation that the nuclei mass is much larger than the electron mass [1]. As a consequence, the electrons move faster than the heavy nuclei and can adapt nearly instantaneously to any change in the positions of the nuclei $\mathbf{R}$. Hence, the dependence of the electron wave $\psi_e(\mathbf{r}, \mathbf{R})$ on $\mathbf{R}$ can be considered parametrically. Furthermore, the nuclei wave function $\psi_n(\mathbf{R})$ is only dependent on the nuclei coordinates. Applying the Hamiltonian operator under this assumption to the total wave function Ψ results in two separated equations: one for the electron wave function and one for the nuclei wave function. For a fixed nuclear configuration, the electronic wave satisfies the many-electron equation:

$$(\hat{T}_e + \hat{V}_{ee} + \hat{V}_{ne} + \hat{V}_{nn})\psi_e(\mathbf{r}, \mathbf{R}) = E_e(\mathbf{R})\psi_e(\mathbf{r}, \mathbf{R}) \tag{1.3}$$

where $E_e(\mathbf{R})$ is the energy of the electrons in presence of the nuclei. Supposing that the electron structure is solved for all relevant positions of the nuclei, then $E_e(\mathbf{R})$ is the potential surface on which the nuclei move. Then the dynamics of the nuclei can be determined by solving the Schrödinger equation of the nuclei:

$$[\hat{T}_n + E_e]\psi_n(\mathbf{R}) = E_{tot}\psi_n(\mathbf{R}). \tag{1.4}$$

---

[1] In fact, the mass of the majority of nuclei M are 3-4 orders of magnitude greater than the mass of an electron m. For example the lightest nucleus, which is the proton has, a mass of $M \approx 2000m$

Despite the simplifications, the calculation of the many body term due to the electron-electron interaction term in eq. 1.3. remains a particularily difficult challenge. There exists various methods to calculate the many-electron equation. One of the most popular is the Hartee-Fock method, which solves the equation in the space of Slater determinants. The problem with these methods is the huge computational effort due to the large number of variables in the wavefunction ($3N_e$). In the following, the DFT is presented, which reduces the problem to three spatial variables $\mathbf{r} = (x, y, z)$ by reformulating ground state properties in terms of electronic density $n(\mathbf{r})$.

1.1.2 The Hohenberg-Kohn Theorems

In 1964, Hohenberg and Kohn provided the foundations of DFT by developing two theorems [6]. The first theorem states that *the ground-state density* $n(\mathbf{r})$ *of the many-electron system determines uniquely the external potential* $\hat{V}_{ext}$ within a constant. [2] The Hamiltonian can therefore be unambiguously expressed in terms of electronic density. As a consequence, all ground-state observable properties of the system can as well be expressed as a functional of the electron density, in particular the total energy of the system. The total energy is composed of the energy contribution due to the external field $E_{ext}[n(\mathbf{r})]$ and an universal term $F[n(\mathbf{r})]$, which is the sum of kinetic electron energy and electron-electron interaction energy. This universal functional $F[n(\mathbf{r})]$ is valid for any many-electron system in an external field.

$$E[n(\mathbf{r})] = E_{ext}[n(\mathbf{r})] + F[n(\mathbf{r})] = E_{ext}[n(\mathbf{r})] + T_e[n(\mathbf{r})] + E_{ee}[n(\mathbf{r})]. \tag{1.5}$$

The second theorem is a variational principle: *The ground state density* $n_0(\mathbf{r})$ *is the one that minimizes the energy Functional* $E[n(\mathbf{r})]$. Both theorems provide a way to solve many-electron system by reformulating the problem in terms of electronic density only depending on three spatial coordinates. The first theorem is a proof of existence of such a functional. And the second one tells us that the ground state electronic density can be found by applying the variational principle on the total energy functional. Unfortunately, the theorems do not provide any mathematical expression of the universal functional $F[n(\mathbf{r})]$. The determination of this functional remains the main difficulty of the DFT. The Kohn-Sham equations (KS) give a computational tool to apply these theorems to DFT calculations.

---

[2] The external potential is created by the nuclei and/or an external field.

1.1.3 The Kohn-Sham equations

To give a mathematical expression of kinetic and interaction energy as a functional of the total density, Kohn and Sham proposed in 1965 an Ansatz allowing to establish a calculation scheme useful for practical implementation [7]. As the expression for the kinetic energy of non-interacting electrons is known, the Ansatz of Kohn and Sham is to replace the real many-electron system by a fictitious system of non interacting electrons moving in an effective potential V_{eff} in such a way that the resulting density equals to the real N_e electron system (within a constant). Each non-interacting electron follows the one-body Schrödinger equations leading to a set of N independent Kohn-Sham equations:

$$\left[\frac{1}{2}\nabla^2 + V_{eff}(\mathbf{r})\right]\phi_i = E_i\phi_i. \tag{1.6}$$

The N one-body equations are analytically solvable. For such a system, the expression of the electron density is known and constructed by summing up the square moduli of occupied states:

$$n(\mathbf{r}) = \sum_i^N \left|\phi_i^2(\mathbf{r})\right|. \tag{1.7}$$

The total energy of this fictitious Kohn-Sham electron system can be written as a functional by applying the first Hohenberg-Kohn theorem:

$$E[n(\mathbf{r})] = T_{KS}[n(\mathbf{r})] + E_{eff}[n(\mathbf{r})] \tag{1.8}$$

with

$$T_{KS}\left[n(\mathbf{r})\right] = -\frac{1}{2}\sum_i \langle\phi_i|\, \nabla^2 \,|\phi_i\rangle. \tag{1.9}$$

The transformation is in principle exact at this state. However, an expression for the unknown effective potential V_{eff} has to be found. The idea is to decompose the effective potential in such a way that practical implementations are feasible. For that purpose, first the electron-electron interaction term of the universal functional is decomposed in a classical coulomb interaction between pair electrons, the Hartree term $E_H[n(r)]$, plus a residue term $R_{ee}[n(\mathbf{r})] = E_{ee}[n(\mathbf{r})] - E_H[n(\mathbf{r})]$. Second, the kinetic term of the universal functional is split into a kinetic energy term of non interacting electrons $T_{KS}[n(r)]$ and another residue term $R_{kin}[n(\mathbf{r})] = T_e[n(\mathbf{r})] - T_{KS}[n(\mathbf{r})]$. The exchange-correlation term $E_{XC}[n(\mathbf{r})]$ is the sum of these two residue terms:

$$E_{XC}[n(\mathbf{r})] = (E_{ee}[n(\mathbf{r})] - E_H[n(\mathbf{r})]) + (T_e[n(\mathbf{r})] - T_{KS}[n(\mathbf{r})]). \tag{1.10}$$

The exchange-correlation term $E_{XC}[n(\mathbf{r})]$ is universally valid. This term represents the error made by using a non-interacting kinetic energy, named as correlation part, and the error made in treating the electron-electron interaction classically, often referred as exchange part.

Once these energy terms are decomposed, the condition of same electronic ground state density is used. This condition results in the same total energy for the fictitious and real systems:

$$T_{KS}[n(\mathbf{r})] + E_{eff}[n(\mathbf{r})] = T_{KS}[n(\mathbf{r})] + E_H[n(\mathbf{r})] + E_{ext}[n(\mathbf{r})] + E_{XC}[n(\mathbf{r})]. \tag{1.11}$$

Likewise, the equation 1.11 can be used to rewrite the effective potential. First, the effective energy term is isolated and then its variational is taken with respect to the electronic density $V_{eff} = \frac{\partial E_{\text{eff}}}{\partial n}$. The effective potential after transformation is given by:

$$V_{eff}(\mathbf{r}) = \int \frac{n(\mathbf{r})}{\mathbf{r}} d\mathbf{r} + V_{ext}(\mathbf{r}) + V_{XC}[n(\mathbf{r})] \tag{1.12}$$

with

$$V_H(\mathbf{r}) = \int \frac{n(\mathbf{r})}{\mathbf{r}} d\mathbf{r}. \tag{1.13}$$

With the expression of the effective potential, all ingredients for practical implementations are collected. Thereby, the reformulation by Kohn-Sham permits an auto-coherent resolution scheme to find the ground state density of the system of interacting electrons. In figure 1.1 this calculation scheme is illustrated. Instead of minimizing the total energy functional $E[\mathbf{r}]$, the effective potential given by eq. 1.12 is calculated from an initial density guess. Then the Kohn-Sham equations are solved. On the basis of the KS-orbitals, a new density and the corresponding energy is calculated. The new density and energy values are compared to its value at the previous step. If the results are auto-coherent, the self-consistent loop is stopped. Otherwise, a new iteration step is performed, until the convergence of the energy and density is reached. Once the ground-state density is determined, other output quantities can be calculated, since all ground state properties can be written as functionals of this density (cf. second Hohenberg-Kohn theorem).

Furthermore, this calculation scheme can be applied to any arrangement of nuclei and thus provides the energy surface of the material at zero Kelvin. Therefore, the DFT allows the determination of (for example zero temperature) phase diagrams, phonon frequencies or elastic constants. Moreover, the Hellmann-Feynman theorem can be employed for the calculation of forces acting on nuclei [8]. Thus in principle, one can also compute finite temperature properties by using Monte Carlo (MC) or Molecular Dynamics (MD) methods.[3]

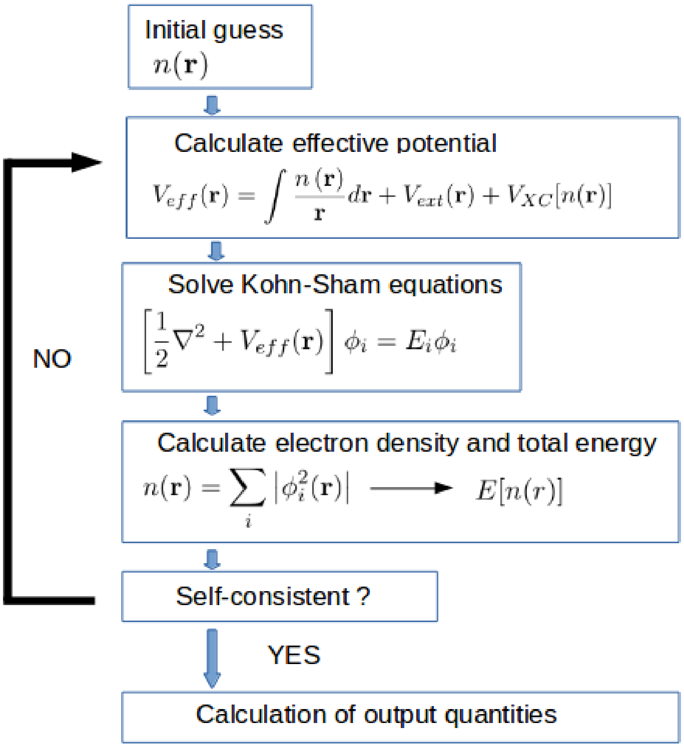

Figure 1.1: Schematic representation of the self-consistent loop used in DFT calculations.

In summary, the universal functional $F[\mathbf{r}]$ of interacting particles (with unknown mathematical form) has been replaced by its equivalent of non-interacting particles of known form and the exchange correlation term. Applying the Kohn-Sham calculation scheme to this fictitious system gives the ground state density. At this state, the KS equation are in principle an exact theory. But the E_{XC} term is not known exactly and has to be approximated. The strength of DFT is that even rude approximations lead to acceptable results (see section 1.1.5).

---

[3] In practice *ab initio* MC or MD calculations are to computationally expensive.

1.1.4 Periodic DFT

The computational cost of the DFT calculation scales quadratic with the number of electrons in the system. The periodic boundary conditions are applied to avoid a disproportionate number of computational resources by simulating bulk crystals. Thereby the simulation cell is considered as a unit cell of a system that is periodically replicated in three dimensions, see figure 1.2. The translation symmetry is used in the Bloch's theorem, which can be applied to calculate the ground state density tractable through the Brillouin Zone (BZ) sampling. In the next subsection the Bloch's theorem and the Brillouin Zone sampling are presented. Further increase of computational efficiency is achieved by the introduction of pseudopotentials, which will be the subject of the subsequent section.

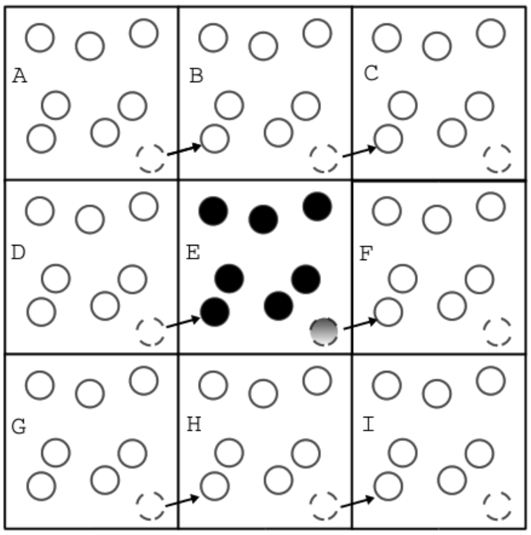

Figure 1.2: An ion moves from the cell E to the cell F. The periodic boundary condition replicates the same movement for the other images and thus an ion from cell D enters instantaneously in cell E keeping the number of ions in the simulation cell constant. [9]

Brillouin Zone sampling

The solid is computed using periodic boundary conditions. In such a periodic system the Bloch theorem applies on the electron wavefunction, i.e. the wavefunction can be written as a plane-wave times a cell periodic function $u_{n\mathbf{k}}(\mathbf{r})$:

$$\phi_{n,\mathbf{k}}(\mathbf{r}) = u_{n\mathbf{k}}(\mathbf{r})e^{i\mathbf{kr}} \tag{1.14}$$

where $\mathbf{k}$ denotes the wavevector. The wavefunction 1.14 can be inserted in the electron density given in equation 1.7. Furthermore, as a consequence of periodicity in real space, the reciprocal space is also periodic and thus the $\mathbf{k}$ vectors can be reduced to the first Brillouin Zone (BZ). Thereby, the electronic density becomes:

$$n(\mathbf{r}) = N' \sum_i \int_{BZ} u^{\star}_{n\mathbf{k}}(\mathbf{r}) u_{n\mathbf{k}}(\mathbf{r}) d\mathbf{k} \tag{1.15}$$

where N' is a proportionality factor such as the integration of the electron density over space gives the total number of electrons in the simulation cell. The integration in equation 1.15 is carried out over the entire first BZ. In the k-point mesh sampling, the integral is approximated by summing over a finite number of k-points with important contributions to the integral. Different methods of k-point sampling in the BZ has been proposed and shown to be successful. In all these methods the precision of the electronic density depends on the density of the k-point mesh.

Plane-wave DFT and Pseudopotential

In the previous section, the Bloch theorem was applied to the electronic wavefunction. Thereby, a cell periodic function has been introduced:

$$u_{n\mathbf{k}}(\mathbf{r}) = u_{n\mathbf{k}}(\mathbf{r} + \mathbf{R}). \tag{1.16}$$

In the plane-wave DFT, the cell periodic function is Fourier expanded in terms of plane-waves:

$$u_{n\mathbf{k}}(\mathbf{r}) = \sum_{\mathbf{G}} C_G e^{(i\mathbf{G}.\mathbf{R})} \tag{1.17}$$

with $C_{\mathbf{G}}$ being the expansion coefficients. Even if the Fourier expansion demand an infinite number of $\mathbf{G}$-vectors, in practice, the sum is limited to plane waves, whose kinetic energy is lower than the so called cut-off energy E_{cut}:

$$\frac{1}{2}(\mathbf{k} + \mathbf{G}) < E_{cut}. \tag{1.18}$$

The precision of the DFT calculation depends on the choice of the cut-off energy E_{cut}.

Large cut-off energies are required for the tight bound core electrons and for the strongly space oscillating valence electron wavefunctions in the core region. Therefore, in practice the plane-wave DFT becomes applicable in the framework of the pseudopotential approximation. The pseudopotential formalism is based on the observation that core electrons are poorly involved in chemical bounding and can therefore, in good approximation, be considered to be independent from the chemical environment. Thus, only the valence electrons are explicitly used in the electronic structure calculation, while the core electrons and the nucleus are substituted by an effective potential. On the one hand this reduces strongly the number of electrons explicitly involved in the electron density calculation and on the other hand a convenient choice of the effective potential can avoid the strong space oscillation of valence wavefunctions in the core regions. In fact, the valence electron wavefunctions have to verify the condition of orthogonality, i.e. they have to be orthogonal to all core wavefunctions leading to strong spatial oscillation. Thus if the pseudopotential is chosen to present a smooth, nodeless form, the oscillations are reduced. Consequently, the valence electron wavefunctions can be described by a reduced number of expansion coefficients.

1.1.5 The different classes of exchange correlation functional

The accuracy of DFT depends on the quality of the approximation made for the E_{XC} functional. There exists a large number of functionals, which are more or less adapted for a particular study. Kohn and Sham presented the first E_{XC} functional in 1965, the Local Density Approximation (LDA), where the inhomogeneous system is locally described as a homogeneous electron gas. In this case, the electronic density equals the average number of electrons per volume: $n(\mathbf{r}) = N_e/V$ and the exchange correlation functional can be written as:

$$E_{\mathrm{XC}}\left[n\left(\mathbf{r}\right)\right] = \int n\left(\mathbf{r}\right)\epsilon_{\mathrm{XC}}\left(n\left(\mathbf{r}\right)\right)d\mathbf{r} = \int n\left(\mathbf{r}\right)\left(\epsilon_{\mathrm{X}}\left(n\left(\mathbf{r}\right)\right) + \epsilon_{\mathrm{C}}\left(n\left(\mathbf{r}\right)\right)\right)d\mathbf{r} \tag{1.19}$$

where the term $\epsilon_{\mathrm{XC}}\left(n\left(\mathbf{r}\right)\right)$ corresponds to the exchange-correlation energy per particle of a uniform electron gas. It depends on the density at point r and does not take changes in its local environment into account. The $\epsilon_{\mathrm{XC}}\left(n\left(\mathbf{r}\right)\right)$ can furthermore be split into an exchange part $\epsilon_{\mathrm{X}}\left(n\left(\mathbf{r}\right)\right)$ and correlations part $\epsilon_{\mathrm{C}}\left(n\left(\mathbf{r}\right)\right)$. An analytic expression of the exchange term can be derived for an homogeneous electron gas. An explicit expression for the correlation energy is unknown, but it can be determined numerically by Monte Carlo calculations for an homogeneous electron gas [10]. In this approximation, the energy functional is reduced to a simple local function of the density. In real systems, the electronic density can vary strongly in space.

Corrections of LDA can be done by introducing additionally a dependence of the gradient of the density on the E_{XC} functional. This class of semi-local E_{XC} functionals are called generalized gradient approximation (GGA) and have the form:

$$E_{\mathrm{XC}}\left[n\left(\mathbf{r}\right)\right] = \int n\left(\mathbf{r}\right) \epsilon_{\mathrm{XC}}^{GGA}\left(n\left(\mathbf{r}\right), \nabla(n\left(\mathbf{r}\right)\right) d\mathbf{r}. \tag{1.20}$$

The development of reliable functionals became an own field of research and led to a wide variety of exchange correlation fucntionals. The most commonly used GGA approximation in solid state physics is the one introduced by Perdew, Burke, and Ernzerhof (PBE) E_{XC} functional [11]. In 2008, Perdew developed an improved PBE functional taking the degrees of freedom associated to geometry in solids (PBEsol) into account [12]. Wu and Cohen developed a functional based on a diffuse radial cutoff for the exchange hole in real space and the analytic gradient expansion of the exchange energy for small gradients [13]. In general, LDA and GGA approximation are known to have limitations. In the LDA approximation, the atoms tend to 'over-bind' resulting in a too small equilibrium volume with respect to experimental results. The GGA approximation represents an improvement of LDA, but tends to 'over-correct' and results, in general, in a too large equilibration volume. Both LDA and GGA functionals underestimate the band gap calculated from the Kohn-Sham energies. It has to be kept in mind that these energies correspond to a fictive non-interacting system and have in principle no physical interpretation. However, a one-to-one correspondence between band gap error and the static screening property, which is a ground state property and thus determinable with DFT from the electronic density, was observed [14].

Another class of approximation of E_{XC} functionals are the hybrid functionals introduced by Becke in 1993 in order to improve electronic properties. Hybrid functionals incorporate a portion of exact exchange from Hartee-Fock theory hybridized with exchange correlation from other *ab initio* or empirical functionals. These functionals show in general more accurate band gap and screening properties. One of the most popular hybrid functionals is B3LYP, which stands for Becke, 3-parameter, Lee-Yang-Parr [15]. Bilc *et al.* proposed an alternative hybrid functional, B1-WC, that mixes exact exchange with the GGA of Wu and Cohen [1]. The Heyd-Scuseria-Ernzerhof functional (HSE) is based on a screened Coulomb potential for the exchange interaction improving computational performance in particular in metallic systems [16].

1.1.6 DFT applied on $BaTiO_3$

Since the beginning of the 1990s electronic structure methods and in particular DFT calculations became central for the microscopic comprehension of the origin of ferroelectricity in oxides. In a pioneer work, Cohen and Krakauer performed within the LDA approximation a series of frozen phonon calculations. These calculations underline the experimental observed ferroelectric transition and show that the cubic phase of $BaTiO_3$ is unstable with respect to soft-mode distortions [17]. They studied the energy surfaces with respect to soft-mode displacement and demonstrated its high sensibility of depth and shape to strain. Cohen and Krakauer emphasised in a later article that the hybridization between the titanium 3d and oxygen 2p is necessary for ferroelectricity in $BaTiO_3$ and $PbTiO_3$ [18]. In addition, they pointed out that the difference of the phase transition sequence in $BaTiO_3$ and $PbTiO_3$ is due to very distinct A-O interactions. Singh and Boyer made evident that ferrolectricity in perovskite shows a delicate balance between short-range repulsion favouring the paraelectric cubic phase and long-range electrostatic forces favouring the ferroelectric phases [19]. In 1993, King-Smith and Vanderbilt developed a theory of polarization in crystalline solids on the basis of Wannier functions. Thanks to the developed methodology, polarization, Born effective charge and piezoelectric constants became able to be computed within DFT and this led to a great progress in the understanding of ferroelectricity [20] [21]. Early experimental measurements of Born effective charges in $BaTiO_3$ by optical measurement of LO-TO splitting showed very large values compared to the nominal charges, which was then confirmed theoretically by DFT calculations. The DFT calculations showed that these high values are due to strong hybridization [22]. Fu and Cohen were able to explain the experimentally large piezoelectric response of $BaTiO_3$. They determined its origin in the large strain induced by rotation of the polarization from rhombohedral to tetragonal orientation [23]. Different *ab initio* studies examined the surface energy of periodic slabs of $BaTiO_3$ with or without applied external electric field. All calculations revealed a high surface energy, which explains the difficulty of cleavage in $BaTiO_3$ [24] [25] [26].

During the last two decades, DFT allowed important insight into the microscopic mechanisms in $BaTiO_3$ and other ferroelectrics. As mentioned above, DFT results depend on the used exchange-correlation functional and give in general errors of a few percentage in the equilibrium cell parameters. Ferroelectric properties are strongly coupled to strain and an underestimation of 1-2% in the equilibrium volume can even suppress ferroelectricity [27]. Thus, in some cases, calculations are performed at experimental equilibrium volume to avoid this problem. As a result, electromechanical constants or Born effective charges were in better agreement with experiments. Nevertheless, the spirit of *ab initio* calculation is the determination of systems without the need of experimental input and is essential to designing new improved ferroelectric-based materials, where experimental data are unavailable.

In order to determine the most adapted E_{XC} functionals, Kresse et al. studied recently the structural, electronic and phonon properties of the cubic and the tetragonal phase in $BaTiO_3$ for a variety of E_{XC} functionals [28]. In table 1.1, the structural properties for $BaTiO_3$ in cubic and ferroelectric tetragonal phase are listed for various E_{XC} functionals. In the cubic phase, Kresse et al. pointed out that LDA underestimates the lattice constant *c* by around 1% as expected. PBE and the hybrid B3LYP overestimates the lattice constant by the same amount. HSE and PBEsol lead to a lattice constant very close to experimental measurements. The Wu-Cohen functional (WC [13]) underestimates the lattice constant. As the hybride B1-WC functional includes a portion of WC, its lattice constant is also underestimated. In the tetragonal phase the cell volume follows the same tendency as in the cubic phase. The extent of the tetragonal distortion is given by the c/a ratio. LDA give rise to a very good c/a ratio, whereas PBE strongly overestimate it. PBEsol, WC and B1-WC lie between LDA and PBE and are thus in good agreement with experiments. This c/a ration is strongly overestimated for HSE and B3LYP. Comparing the ferrolectric displacement in the tetragonal phase, it has been observed that its magnitude is essentially dependent on the volume. Thus the magnitude of the ferroelectric displacement is twice as large in PBE as in LDA.

For the electronic properties, the expected tendency is observed. LDA and GGA based functionals underestimate the band gap. The best electronic properties are given by the WC functional. B3LYP overestimates the band gap, while HSE slightly underestimates it. The best results are obtained for B1-WC (see table 1.2).

In table 1.3, zone-center frequencies are summarized for the cubic structure of $BaTiO_3$. A large scatter in phonon frequencies can be observed even in the same family of E_{XC} functionals. This is due to the fact that the calculated phonon frequencies are sensitive to the lattice constant and not to the applied functional. An exception is HSE, which tends to stiffen the phonon modes due to Hartree exact correlation. Within HSE, phonon frequencies are described best followed by LDA because of the small cell parameters. GGA based functionals give rise to too soft phonon modes. Slightly better results are obtained by B1-WC.

Table 1.1: Lattice constant, bulk modulus in cubic phase of BaTiO$_3$. Structural properties, tetragonal distortion c/a, atomic displacement of the oxygen parallel to the c lattice constant

	LDA	PBE	PBEsol	WC	HSE	B3LYP	B1-WC	Expt.
cubic								
a_0 (Å)								
Ref. [28]	3.953	4.035	3.986		3.995			4.00a
Ref. [29]	3.96	4.03				4.04		
Ref. [1]	3.958	4.035		3.990		4.036	3.971	
B_0 (GPa)								
Ref. [28]	189	162	177		181			162a
Ref. [29]	196	175				176		
Ref. [30]	195	160						
tetragonal								
a								
Ref. [28]	3.945	4.005	3.971		3.969			3.997a
Ref. [1]	3.954	4.013		3.982		3.996	3.962	
c/a								
Ref. [28]	1.009	1.050	1.021		1.042			1.0086a
Ref. [1]	1.006	1.035		1.012		1.066	1.015	
dz_0								
Ref. [28]	-0.017	-0.047	-0.028		-0.042			-0.026a
Ref. [1]	-0.014	-0.039		-0.022		-0.057	-0.024	
$P(C/m^2)$								
Ref. [28]	0.216	0.435	0.314		0.407			0.27c
Ref. [1]	0.20	0.39		0.26		0.48	0.28	

a Ref. [31]
c Ref. [32]

In summary, the best results in structural, electronic and phonon properties are obtained with HSE functional, but the computational cost is at least one order of magnitude more expensive than the other functionals. As PBEsol and WC predicts well the properties of BaTiO$_3$, they present a good alternative to HSE.

Although DFT calculations are very powerful methods and have been crucial in the microscopical understanding of ferroelectricity, auto-coherent methods demand a high computational effort. Thus, they are limited in time and length scales. Therefore, they can generally provide only static properties for complex systems, such as ferroelectric materials, primarily at zero Kelvin. But finite temperature calculations at long time scale are needed for the complete description of the phase transitions of ferroelectric materials with increasing temperature. The dielectric and piezoelectric properties are strongly temperature dependent in particular close to the phase

Table 1.2: Direct Γ-Γ (and indirect R-Γ) bang gap in eV for cubic and tetragonal structure in $BaTiO_3$

	LDA	PBE	PBEsol	HSE	B3LYP	WC	B1-WC	Expt.
cubic								
Ref. [28]	1.84	1.87	1.91	3.07				
	(1.73)	(1.70)	(1.77)	(2.92)				(3.2b)
Ref. [1]	2.2	2.2			3.8	2.2	3.45	
	(2.1)	(2.1)			(3.7)	(2.1)	(3.39)	
tetragonal								
Ref. [28]	2.09	2.31	2.16	3.55				
	(1.84)	(1.76)	(1.76)	(3.02)				(3.4b)
Ref. [1]							3.73	
	(2.10)				(3.80)		(3.44)	

b Ref. [32]

Table 1.3: Zone-center phonon frequencies in cm^{-1} for the cubic phase of $BaTiO_3$. The lattice constant used for each calculation is given in Å in the second column.

Work	(Å)	Γ_{15}(TO1)	Γ_{15}(TO2)	Γ_{25}	Γ_{15}(TO3)	
Ref. [28]	3.953	LDA	139i	186	291	479
Ref. [28]	4.035	PBE	239i	169	286	453
Ref. [28]	3.986	PBEsol	188i	178	287	465
Ref. [28]	3.995	HSE	241i	185	310	480
Ref. [27]	3.94	LDA	113i	184	288	481
Ref. [30]	4.03	PBE	203i	168		463
Ref. [1]	3.990	WC	128i	186	282	469
Ref. [1]	3.971	B1-WC	145i	195	299	482
Ref. [33]	395K	Expt.	soft	182	308	482

transition temperature. Furthermore, many properties are given by the dynamics of domain walls such as the hysteresis loop. However, simulation of the dynamics of domain walls demands length scales of the order of nanometres.

1.1.7 Conclusion

In this section the principle of DFT has been presented. Furthermore it has been stated that the accuracy of DFT depends on the exchange correlation functional, the nature of the basis set of the pseudo-potential, the k-point mesh, plane wave cut off energy, the break criteria in the self consistent DFT calculation loop and on the implementation in different DFT-codes. Especially, the accuracy of DFT-calculated properties of $BaTiO_3$ for different functional has been summarized. It has been pointed out that an adapted choice of an E_{XC} functional leads to precise results and is a powerful tool for the microscopical understanding of ferroelectricity. The drawback of DFT is given by its high computational cost making its application on nano-scale systems and on large time scales difficult. But its ability to calculate precise properties of ferroelectrics without the need of experimental input can be used for the parametrization of second principles methods (cf. next section).

1.2 Effective Hamiltonian

As mentioned in the previous section, *ab initio* Molecular Dynamics simulations of the structural phase transitions is not manageable through DFT due to its high computational cost. In this section, first the principle of the effective Hamiltonian is presented for the modelling of ferrolectric systems. This principle allows to calculate complex structural and transitions properties under the use of intelligently chosen approximations with lower computational cost. Second, the contribution of the effective Hamiltonian to the advances in understanding dynamics of ferroelectrics and its limits are summarized on the example of the prototype ferroelectric $BaTiO_3$.

1.2.1 Principle and derivation of the effective Hamiltonian

In 1995, Zong, Vanderbilt and Rabe derived the first effective Hamiltonian for the perovskite ferroelectric compound $BaTiO_3$ [34] [35]. They were able to describe its properties at finite temperature. Finite temperature properties of a statistical system is described by the partition function. This central quantity can be determined by the total potential energy as a function of the atomic displacements. The request is to make a suitable approximation in order to get a simplified and parametrizable expression of the Hamiltonian. The effective Hamiltonian approach is based on two main observations. First, experimental results and first principle total energy calculations advocate that essentially small atomic displacements and strain deformations from the cubic perovskite structure are involved in the ferroelectric phase transition. Thus, the equilibrium cubic structure can be seen as the reference structure and a Taylor expansion of the energy in displacements with respect to this reference phase can be performed. The Taylor expansion has to be done at least up to fourth-order as ferroelectricity is known to be an anharmonic phenomenon. Furthermore, the contribution to the partition function is exponentially decreasing with increasing energy. Therefore, one can, in good approximation, consider only contributions to the partition function from low-energy distortions. The second central observation is that among all the possible low-energy distortions, mainly two phonon branches make important contribution to the phonon density: The lowest TO modes (soft mode) and long-wavelength acoustic (strain variables) phonon. Instead of expressing the energy expansion of the unit cell in terms of all 15 degrees of freedom, it can be reduced to the 6 relevant degrees of freedom associated to these two phonon branches. The strain degrees of freedom for each unit cell l are described in terms of displacement vectors $\mathbf{v}_l$. The soft mode is described as a collective motion of displacement of individual atoms (local mode). There exists no unique choice for local modes to describe the same soft mode throughout the Brillouin Zone. Thus, the local mode is chosen as symmetric as possible to minimize the number of expansion terms. The local mode should minimize the interaction between adjacent local modes. The amplitude of the local mode of a unit cell l is given by the variables $\mathbf{u}_l$ and the local mode chosen for $BaTiO_3$ is represented in figure 1.3.

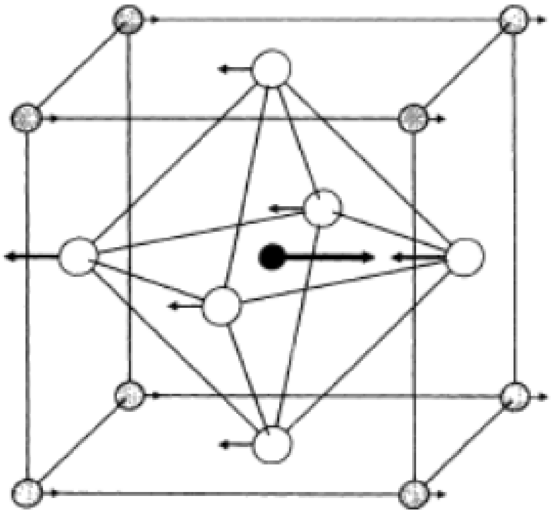

Figure 1.3: The perovskite structure of cubic $BaTiO_3$. Ba, Ti and O atoms are represented by shaded, solid and empty circles, respectively. The length of the arrows is proportional to the magnitude of the displacements for a local mode polarized along $\mathbf{x}$. [34]

The Taylor expansion of the energy in terms of soft mode variables $\mathbf{u}_l$ and strain variables $\mathbf{v}_l$ includes five terms:

$$E^{\text{total}} = E^{\text{self}}(\{\mathbf{u}\}) + E^{\text{dpl}}(\{\mathbf{u}\}) + E^{\text{short}}(\{\mathbf{u}\}) + E^{\text{elas}}(\{\mathbf{v}\}) + E^{\text{int}}(\{\mathbf{u}\},\{\mathbf{v}\}). \quad (1.21)$$

The first term is the soft mode self energy term $E^{\text{self}}(\{\mathbf{u}\}, \kappa_{\in}, \alpha, \gamma)$ describing the energy penalty by displacing atoms in a unit cell according to the local mode. The second term is the long-range dipole-dipole energy $E^{\text{dpl}}(\{\mathbf{u}\}, \mathcal{Z}^{*}, \epsilon_{\infty})$ and the third term is a short range correction to this term $E^{\text{short}}(\{\mathbf{u}\}, \mathcal{J}_{ij,\alpha,\beta})$. The fourth term represents the harmonic elastic energy $E^{\text{elas}}(\{\mathbf{v}\}, \mathcal{B}_{11}, \mathcal{B}_{12}, \mathcal{B}_{44})$ and the last term $E^{\text{int}}(\{\mathbf{u}\}, \{\mathbf{v}\}, \mathcal{B}_{1xx}, \mathcal{B}_{1yy}, \mathcal{B}_{4xz})$ the anharmonic strain-soft-mode coupling. The parameters for each energy term are added in italic characters to the previous notation.

The effective Hamiltonian is fully specified by a set of parameters, which can be determined by DFT calculations, whereat most of the parameters are derived from frozen-phonon calculations. These parameters are the fourth order terms of on-site energy α and γ, the elastic constants $\mathcal{B}_{11}, \mathcal{B}_{12}, \mathcal{B}_{44}$, the on-site elastic-mode interaction parameters $\mathcal{B}_{1xx}, \mathcal{B}_{1yy}, \mathcal{B}_{4xz}$, the mode effective charge $\mathcal{Z}^{*}$ (for more details, see [22] [36]). Since the quality of the DFT calculations for optical dielectric constant is not satisfactory for simple exchange-correlation functionals, experimental values are often taken.

The determination of intersite interaction parameters of the interaction matrix $\mathcal{J}_{ij,\alpha,\beta}$ is extracted from the energy for distortions at the zone-boundary [35]. Once the set of parameters is determined for the effective Hamiltonian, either MD or MC simulations can be performed and finite temperature properties can be calculated.

1.2.2 Effective Hamiltonian applied on ferroelectric compounds

Due to its much smaller CPU-cost compared to DFT, the effective Hamiltonian approach allows large-scale simulations at finite temperature. Therefore, this method provides a tool to give insight into nano-structured ferroelectrics, which are difficult to simulate with DFT, but which are of scientific and technological interest.

The effective Hamiltonian with classical Monte Carlo simulations reproduces the experimentally observed phase transition sequence in several ferroelectric Perovskite compounds, *inter alia* the bulk $BaTiO_3$ [35]. However, the calculated transition temperatures are 290 K, 230 K and 200 K, instead of the experimentally observed temperatures 403 K, 278 K and 183 K, respectively. The underestimation of transition temperatures have been essentially related to a poor description of thermal expansion by the effective Hamiltonian [37]. The effective Hamiltonian approach was also applied to the study of domain walls and in tetragonal $BaTiO_3$ with a simulation cell composed by 40x10x10 unit cells and which include two 180° domain walls [38]. The thickness of the 180° domain walls was evaluated to be only 5.6 Å. The general form of effective Hamiltonian for bulk ferroelectrics as presented above cannot be directly applied to studies of thin film ferroelectrics and solid solutions. Additional terms in the effective Hamiltonian have to be included to describe surfaces or to include compositional degrees of freedom for complex systems. In fact, the studies of alloys are interesting for the design of new materials with tailored properties. The solid solution Pb(Zr,Ti)O_3 is nowadays applied in transducers and actuators, because of its large piezoelectrocity. Bellaiche et al. developed an effective Hamiltonian for alloy systems, such as Pb(Zr,Ti)O_3 [39]. The effective Hamiltonian simulation for structural and piezoelectric properties were in good agreement with experimental findings. Furthermore, this approach give insight into the origin of the huge piezoelectric d_{33} coefficient near the morphotropic phase boundary.

The effective Hamiltonian approach contributed to the understanding of simple utrathin ferrolectric films (UFF). Size effects become important and affect ferroelectric properties in such low-dimensional systems. Almahmoud *et al.* developed an effective Hamiltonian for UFF Pb(Zr,Ti)O_3 by including an appropriated part into the Hamiltonian that are related to the vacuum-solid interface [40]. The investigation shows that the in plane rotation of the spontaneous polarization can increase piezoelectricity and dielectricity and that phase transition sequence changes compared to bulk Pb(Zr,Ti)O_3. A complete review about the state of art in ultrathin ferroelectric films is given by [41]. The effective Hamiltonian investigations revealed that ferroelectric transition exists in low-dimensional structures. This is an important finding as it makes ferroelectric properties applicable to nano-scale devices.

Furthermore, the effective Hamiltonian approach was used for the study of different nano-structures (nanowires, nonodisks, nanorods and nanodots) [42] [43] [44]. Although the effective Hamiltonian approach was applied to various ferroelectric systems, it has to be kept in mind that these simulations treat only a reduced number of degrees of freedom. Therefore, for a successful functionality of the effective Hamiltonian approach the identification of the critical degrees of freedom needs to be preassigned.

1.3 Shell Model

The Shell Model (SM) has a long history in the atomistic modelling of ionic materials using interatomic potentials that mimics the real interaction between atoms. Its specificity is the inclusion of the polarisability of the ions.

1.3.1 Principle and derivation of the Shell Model

In the Shell Model the atom is represented as positive core charge located at the site of the nucleus and a negative shell charge. These charges are connected by a spring, which can be of harmonic or anharmonic nature (see fig. 1.4). The core charge can be interpreted physically as an effective nuclear charge and the shell as the corresponding effective valence charge mainly responsible for the polarization response of an atom. However, in practice the charges are frequently treated as adjustable parameter of the model rather than physically true charge values. The values of the charges are kept fixed in this model. The polarization of an atom is given by the relative displacement of the shell to the core. Thus, the polarizability of the atom depends on the stiffness of the connecting spring. In the traditional approach of the Shell Model, the terms of the interatomic potential are pairwise additive. The cores and shells of different atoms interact via Coulomb 's law: $V_C(r_{ij}) = q_i q_j / r_{ij}$, where r_{ij} is the distance between two charges q_i and q_j. A short-range interaction term between shells of different atoms represents both electron cloud repulsion and van der Waals attraction and is generally described by a Buckingham potential: $V_B(r_{ij}) = Aexp(r_{ij}/\rho) + C/r_{ij}^6$ or a Rydberg potential: $V_R(r_{ij}) = (a + Br_{ij})exp(r_{ij}/\rho)$. The coupled core and shell interaction for a ferroelectric compound is generally taken to be anharmonic $V(r) = k_2 r^2/2 + k_4/24r^4$. The free parameters in the Shell Model are the core and shell charges, the constants in the short-range interaction and in the spring potential. The parameters of the Shell Model can be derived from first principle calculations through fitting on the potential energy surface by least square minimization.

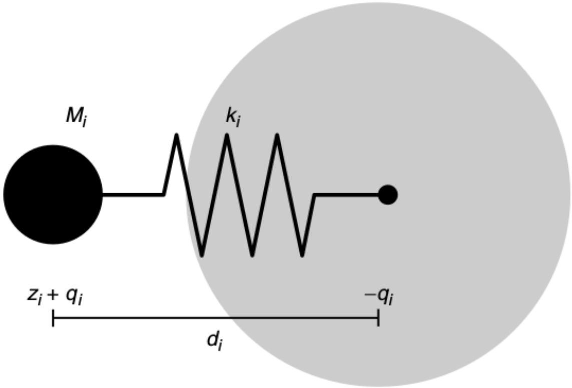

Figure 1.4: Schematic representation of the atom in the Shell Model. The core of charge $z_i + q_i$ and is attached by a spring to a shell charge $-q_i$. [45]

1.3.2 Application of the Shell Model

In 1999 the first Shell Model was developed, which was successful in the description of the phase transition sequence of $BaTiO_3$ [46]. This first generation of Shell Models considered an anisotropic core-shell interaction at the oxygen ions with a fourth-order core-shell interaction along the O-Ti bond. The Ba and Ti ions were taken as isotropically polarizable. The free parameters were determined by fitting carefully zero temperature energy in cubic and ferroelectric phase for various configurations of atomic displacements. This first Shell Model was a breakthrough for atomistic modelling. The first Shell Model demonstrated the capability of Molecular dynamic simulations to reproduce complex phase transition sequence with increasing temperature. The model is in good agreement with experimental data for the lattice parameters and expansion coefficients for the different phases. The values of polarization are also reasonable well calculated. However, the theoretically determined transition temperatures tend to be too small, like in the effective Hamiltonian approach. As both approaches are derived from first principle DFT calculations, this suggests that the error may be due to imprecisions in the reference data. The drawback of this first generation of Shell Models is that they can only be applied to systems, where the crystallographic environment is well-defined for the oxygen ions. Therefore, the anisotropic Shell Model is for example not applicable to complex microstructure, where the local environment is not well defined at grain boundaries. A study of such a kind of system requires isotropic Shell Models.

In 2000 an isotropic Shell Model has been derived for $KNbO_3$ [47] and four years later for $BaTiO_3$ and $SrTiO_3$ [48]. (There exists as well more recently developed isotropic Shell Model, 2013 [49]). The isotropic Shell Models are in good agreement with experimental results, such as the phase transition sequence, the lattice parameters, the Born effective charges, and the polarization as a function of temperature. This second class of isotropic Shell Models has been used for the study of solid solutions. Solid solutions of a ferroelectric material have gained a considerable interest in atomistic simulations emerging from the desire to design new structures including properties unobtainable in single-component materials. The solid solution $Ba_xSr_{1-x}TiO_3$ has been built from the two isotropic Shell Models $BaTiO_3$ and $SrTiO_3$ [48]. This model was able to describe the general features of experimental observations in a semi-quantitative manner. Notably, the critical concentration of Sr, for which all three Curie temperatures coincide and a rhombohedral to cubic phase transition occurs, concurs with the experimental value of $x \approx 0.2$. Nevertheless, the phase transition temperatures were badly reproduced. Furthermore, the correlation between the dielectric properties of the solid solution and the local structure were studied. It was revealed that the experimentally observed broadening of the static dielectric peak around the phase transition temperature is mainly dependent on the average cell volume.

Sepliarsky used a Shell Model for the study of ferroelectric phase transitions and dynamical behaviour in a ferroelectric/paraelectric $KNbO_3/KTaO_3$ superlattice with varying modulation length[50] [51]. These atomistic simulations confirmed the experimental observation that for large modulation lengths the $KNbO_3$ layers are almost independent of each other. Below a critical modulation length, the structural phase transition occurs at the Curie temperature of the KTN solid solution [52]. Therefore, in this case the superlattice acts as a single artificial ferroelectric composite. The atomistic simulation shows that, in the paraelectric $KTaO_3$ layers, polarization is induced due to long-ranged ferroelectric interactions with the highly polarized $KNbO_3$.

Cohen et al. developed a Shell Model for relaxor ferroelectric (PMN-x PT), which is able to reproduce qualitatively the phase diagram as a function of the Ti concentration [53]. Thereby, the location of the morphotropic phase boundary is in agreement with experiments, while the extension of the concentration range, in which this phase appears, is too large within the model. The extension of the concentration range has to be adjusted by applying pressure on the system.

Shell Models for ferroelectric materials have been used for several different other properties, such as surfaces, grain boundaries, thin films and nanostructures. An early developed Shell Model in 1995 for $SrTiO_3$ predicted surface reconstruction [54]. This could never been verified experimentally or theoretically with electronic-structure calculations [55] [56]. Nevertheless, more recent Shell Model simulations of surface structures are in good accord with electronic structure calculations [57]. For example, the Shell Model from Tinte and Stochiatti for $BaTiO_3$ surface structure calculations was in good agreement with electronic structure calculations [58].

Reversion of polarization in ferroelectric materials is driven mainly by domain-wall motion and, to a less important portion, driven by a domain switching processes in a mono-domain. The latter can be studied by atomistic simulation. This has been done by Sepliarsky *at al.* in $KNbO_3$. In this study the microscopic processes that take place during polarization reversal in the tetragonal phase has been characterized [59]. At low temperature and low electric field this process occurs in a spatially coherent manner and a macroscopic intermediate states with orthorhombic symmetry is observed. At high temperature and strong electric field no well-defined macroscopic intermediate states take place.

To resume, the Shell Model has been successful in describing a wide range of ferroelectric phenomena. The ability of the Shell Model to reproduce the main features of classical perovskite ferroelectrics, such as phase transition sequence etc., shows that it contains the important physical ingredients of ferroelectricity. Furthermore, it has been possible to study more complex ferroelectric based systems, at least in a quantitative manner. These systems are ferroelectric solid solutions, superlattices, and ultrathin films. [60], [50], [58], [61]

1.4 Limits of the current models and Objectives

In the last decades, first-principle methods contributed intensively to the microscopic understanding of simple ferroelectric systems, such as perovskite ferroelectrics. The first-principle density functional calculations offer a powerful approach to determine several ferroelectric zero-temperature properties free from any experimental input. Nevertheless, the determination of temperature dependent ferroelectric properties, such as the sequence of phase transitions and respective temperatures, are hardly achieved with first principle techniques. Furthermore, the first-principle techniques are up to now limited in time- and length-scale on account of their high computational cost. However, most of the ferroelectric systems of technological interest are compounds of complex nano-structured solid solutions. Therefore, in order to perceive how the material properties are connected to their nanostructure, large scale-simulations are needed. In addition, defects can have an impact on the physical properties and are challenging to investigate through first principle techniques as this requires generally large simulation cells to capture defect-defect interactions.

First-principle based approaches, such as the effective Hamiltonian and the Shell Model have achieved comparable success in describing ferroelectric properties at finite temperatures. Both approaches are capable to simulate larger time and length scales compared to first principle techniques due to their reduced computational expense (see figure 1.5). The two approaches were able to describe the temperature driven phase transition diagrams of several ferroelectric compounds. Nevertheless, in both cases transition temperature differ from experimental findings and are related to a poor description of the thermal expansion. While the Shell Model provides spatially detailed information at the atomic scale, the effective Hamiltonian approach reduces the number of degrees of freedom. Therefore, before developing an effective Hamiltonian a prior understanding of the important degrees of freedom is necessary. This may present a challenging task, when one wishes to predict the physical properties of newly designed materials. Furthermore, the study of defects and surface effects using the effective Hamiltonian approach is difficult to carry out and extra terms to the effective Hamiltonian have to be included. Even if all atomic degrees of freedom are incorporated in the Shell Model, similar limits in its application come in great part from the use of partial charges. The use of partial charges makes indeed the variation of composition and the introduction of defects difficult (partial charge is not proportional to classical ionic charge). It is for instance impossible within the Shell Model to introduce at the same time a barium and oxygen vacancy in a straightforward way. While the parameters of the effective Hamiltonian are derived on separated DFT data-sets, the Shell Model parameters are determined through a multivariate fitting procedure and thus more sensitive to compensation errors.

In the present work, the objective is to develop a model at the atomic level that provides spatially detailed information without the heavy computational cost compared to first principle calculations. Therefore the Polarizable Ion Model that treats the ion as polarizable and nominal charged is employed. The use of formal charged ions should facilitate the study of defects, surfaces and complex solid solutions. By including the *ab initio* dipoles into the fitting procedure, hopefully, the different contributions to the inter-ionic interactions are faithfully reproduced. This could enhance the transferability of the inter-ionic potential.

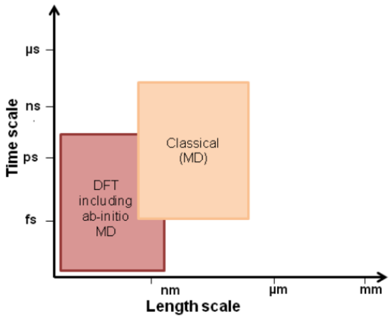

Figure 1.5: Time and length scale range for *ab intio* calculations and classical molecular dynamics simulations. [62]

Chapter 2

Polarizable Ion Model

Contents

THE Polarizable Ion Model (PIM) developed by Wilson and Madden in 1993 [1] aims at improving already existent pair potentials by taking into account the polarizability of ions. The total potential energy within the PIM is decomposed in four terms:

$$U = U^{\mathrm{Coulomb}} + U^{\mathrm{Disp}} + U^{\mathrm{Rep}} + U^{\mathrm{Pol}}. \tag{2.1}$$

The first term represents the Coulomb potential due to point charge-charge interactions, the second the dispersion, the third the short range repulsion and the last term the polarization potential. Forces can be derived from this potential and used in Molecular Dynamicss (MD) for finite temperature studies. In the following, each term of the total potential is discussed and explicit mathematical expressions are presented. A special consideration will be taken on the polarization term by illustrating how environmental effects present in ionic crystals can lead to a tractable

---

[1] and has been improved ever since.

model of induced multipoles for simulating ionic materials. In the last section of this chapter, the general procedure of the derivation of the parameter of the PIM is presented and concrete examples are given.

2.1 Principle of the Polarizable Ion Model

2.1.1 Charge-charge interaction

In the PIM, ions are treated as polarizable point charges that interact via Coulombic's law:

$$U^{q-q} = \sum_{i<j} \frac{q_i q_j}{r_{ij}} = \sum_{i<j} q_i \mathbf{T}_{ij} q_j. \tag{2.2}$$

In Equation 2.2 and throughout the work the following tensor notation is used:

$$\mathbf{T}_{ij} = (\mathbf{r_{ij}})^{-1} \tag{2.3}$$

$$\mathbf{T}_{ij}^{\alpha} = \nabla_\alpha \mathbf{T}_{ij} = -r_{ij}^{\alpha}(r_{ij})^{-3} \tag{2.4}$$

$$\mathbf{T}_{ij}^{\alpha\beta} = \nabla_\alpha \nabla_\beta \mathbf{T}_{ij} = (3r_{ij}^{\alpha} r_{ij}^{\beta} - (r_{ij})^2 \delta_{\alpha\beta})(r_{ij})^{-5} \tag{2.5}$$

$$\mathbf{T}_{ij}^{\alpha\beta\ldots\nu} = \nabla_\alpha \nabla_\beta \ldots \nabla_\nu \mathbf{T}_{ij} \tag{2.6}$$

where the indices α, β and γ represent the Cartesian axes x, y and z. The charge-charge interaction is by far the preponderant term in the total potential energy for ionic materials.

2.1.2 Dispersion

The dispersion potential includes terms up to dipole-dipole and dipole-quadrupole order:

$$U^{\text{Disp}} = -\sum_{i \leq j} \left[\frac{C_6^{ij} f_6(r_{ij})}{r_{ij}^6} + \frac{C_8^{ij} f_8(r_{ij})}{r_{ij}^8} \right]. \tag{2.7}$$

The Tang-Toennies damping functions $f_n^{ij}(r_{ij})$ are used to screen the dispersion interactions at short distance and given by the expression [63]:

$$f_n^{ij}(r_{ij}) = 1 - c^{ij} e^{-b^{ij} r_{ij}} \sum_{k=0}^{n} \frac{(b^{ij} r_{ij})^k}{k!}. \tag{2.8}$$

The free parameters are the strength coefficients C^{ij} and the parameters of the dispersion damping is b^{ij}, while $c^{ij} = 1$ (see fig. 2.1).

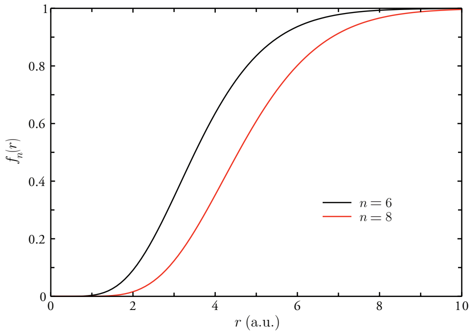

Figure 2.1: Tang-Toennies damping functions given by expression 2.8 with $c^{ij} = 1$ and $b^{ij} = 1.9$ (a.u.).

2.1.3 Short range repulsion

The short range repulsion is due to the Pauli exclusion principle. In the PIM code, different short range repulsive potentials are implemented. The short range potentials decay fast with distance r_{ij} and they are assumed to converge within the nearest periodic image convention.

Born-Mayer

The simplest description of the repulsion potential is the Born-Mayer potential, which treats the ion as rigid:

$$U^{\text{Rep}} = \sum_{i \leq j} A^{ij} e^{-a^{ij} r_{ij}} \tag{2.9}$$

where the parameter A^{ij} represents the strength of the repulsion between two ions i and j and the parameter a^{ij} determines the steepness of the repulsive wall.

Deformability-potential

In the Born-Mayer potential, the ion shape is considered to be rigid. Nevertheless, the ion adapt its electronic density to environmental changes. Thus, the shape of the repulsion wall depends on the instantaneous position of the surrounding ions.

The improved Born-Mayer potential accounts for the deformability of spherical and dipolar shape of the repulsion wall [64]:

$$U^{\mathrm{Rep}} = \sum_{i\in A, j\in C} B^{-+} e^{-a^{-+}\rho_{ij}} + \sum_{i,j\in A} B^{--} e^{-a^{--}r_{ij}} + \sum_{i,j\in C} B^{++} e^{-a^{++}r_{ij}} + \sum_{i\in A} \left[D^{-}\left(e^{\beta^{-}\delta_i} + e^{-\beta^{-}\delta_i} \right) + C^{-}\left(e^{\eta^{-2}|\epsilon_i|^2} - 1 \right) \right] \tag{2.10}$$

where

$$\rho_{ij} = r^{ij} - \delta_i - S^{ij}_{\alpha}\epsilon^{i}_{\alpha}. \tag{2.11}$$

The expression of the deformability potential 2.10 is exemplary given for a two-species system. The letter A and C stands for anion and cation, respectively. The cations are considered to be rigid, while the anion are deformable. The first three terms are the anion-cation, anion-anion and cation-cation short-range repulsions. The cation-anion summation depends on ρ_{ij}, the instantaneous distance between cation and anion charge densities, for which short range repulsion becomes relevant. In this term, δ_i is a variable characterizing the spherical breathing of the anion and stands for the deviation of the anion radius from its default value. The dipolar distortion is given by the set of three variables ϵ^{i}_{α}. $S^{ij}_{\alpha} = \frac{r^{ij}_{\alpha}}{r^{ij}}$ represents the interaction tensor. The last term includes the sum over self-energy terms representing the cost in deforming the charge density. The parameters β and η are effective force constants determining the stiffness of deforming. The magnitude of spherical breathing δ_i and dipolar deformation ϵ^{i}_{α} for fixed ion positions are determined by minimization of the deformability-potential.

2.1.4 Polarization potential

Ionic materials are very sensitive to environmental changes. Therefore, modelling of ionic materials needs a deep understanding of changes in the electronic structure of ions in condensed phase due to the interaction with neighbouring ions. First, isotropic compression effects on the electron density in a symmetric crystalline environment are examined. Second, polarization effects in less symmetric environments are discussed by decomposing the interaction in an asymptotic and short range term.

Ion compression in perfect crystal: symmetric environment

The ions, which constitute an ionic material, are very sensitive to environmental effects. These effects are responsible for the stabilization of oxide anions O^{2-} in the solid phase, while it is known to be unstable in the gas phase.[2] An anion placed in a perfect crystal of cubic symmetry is considered to illustrate the environmental effects of compression (see figure 2.2). Madden *et al.* characterized the anion-in-crystal polarizability by performing electronic structure calculations carried out on two levels of precision. First, the effect of a point charge crystal lattice on the anion polarizability (CRYS) and second, the short-range effect appearing by including fully described first cation shell density (CLUS), is examined. In table 2.1, *ab initio* coupled Hartree-Fock polarizabilities for some sample ions are given [66]. The results show a substantial reduction of the anion *ab initio* polarizabilities from the free state (FREE), to CRYS and finally CLUS.

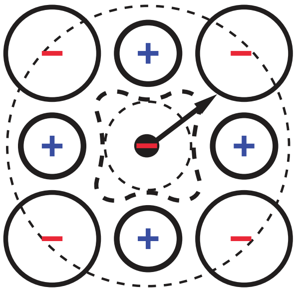

Figure 2.2: Schematic representation of anion and cation in a cubic crystal.

The decrease of the crystal polarizability can be explained as following. The electron cloud of the central anion is exposed to an electrostatic potential created by the lattice point charges constituting the crystal. The form of the potential acting on the electron cloud can be written as an expansion in cubic harmonics:

$$U(\mathbf{r}) = U_0(r) + \sum_{l>4} \sum_{m} U_l(r) Y_{l,m}(\mathbf{r}) \tag{2.12}$$

where $U_0(r)$ is a spherical potential and $U_l(r)Y_{l,m}(\mathbf{r})$ a potential for angular momentum with $l = 4$ or higher even terms. The spherical potential is dominant for sp valence ions, such as O^{2-}, where in spherical symmetry the closed shell ionic

---

[2] In the gas phase the following energy differences between ionized states are given: $\Delta U(O \rightarrow O^{-}) = -142\ kJmol^{-1}$, $\Delta U(O \rightarrow O^{2-}) = +844\ Jmol^{-1}$. The one electron ionized state is stable, while the two ionized state is unstable in free space, because of the infinite polarizability of O^{2-} [65].

ground state is S. [3] Thus, the electron cloud of the anion experiences a spherical confining potential. Therefore, the electrons are effectively more tightly bound in crystals relatively to free standing ion. This effect reduces thus the polarizability of the ion.

Table 2.1: *Ab initio* polarizabilities for anions in free state (FREE), in a lattice of point charges (CRYS), and with a fully described first cation shell (CLUS)

Anion	FREE	CRYS	CLUS
F^-	10.654	7.300	6.18
Cl^-	31.468	26.655	20.232
O^{2-}	"∞"	21.177	12.32

An additional contribution to the spherical potential acting on the electron cloud is given by the repulsion due to the electron density of the neighbouring ions (Pauli principle). The total spherical potential U_s compresses the electron cloud significantly and reduces further the polarizability of the anion (see figure 2.3).

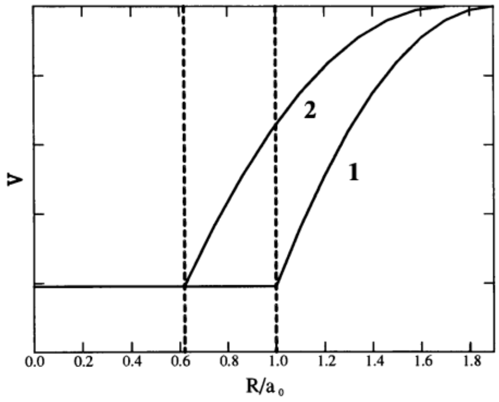

Figure 2.3: Potential felt by an electron in an anion at the origin due to the crystalline environment due to point charges only (CRYS: curve 1) and due to overlap terms (CLUS: curve 2). [66]

The crystal field has very little effect on the cation properties with respect to the free state, as the cation electrons tend to be more tightly bound compared to those in the anions due to the excess of positive nuclear charge. Therefore, the cation remains relatively unperturbed by the crystalline environment. In fact, *ab initio* calculations confirmed the small dependence of the cation polarizabilities to crystalline compression environmental effects [67].

---

[3] perturbation theory suggest mixing of S ground state with excited $l = 4$ G state, but occupation of such a high angular momentum orbital would energetically unfavourable for sp valence ions. Hence the degree of mixing with G is small [66]

Polarization effects

Simulation at finite temperature of ionic materials requires a detailed consideration of polarization effects in less symmetric environments. Taking again the cubic system of figure 2.2, thermal fluctuations may displace the ions from their perfect crystal lattice position. Such a distortion of the perfect cubic crystal affects the potential felt by the central anion. Thus, in the spherical expansion of equation's 2.12 angular momentum terms for $l = 0, 1$ and 2 have to be included, where $l = 1$ represents the deformation of dipole symmetry and $l = 2$ of quadrupole symmetry (or higher angular momentum terms). This results in induced dipoles and quadrupoles or higher multipoles.

The effect of how charge displacement induces dipoles on the central anion has been rationalized by Madden *et al.* by examining separately the different contributions to the total induced dipole moment.

First, the displacement of an ion asymptotic far away, i.e. at distances greater than the first coordination shell, is considered. The potential acting on the central anion electron density is affected through an induced field (E_β, $l = 1$) and field gradient ($E_{\gamma\beta}$, $l = 2$). The resulting dipoles $\mu^i_{\alpha,AS}$ and quadrupoles $\theta^i_{\alpha\beta,AS}$ of the central anion i are expressed according to the multipole expansion [68]:

$$\boldsymbol{\mu}_i^{\alpha,\mathrm{AS}} = \boldsymbol{\alpha}^{\alpha\beta} E^{\beta}(\mathbf{r}_i) + \frac{1}{3}\mathbf{B}^{\alpha\beta,\gamma\delta} E^{\beta}(\mathbf{r}_i) E^{\gamma\beta}(\mathbf{r}_i) + \ldots \tag{2.13}$$

$$\boldsymbol{\theta}_i^{\alpha\beta,\mathrm{AS}} = \frac{1}{2}\mathbf{B}^{\alpha\beta,\gamma\delta} E^{\gamma}(\mathbf{r}_i) E_{\delta}(\mathbf{r}_i) + \mathbf{C}^{\alpha\beta\gamma\delta} E^{\gamma\delta}(\mathbf{r}_i) + \ldots \tag{2.14}$$

where the superscripts α, β correspond to the Cartesian axes. The Einstein summation notation is used, i.e. repeated subscripts represent summation over the three values x, y and z of that subscript. The terms $\boldsymbol{\alpha}$ and $\mathbf{C}$ are the in-crystal dipole and quadrupole polarizabilities and $\mathbf{B}$ the dipole-dipole-quadrupole hyperpolarizability. For spherical ions, $\boldsymbol{\alpha}$, $\mathbf{B}$ and $\mathbf{C}$, can be specified by a single scalar.

Additional effects to the induced dipole moment occur for nearest neighbour distortions and corrections to the asymptotic multipoles have to be included. First, a point charge displacement in the first shell creates free space, in which the electron density can adapt. This effect is referred as 'the dent-in-wall correction', see figure 2.4.

By taking the spatial extension of the first shell ions into account, two more corrections are necessary. One originates from the failure of classical expansion of Coulomb potential when charge distributions of ions overlap, named as 'the Coulomb overlap correction'. Furthermore, the extend, to which the central ion

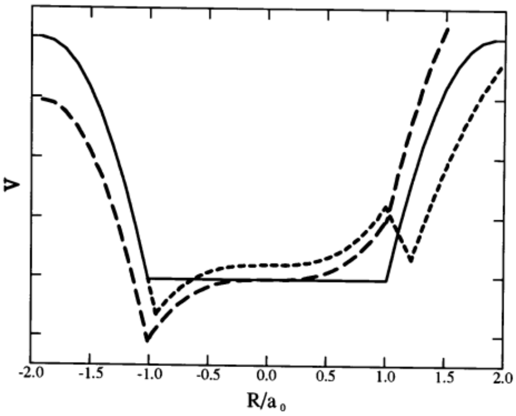

Figure 2.4: Potential felt by an electron in an anion at the origin in the first shell for a distortion outwards. Solid line: undistorted potential, long-dashed k=line: Coulombic induced potential after distortion, short dashed: total potential including short range 'dent-in-wall effect'. [66]

electron density penetrates the charge cloud of the surrounding first shell ion, is restricted by the Pauli exclusion principle, called 'the Exchange-repulsion-correction'.

Madden *et al.* performed electronic structure calculations in order to quantify the effect of each short range correction to the asymptotic multipoles. The details of the calculation can be found in [69]. These calculations show significant differences in the way cations and anions are polarized by the interactions with neighbouring ions. In the case of anions, the outward displacement of a neighbouring cation creates free space in which the anion electron density can adapt and opposites the asymptotic dipole. As a result of this effect, the dipole moment decreases [70]. The Coulomb overlap correction has an opposite effect to the previous discussed 'dent-in-wall-effect'. Calculations show a slight increase of the dipole moment, when anion and cation electron densities overlap. In fact, while the anion electron density penetrates the cations, the anion experiences an increased cation nuclear charge that creates a force on its electron density in the same direction as the asymptotic dipole moment. The most important portion to the short range correction to the asymptotic dipole moment, in the case of anions, is given by the Exchange-repulsion. The Pauli exclusion principle prohibits the regions occupied by the cation charge density. Therefore, 'the Exchange-repulsion-correction' creates a force in the opposite direction as the asymptotic dipole and reduces its value. As the exchange-repulsion overwhelms the other short range effects, the total dipole moment is reduced. In alkali metal halide, the reduction can be around $\sim 40\%$ [71] [70].

The cations have a more bounded nature of the electron density than the anions.

They are therefore less sensible to changes in the confining potential due to a displacement of neighbouring point charges. Therefore 'the dent-in-wall correction' is almost negligible. Madden *et al.* calculated for different cation size the Coulomb overlap and Exchange-repulsion correction. The Exchange-repulsion force drives the electrons in the same direction as the asymptotic dipole moment, while the Coulomb overlap-correction enhances the asymptotic dipole moment and increases with the cation size. In contrast to the anions, both effects are of similar magnitude. The sign of the total net short range correction can change for different alkali metal cations. The corrections to the asymptotic dipole are found to be around $10\% - 25\%$.

Madden *et al.* modelled the total dipole moment, as the sum of the asymptotic dipole moment and a short range dipole moment, that has to account for the corrections due to nearest neighbour interactions. In this model, the short range dipole is considered to arise from a "field" acting through the ionic polarizability:

$$\boldsymbol{\mu}_i^{\alpha,\mathrm{SR}} = \boldsymbol{\alpha} E_{\boldsymbol{\alpha}}^{SR} \tag{2.15}$$

where the short range 'field' $E_{\boldsymbol{\alpha}}^{SR}$ is taken to be the product of the asymptotic field in equation 2.13 and a correction factor, which enhances or reduces the asymptotic dipole moment depending on the sign of the parameter c^{ij}:

$$E_{\boldsymbol{\alpha}}^{SR} = E_{\boldsymbol{\alpha}}^{AS} \left[c^{ij} e^{-b^{ij} r_{ij}} \sum_{k=0}^{n} \frac{(b^{ij} r_{ij})^k}{k!} \right] . \tag{2.16}$$

Within this choice, the total dipole $\boldsymbol{\mu}_i^{\alpha}$ moments is given by:

$$\boldsymbol{\mu}_i^{\alpha} = \boldsymbol{\mu}_i^{\alpha,\mathrm{AS}} + \boldsymbol{\mu}_i^{\alpha,\mathrm{SR}} = \boldsymbol{\mu}_i^{\alpha,\mathrm{AS}} \left(1 - c^{ij} e^{-b^{ij} r_{ij}} \sum_{k=0}^{n} \frac{(b^{ij} r_{ij})^k}{k!} \right) . \tag{2.17}$$

The polarization part of the potential including only dipolar effects by incorporating the expression of the total dipole moment 2.17 is given by:

$$\begin{aligned} U^{\mathrm{pol}} &= \sum_{i,j} \left(q_i \mu_j^{\alpha} f_4^{ij}(r_{ij}) - q_j \mu_i^{\alpha} f_4^{ji}(r_{ij}) \right) \mathbf{T}_{ij}^{\alpha} \\ &\quad - \sum_{i,j} \mu_i^{\alpha} \mu_j^{\beta} \mathbf{T}_{ij}^{\alpha\beta} + \sum_i \frac{1}{2\alpha_i} \mid \boldsymbol{\mu}_i \mid^2 . \end{aligned} \tag{2.18}$$

The terms $\mathbf{T}_{ij}^{\alpha}$ and $\mathbf{T}_{ij}^{\alpha\beta}$ are the charge-dipole and dipole-dipole interaction tensors from equations 2.4 and 2.5, respectively. Here, α_i is the polarizability of ion i and $\boldsymbol{\mu}_i$ are the asymptotic dipoles. The charge-dipole asymptotic terms are corrected for the above explained short range effects by the means of Tang-Toennies damping functions $f_n^{ij}(r_{ij})$ as used in eq. 2.17 [63]:

$$f_n^{ij}(r_{ij}) = 1 - c^{ij} e^{-b^{ij} r_{ij}} \sum_{k=0}^{n} \frac{(b^{ij} r_{ij})^k}{k!}. \tag{2.19}$$

The parameters b^{ij} define the distance at which the overlap of electron density takes place and are thus the same for cations and anions, i.e. $b^{ij} = b^{ji}$. The parameters c^{ij} determine the strength of correction to the asymptotic dipole moment. For anions, overlap effects by displacing first cation shell reduce dipole moments and therefore the parameter c^{ij} is positive defined. In the case of cations, the sign of net short-range dipole is unpredictable and depends on the particular ion species. Thus c^{ji} can take either positive or negative values.

Until now, only the electronic densities of central ion was treated as polarizable while those of the neighbouring ions were considered to be 'frozen'. But in reality, the induced multipoles on the central ion induced by the displacement of another ion generates itself an electric field, which affects the electronic density of surrounding ions, and these in turn affects further the polarization of the central ion. These coupled many-body interactions are not analytical solvable. Thus the instantaneous values of the dipole moments are obtained by minimizing the polarization potential given in expression 2.18. In general, for the minimization the conjugate gradient algorithm is used providing a faster convergence. Nevertheless, in this work it has been noticed that the conjugate gradient method fails for less polarizable ions as titanium. In this case, a more robust method of minimization is the simple gradient descent algorithm. (For details of the algorithms see for example [72].)

2.1.5 Truncation and Ewald summation

Cut-off radius

In the PIM the ionic material is simulated using periodic boundary conditions. Considering a given particle i in the simulation cell, it interacts with all the other particles of the infinite periodic images and with all the particles of the same cell. The PIM interaction potential is pairwise additive and thus the potential energy of a cubic simulation cell containing N particles is [73]:

$$U^{\mathrm{Tot}} = \frac{1}{2} \sum_{i,j,\mathbf{n}}{}^{\prime} U(|\mathbf{r}_{i,j} + n_\alpha L_\alpha|) + \sum_i \frac{1}{2\alpha_i} \mid \boldsymbol{\mu}_i \mid^2 \tag{2.20}$$

with L_α the simulation cell length in α direction and $\mathbf{n}$ an arbitrary vector of the three integer numbers. The prime symbol over the sum means that the interaction of a particle with itself $i = j$ for $n = 0$ is excluded.

If the potential decreases rapidly with the interatomic distance $r_{i,j,\mathbf{n}}$, a cut-off distance can be defined. Above this distance the interactions are considered to be negligibly small. Hence, the infinite sum in equation 2.20 is approximated by a finite sum.

The nearest periodic image convention takes into account the interaction of all particles in a simulation cell with the nearest image, i.e. the cut-off distance is equal (or less) than the length of the simulation cell. The short-range repulsion decays exponentially fast with distance and is thus dealt with the nearest periodic image convention.

Ewald summation

In contrast to the short range repulsion, the sum over Coulomb interactions given in equation 2.2 decays slowly with distance $1/r_{ij}$ and can therefore generally not be considered to converge within the nearest periodic image convention for a typical, computational reasonable, size of simulation cells. Furthermore, the sum is conditionally convergent, i.e. the result depends on the order in which the terms are added up. Thus, numerically tricks must be used to evaluate the electrostatic energy of the simulation box. Therefore, the long-range interaction terms are treated in the framework of the Ewald summation. The Ewald summation formula is a method for computing long-range interactions in periodic systems. The main idea is to split the sum into a real space contribution and a reciprocal space contribution, which are both well convergent. Therefore, the following identity is used:

$$\frac{1}{r} = \frac{1 - f(r)}{r} + \frac{f(r)}{r}. \tag{2.21}$$

The distribution $f(r)$ has to be chosen in such a way, that on one hand the first term decays fast with rising r. In this case, its contribution in real space is negligible above a cut-off distance. On the other hand, for large values of r the second term should be smooth in order to describe it with few Fourier terms in reciprocal space. The distribution $f(r)$ is conveniently chosen to be Gaussian. [74] Within this decomposition the charge-charge potential becomes [75]:

$$U^{\mathrm{Real}} = \sum_i \sum_{j>i} \left(q_i \widehat{\mathbf{T}}_{ij} q_j \right). \tag{2.22}$$

The circumflex accent over the tensor stands for its screened version given by:

$$\widehat{\mathbf{T}}_{ij} = \widehat{\frac{1}{r_{ij}}} = \frac{erfc(\kappa r_{ij})}{r_{ij}} \tag{2.23}$$

where κ is the smearing parameter and $erfc$ is the complementary error function:

$$\text{erfc}(r) = 1 - \text{erf}(r) = \frac{2}{\sqrt{\pi}} \int_r^\infty e^{-t^2} dt. \tag{2.24}$$

The contributions in reciprocal space has the following expression:

$$U^{q-q}_{\text{Recip}} = \frac{4\pi}{V} \sum_{h>0}^{\infty} \frac{e^{-h^2/4\kappa^2}}{h^2} \left(\left[\sum_i q_i \cos(\mathbf{h} \cdot \mathbf{r}_i) \right]^2 + \left[\sum_i q_i \sin(\mathbf{h} \cdot \mathbf{r}_i) \right]^2 \right) \tag{2.25}$$

where the sum is taken over the reciprocal lattice $\mathbf{h} = 2\pi \left(i\hat{\mathbf{x}}/L_x + j\hat{\mathbf{y}}/L_y + k\hat{\mathbf{z}}/L_z \right)$. V is the simulation cell volume $|L_x \cdot (L_y \times L_z)|$.

The reciprocal sum given in eq. 2.25 includes the interactions of each particle with itself. This erroneous interaction has to be corrected by subtracting the sum by a so called self-energy term:

$$U^{q-q}_{\text{Self}} = \frac{\kappa}{\sqrt{\pi}} \sum_i (q_i)^2. \tag{2.26}$$

In the previous expressions the smearing parameter κ has been introduced. It is an adjustable parameter that represents an inverse length and determines the width of the Gaussian distribution. A large κ value means that the distribution around the point charges is sharp and thus a faster convergence in real space is achieved. Simultaneously, increasing the κ value strengthened the interaction between the charge distribution in the reciprocal space. Hence, more k-space terms are necessary to assure convergence in reciprocal space. In a simulation, the aim is to choose a compromising value of κ and the number of k-space terms, such as both sums in real and reciprocal space, converge under reasonable computational effort. It is important to check convergence of the Ewald sum for each individual system before beginning a calculation.

In the form of the Ewald formula, which is presented here, the surface term has been omitted by taking the 'tin-foil' boundary condition, i.e. the Ewald sphere is surrounded by a perfect conductor [9] [76].

The Ewald summation formula, exemplary discussed for the Coulomb interaction term, is applied for all electrostatic interaction and for dispersion. Exact derivation of the expression in real and reciprocal space are derived in [77].

Nomenclature of the model types

In the following, the nomenclature for the different model types derived by Madden *et al.* are listed. This nomenclature is used throughout the present work.

1. RIM:

The Rigid Ion Model treats the ions as rigid and non polarizable species. Ions interact via the charge-charge potential eq. 2.2, the Born-Mayer short range repulsion eq. 2.9 and the dispersion term eq. 2.7.

2. DIPPIM:

The DIPole Polarizable Ion Model improves the RIM by including the polarizability of the ions. Additional to the RIM potential interaction terms, the polarization potential is included in DIPPIM given by eq. 2.18.

3. DAIM:

The Dipolar Aspherical Ion Model includes deformability and polarizability at the dipolar level. The interaction potential equals the DIPPIM but instead of the Born-Mayer potential the deformability-potential given in expression 2.10 is used.

4. AIM:

The Aspherical Ion Model includes deformability and polarizability up to the quadrupolar level. Exact expressions of the AIM can be found in reference [78].

2.2 General derivation procedure for the PIM parameters

In this section, the parametrization of the interaction potential described in the previous section will be discussed. Two different fitting methodologies for the derivation of the PIM potential are used in literature. In this section, both methods are exposed and examples of their applications are discussed.

2.2.1 Global Fit: Fitting all parameters at the same time

The general procedure for developing a PIM is performed by fitting the free parameters on a set of *ab initio* reference data. The first step consists in the creation of *ab initio* reference data. Therefore, different configurations of the specific material are chosen in order to cover a wide range of thermodynamic states (coordination number, temperature, pressure etc.). This large number of different thermodynamic conditions is expected to lead to a greater transferability of the PIM potential. DFT calculations are performed on each of these configurations. Then, the forces acting on the ions and the stress tensors are extracted from the DFT calculations. Furthermore, the Wannier analyse applied to the Kohn-Sham eigenfunctions permits the determination of dipole moments associated to each ion [79]. In contrast to the Kohn-Sham eigenfunction, which are non-localized and periodic in space, the maximally-localized Wannier functions are localized around the ion and goes rapidly to zero with increasing distance to the ion. The dipole moment is determined from the position of the center of the maximally localized Wannier functions around an ion.

Once the set of *ab initio* reference data obtained, the fitting procedure is undertaken. In the global fit, all parameters of the potential are simultaneously determined by minimizing the total objective function. The total objective function is the weighted sum of three partial objective functions A_F, A_S and A_D. The weight between the partial objective functions are tunable in the code. The partial objective functions are a measure of the error between the reference DFT dipoles ζ^{DFT}, forces F^{DFT} and stresses S^{DFT} and the model results ζ^{PIM}, F^{PIM} and S^{PIM} for a given set of parameters $\{\chi\}$:

$$A_F\left(\{\chi\}\right) = \frac{\sum_{i,\theta,A}\left|F_{i,\theta}^{A,PIM}\left(\{\chi\}\right) - F_{i,\theta}^{A,DFT}\right|^2}{\sum_{i,A}\left|F_{i,\theta}^{A,DFT}\right|^2} \tag{2.27}$$

$$A_S\left(\{\chi\}\right) = \frac{\sum_{k,A}\left|S_k^{A,PIM}\left(\{\chi\}\right) - S_k^{A,DFT}\right|^2}{\sum_A\left|S_k^{A,DFT}\right|^2} \tag{2.28}$$

$$A_D\left(\{\chi\}\right) = \frac{\sum_{i,\theta,A}\left|\zeta_{i,\theta}^{A,PIM}\left(\{\chi\}\right) - \zeta_{i,\theta}^{A,DFT}\right|^2}{\sum_{i,A}\left|\zeta_{i,\theta}^{A,DFT}\right|^2} \tag{2.29}$$

where i runs over the atoms in a configuration A, θ over the Cartesian coordinates x, y, z and k over the stress tensor components. The minimization of the total objective function is performed with a non-gradient simplex and MIGRAD method as implemented in the package MINUIT [80], [3]. These methods use χ^2 testing to compare the *ab initio* reference data to the model obtained results. In figure 2.5 the general fitting methodology is illustrated.

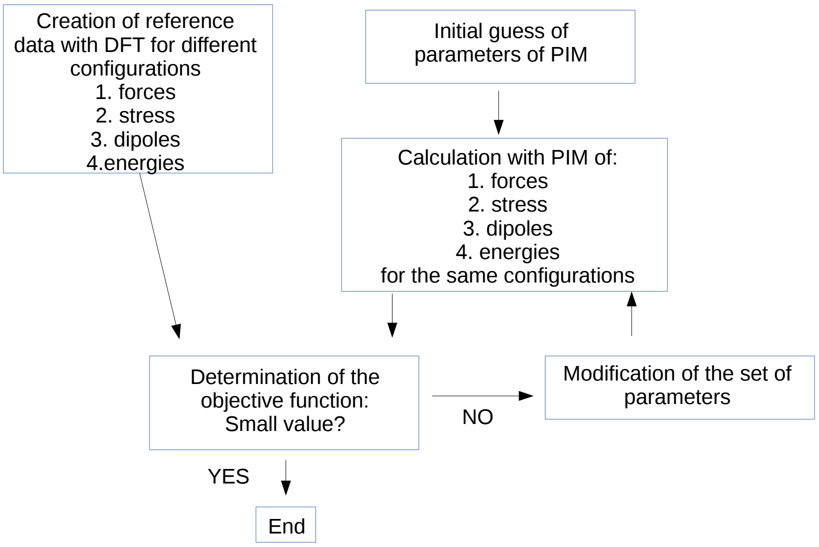

Figure 2.5: Chart illustration of the fitting procedure generally used for the derivation of PIM parameters.

Example of Alkaline earth oxides CaO, SrO and BaO

In 2003, Madden *et al.* presented AIM potentials for three alkaline earth oxides: CaO, SrO and BaO [78]. These compounds involve heavy cations, thus polarization and deformation effects are expected to be important. The AIM potential includes polarization effects up to quadrupole order. Furthermore, deformation of dipolar and quadrupolar symmetry are taken into account in the short range repulsion term between unlike ions. The potential was derived by a Global Fit on *ab initio* forces and stresses (see previous section). For each material nine reference configurations at different pressures (0 - 80 GPa), temperatures (300-2000 K) and coordination environments (sixcoordinated (B1:rocksalt), eight-coordinated (B2: CsCl) and four-coordinated (B3: zinc blende) including each around 200 ions. The Global fitting procedure leads to values of the force component of the objective function less than 0.05 and for the stress component less than 0.002. Madden *et al.* compared the dipole moments of the SrO AIM to the DFT dipole moment, which were excluded in the fitting procedure and conclude because of their accurate descriptions (see FIG.2. in [78]) that for this material the fitting procedure leads to reliable parameters.

The AIM potential for CaO was shown to be transferable in temperature, as the thermal expansion were accurately reproduced on a temperature range between 300 K and 3000 K.

Furthermore, the quality of the AIM potentials for static results such as lattice constants, bulk moduli, elastic constants, phase transition pressures from B1 to B2 phase and phonon dispersion curves was in overall accurate accordance to experiment. Madden *et al.* highlighted in this work the necessity of including deformation effects in alkaline oxide with heavy cations. In fact, it has been demonstrated that the omission of deformation term in SrO leads to non negligible discrepancy in the phonon dispersion relation.

A special focus in this work of Madden *et al.* has been put on the pressure induced phase transition in BaO. Experimental measurements at room temperature reveals that BaO undergoes two phase transitions with increasing pressure [81]. First, around 10-15 GPa, the rocksalt BaO B1 phase becomes hexagonal of NiAs type, i.e the space group is $P6_3/mmc$ with a c/a ratio around 1.75. A second phase transition is observed around 18 GPa towards a PH_4I type tetragonally distorted B2 phase. By further increase of pressure from 20 to 60 GPa, the distorted B2 cell converges toward the perfect B2 phase without fully reaching it at 60 GPa. At high pressure Madden *et al.* expect an orthorhombic PH_4I type phase. This assumption is based on experimental and theoretical observations at high pressure of the appearance of such a orthorhombic phase in CsI, which is a material closely similar to BaO.

In order to analyse the pressure induced phase transitions of BaO with the AIM, Madden *et al.* first performed static energy calculation at different lattice volumes for all crystallographic phases at zero Kelvin temperature. The relative stabilities between the phases taking the enthalpy of B1 phase as reference does not fully follow the experimental phase transition sequence (B1 phase, hexagonal, orthorhombic PH_4I, tetragonally distorted B2 phase). Furthermore, the model predicts the stabilization of the perfect B2 phase already at 25 GPa, while experimentally at least until 60 GPa the structure is observed to be tetragonally distorted. Madden *et al.* showed with Molecular Dynamics calculations at 300 K that entropic effects related to thermal fluctuations become important for such a flat enthalpy surface. In fact, he observed that the system switches between two orthorhombic configurations so that in average the structure is tetragonal. By increasing pressure, the amplitude of the oscillation is decreasing and an orthorhombic distorted phases is obtained. Thus at finite temperature the correct sequence of phase transition order is obtained. Nevertheless, transition pressures are not accurately described with the AIM, as the enthalpy differences are of the order of 10^{-5} Hartree/molecule and thus lays below the expected accuracy of the model. In conclusion, this work about alkaline-earth oxide materials shows that, for this class of materials, it is possible to develop transferable potentials within the global fitting procedure on forces and stress. Furthermore, the model describes the correct order of the complex pressure-driven phase transition in BaO at finite temperature. Moreover, additional microscopic insights in the transition mechanisms are gained by revealing that entropic effects are important. However, phase transition pressures are not accurately reproduced.

TiO_2

Recently, Corradini *et al.* published a DIPPIM for SiO_2 and TiO_2 within a Global fit methodology on forces and stresses. Details of the development of the model can be found in [82]. In this work, two features are interesting to point out. First, the model was derived by a global fitting procedure that includes both materials at the same time. Therefore, the set of parameters of the oxide ion are used in both materials. This ensures the transferability to simulate materials compositions including both materials. The validation of the potential has been carried out at zero Kelvin by computing the energy versus volume E(V) curves, i.e. the atomic positions are optimized at fixed volumes, for each polymorph. In the case of TiO_2 the three main polymorphs are the anatase, rutile and brookite structures. The energy minimum of the curvature corresponds to the zero Kelvin equilibrium structures. The DAIM cell parameters are in good agreement with experimental values. Their relative error is less than 2.5 % except for the anatase phase of TiO_2, for which the c cell parameter is overestimated by 7%. Nevertheless, the c cell parameter value is consistent with the PBE functional cell parameter. The energy difference of the minima in the E(V) gives the relative stability of the different polymorphs. In the case of TiO_2 experimental results find the order of stabilization energies: $E_{rutile} < E_{brookite} < E_{anatase}$ [83] [84]. The PBE functional is not able to reproduce the right order of stabilization: $E_{anatase} < E_{brookite} < E_{rutile}$ [85]. The DIPPIM neither reproduces the experimental nor the PBE order of stabilization: $E_{anatase} < E_{rutile} < E_{brookite}$. Tangney, Scandolo and co-workers have also parametrized a Force Field (FF) for TiO_2 on DFT forces, energies, and stresses in the rutile crystal structure [85]. This force field predicts the same order of stabilization as experimental results, but overestimates strongly the energy differences. This example shows the difficulty to reproduce the correct stabilization order with DFT and force fields for materials, where the energies difference between the different polymorphs are of the order of meV/TiO_2 and which are related to small volume changes of the order of some Å^3/TiO_2 (see fig. 2.2).

Table 2.2: Energy differences of the three polymorphs in meV/TiO_2

Phase	Expt.[83] [84]	DFT[85]	DIIPIM[82]	FF[85]
$E_{anatase}$ - E_{rutile}	35.0, 53.8	-53.4	-4.1	425.9
$E_{brookite}$ - E_{rutile}	7.7	-47.3	44.5	212.6

2.2.2 Separated Fitting procedure

The PIM involves generally a great number of free parameters. The difficulty remains in finding a transferable set of parameters. Therefore, Madden presented in 2003 an improved fitting procedure for the PIM potential [64]. In this procedure, the process of fitting is split up in two parts. First, the free parameters of the polarization term are fitted on the dipoles (or higher multipoles) by minimizing the objective function given by the expression 2.29. In the second step, these parameters are kept fixed, while both short range repulsion and dispersion are varied in order to minimize the objective functions for force and stress, eq. 2.27 and eq. 2.28 respectively. The ability to fit separately parameters should reduce eventual compensation errors and should hopefully lead to values, which reflect the physical intrinsic properties and thus result in a higher transferability.

In order to evaluate the efficiency of both fitting methodologies, Madden *et al.* developed two AIM potentials exploratory for MgO. Firstly, an AIM with the

Global methodology by fitting only on forces [78] and secondly, an AIM with the separated fitting methodology. The separated fitting methodology has been carried out with three crystal structures with different coordination environments as reference configurations, each containing 54 atoms. The atoms in these configurations have been displaced by performing high temperature MD calculations at 1500 K. Forces, stresses and dipoles have been calculated using DFT with PW91-GGA exchange correlation as implemented in the CASTEP code (Cambridge Serial Total Energy Package) [86] [87]. The MgO is modelled with the AIM, i.e. induced dipoles and quadrupoles are included and the ions are considered to be compressible. First, the parameters of the polarization part of the AIM potential have been fitted on the *ab initio* dipoles and quadrupoles. The value of the dipole and quadrupole objective function is $A_p = 0.02$. In the second step, the remaining parameters are fitted on forces and stresses. All parameters entering in the short-range repulsion are taken into account. Madden *et al.* assume that DFT calculations include dispersion effects and thus the damping parameters are included into the fit. However, the dipole-dipole C_6^{ij} and dipole-quadrupole C_8^{ij} strength coefficients are taken from reference [88] and [89].

Madden *et al.* compare the AIM with separated fitting procedure to the AIM derived by a fit only on forces [78]. The force-fitting AIM reproduces accurately the phonon dispersion relation and the equation of state over a wide range of temperature. Furthermore, the set of parameters of the model were transferable to MgO/-CaO mixed crystals. The comparison of both models reveals that the set of parameters obtained through the separated fitting procedure differs from those of the force-fitting AIM. Nevertheless, Madden *et al.* believe that the difference between both AIMs can be considered to be small, if relevant functions, such as the phonon dispersion curve, are described with similar precision. The phonons reflects the energetics of the crystal for low-symmetry ionic configuration, where polarization and aspherical deformation effects are important. The strength of these effects varied at different points in the Brillouin Zone. The plot of the phonon dispersion relation shows that both AIMs result in good agreement compared to experiment [90]. The AIM derived by separated fitting gives rise to a further accordance with experiment in the optic branches. Therefore, Madden *et al.* assume that this model should at least result in the same precision as the force-fitting AIM for the description of the equation of state and the transferability to MgO/CaO mixed crystals. Madden *et* *al.* show with this work on the exemplary MgO crystal that the derivation of accurate and transferable models with the separated fitting procedure for 'simple'[4] oxide materials is possible.

2.3 Conclusion

In conclusion, the PIM presents a powerful tool for modelling ionic materials at large time and length scales compared to DFT. The PIM includes complex many-body effects through the polarization term, which includes both asymptotic and short range effects. Two different fitting procedures used in literature have been presented, the global fit and the separated fit. The global fitting procedure has been successfully applied to alkaline earth oxides CaO, SrO and BaO and was shown to be able to reproduces lattice constants, elastic constants and phonon dispersion curves. In addition, the PIM potential for BaO allowed further insight into the microscopic mechanisms of the pressure driven phase transition for BaO. In the case of TiO_2, the PIM developed with the global fitting procedure fails to reproduce the experimental and the theoretical order of stabilization energy. This points out the challenging task to develop reliable PIM for reproducing of correct description of phase transition order related to small differences in structure and relative stabilization energies of the order of some meV/unit formula. The separated fitting procedure was used by Madden *et al.* for MgO. The model reproduced accurately the phonon dispersion relation and the equation of state over a wide range of temperature. In addition, the set of parameters are transferable to MgO/CaO mixed crystals. In conclusion, although it might be a challenging task to develop a reliable interaction potential for $BaTiO_3$ with its complex phase transition sequence, it represents an attractive attempt considering the advantages of the PIM in terms of length and time scales and the use of formal charges.

---

[4] Simple in the sense that this kind of oxides shows stronger ionic character compared to more complex oxides as TiO_2.

Chapter 3

Development

Contents

IN the first part of this chapter, the technical details of the DFT calculations are presented. Then the ground state properties are determined and compared to DFT results in the literature and experimental findings. This section is followed by an investigation about the reasonable use of nominal charged ions for the modelling of the ferroelectric $BaTiO_3$. The second part of this chapter deals with the development of a Polarizable Ion Model for $BaTiO_3$.

3.1 DFT calculations

3.1.1 Technical details and ground state properties of $BaTiO_3$

In this section, the technical details of the DFT calculations are presented. The convergence of these calculations with respect to the plane wave cut-off energy, k-point-mesh density, and break criteria are studied. Furthermore, structural properties and energetics of $BaTiO_3$ are investigated. Comparison to experimental and other theoretical results gives conclusion about whether DFT calculations performed in the framework of this thesis are accurate enough to capture ferroelectricity. Furthermore, the geometry optimized structures are used in the next section for the creation of a reliable set of configurations for the development of a PIM for $BaTiO_3$.

Technical details for DFT calculations with VASP

In this work, DFT calculations were carried out with the Vienna Ab-initio Simulation Package (VASP). The advantage of the VASP code is that it includes a reliable set of pseudopotentials covering the periodic table. In this work the pseudopotential in the framework of Projector Augmented-Wave method (PAW) is used [91] [92]. The $2s$ and $2p$ levels of oxygen, $5s$, $5p$ and $6s$ levels of barium, and the $3p$, $4s$ and $3d$ of titanium are treated as valence states. Furthermore, DFT calculations are performed using the PBEsol exchange correlation functional [12]. The choice of this functional is based on the discussion in section 1.1.6, which revealed that the PBEsol is a suitable functional for the calculation of ground state properties of $BaTiO_3$. The k-point sampling in the Brillouin Zone is performed using the Monkhorst Pack scheme within the automatic mesh generation [93].

The phase transition sequence in $BaTiO_3$ is known to be very sensitive to changes in volume, i.e. very sensitive to stress. Thus, high precision of the DFT output quantities (energy, stress and force) is required. Therefore, the convergence of DFT output quantities are tested by varying successively the plane wave cut-off energy, energy difference break criteria and k-point-mesh density for a rhombohedral unit-cell, where atoms are slightly displaced from their ideal positions.

In table 3.1, the DFT results of the convergence test are presented. The first row contains the energy in eV/$BaTiO_3$. All force and stress tensor components exhibit a similar convergence behaviour. Therefore, only the x-component of the force vector of one of the oxygen ions and a diagonal (xx) and non-diagonal (xy) component of the stress tensor are exemplary listed in the table.

In the first part of the table, the plane wave cut off energy E_{cut} was varied from 600 to 900 eV, while keeping the other parameters constant. Convergence of force and stress components are achieved up to 10^{-6} a.u. for E_{cut}=900 eV. The energy exhibits a precision of 10^{-2} eV/$BaTiO_3$.

In VASP the self consistent DFT calculation loop 1.1 is stopped if the total energy change and the band structure energy change ('change of eigenvalues') between two steps are smaller than a global break condition, called E_{diff}. In the second part of the table, the break condition E_{diff} is varied between 10^{-4} and 10^{-8}. For

Table 3.1: *Ab initio* convergence table of the energy in eV/BaTiO$_3$, as well as x-force and xx- and xy stress tensor components in a.u.

	Energy	force	stress xx	stress xy
E$_{cut}$ [eV] (with E$_{diff}$ = 1.d-6 eV, k=6x6x6)				
600	-40.112809	0.001816	-0.000289	-0.000012
700	-40.120362	0.001815	-0.000289	-0.000012
800	-40.122504	0.001811	-0.000284	-0.000012
900	-40.122082	0.001809	-0.000281	-0.000012
1000	-40.122154	0.001809	-0.000281	-0.000012
E$_{diff}$ [eV] (with E$_{cut}$ = 900 eV, k=6x6x6)				
10^{-4}	-40.122062	0.001831	-0.000282	-0.000012
10^{-5}	-40.122078	0.001816	-0.000281	-0.000012
10^{-6}	-40.122082	0.001809	-0.000281	-0.000012
10^{-7}	-40.122083	0.001806	-0.000281	-0.000012
10^{-8}	-40.122083	0.001807	-0.000280	-0.000012
k-points (with E$_{cut}$ = 900 eV, E$_{diff}$ = 1.d-6)				
4x4x4	-40.128814	0.001532	-0.000280	-0.000012
5x5x5	-40.121113	0.001876	-0.000282	-0.000012
6x6x6	-40.122082	0.001809	-0.000281	-0.000012
7x7x7	-40.122029	0.001835	-0.000281	-0.000012
8x8x8	-40.122008	0.001825	-0.000281	-0.000012

E$_{diff}$=10^{-6}, the force component is converged to 10^{-5} a.u. and the stress components to 10^{-5} a.u.. The energy is given with a precision of 10^{-5} eV/BaTiO$_3$.

In the last part of the table, the results for different k-point mesh densities going from 4x4x4 to a 8x8x8 k-mesh are listed. The force component convergence with respect to the k-point mesh is more sensitive. Thus, only a precision of 10^{-4} a.u. is reached in this range of k-point mesh densities. The stress tensor components are converged to 10^{-6} a.u. up from k=6x6x6. The energy achieves an accuracy of 10^{-2} eV/BaTiO$_3$.

Throughout this work, the DFT calculations are carried out with a plane-wave cut off set to 900 eV. The Brillouin Zone integration is performed using a 6x6x6 k-point mesh for unit cells with cell parameters around 4.0 Å and the break criteria of the self-consistent loop is taken to be E$_{diff}$=10^{-6}. Within this setting a convergence for the energy of 10^{-2} eV/BaTiO$_3$ is achieved. The forces are converged to 10^{-4} a.u. and the diagonal components of the stress tensor to 10^{-5} a.u. and the off-diagonal components to 10^{-6} a.u.. Within this settings satisfying convergence is achieved.

Ab initio Geometry optimization

In this section, *ab initio* geometry optimization of the four phases of $BaTiO_3$ is presented in order to determine the accuracy of the structural properties of the DFT calculations. The geometry optimization relaxes all degrees of freedom consistent with the space group of the respective phases. In the VASP code, the space group of the supercell is automatically determined. During the geometry optimization, the force, stress tensor, cell shape and cell volume are optimized. Ion positions according to their Wyckoff positions are relaxed using selective dynamics in the VASP code. The relaxation process is stopped, when all forces acting on the ions are smaller than 0.001 eV/Å.

The cubic phase has the space group $Pm3m$ and the fractional coordinates of the atoms are given in table 3.2. As the atomic positions are imposed by symmetry, the only degree of freedom, which is relaxed in the cubic phase, is the lattice parameter a.

According to the displacive model picture of phase transition, the titanium atom is slightly displaced from its center position along the polar axis in each of the three ferroelectric phases.

In the tetragonal phase of space group $P4mmm$, two oxygen atoms, O2 and O3, are equivalent by symmetry. Thus, there exists in total five degrees of freedom: the cell parameters a and c and the three displacement parameters Δ_{O1}, Δ_{O2}, and Δ_{Ti}.

The orthorhombic phase has a space group of $Amm2$. The orthorhombic lattice parameters a,b and c, are related to the equivalent pseudo-monoclinic parameters a_m, c_m, and α by the following equations:

$$a = a_m \tag{3.1}$$

$$b = 2\ c_m\ \sin(\alpha/2) \tag{3.2}$$

$$c = 2\ c_m\ \cos(\alpha/2). \tag{3.3}$$

The quantities, that were optimized, are the lattice parameters a_m,c_m, the angle α, and displacements Δ_{O1}, Δ_{O2}, Δ_{O3}, and Δ_{Ti}.

In the rhombohedral phase of space group $R3m$, all oxygen ions are equivalent. Thus, the relaxed degrees of freedom were Δ_{O1}, Δ_{O2}, and Δ_{Ti}, the cell parameter a and the angle α.

The results of the structural optimizations are shown in table 3.3. The here performed PBEsol DFT calculations are compared to previous DFT calculations carried

Table 3.2: Atomic positions in fractional coordinates in the four phases of $BaTiO_3$

Cubic phase	Position		
O1	(0.5	0.5	0.0)
O2	(0.0	0.5	0.5)
O3	(0.5	0.0	0.5)
Ba	(0.0	0.0	0.0)
Ti	(0.5	0.5	0.5)
Tetragonal phase			
O1	(0.5	0.5	0.0+Δ_{O1})
O2	(0.0	0.5	0.5+Δ_{O2})
O3	(0.5	0.0	0.5+Δ_{O2})
Ba	(0.0	0.0	0.0)
Ti	(0.5	0.5	0.5+Δ_{Ti})
Orthorhombic phase			
O1	(0.5	0.5+Δ_{O1}	0.0+Δ_{O2})
O2	(0.0	0.5+Δ_{O3}	0.5+Δ_{O3})
O3	(0.5	0.0+Δ_{O2}	0.5+Δ_{O2})
Ba	(0.0	0.0	0.0)
Ti	(0.5	0.5+Δ_{Ti}	0.5+Δ_{Ti})
Rhombohedral phase			
O1	(0.5+Δ_{O1}	0.5+Δ_{O1}	0.0+Δ_{O2})
O2	(0.0+Δ_{O2}	0.5+Δ_{O1}	0.5+Δ_{O1})
O3	(0.5+Δ_{O1}	0.0+Δ_{O2}	0.5+Δ_{O1})
Ba	(0.0	0.0	0.0)
Ti	(0.5+Δ_{Ti}	0.5+Δ_{Ti}	0.5+Δ_{Ti})

out by Ghosez (LDA [94]) and to experimental values (Expt.). The DFT calculations carried out by Ghosez use the LDA functional, which is known to underestimate cell parameters. As ferroelectric instability in $BaTiO_3$ is sensitive to volume underestimation, only structural optimization was performed by Ghosez, while cell parameters were fixed to the experimental lattice constant.

In the cubic phase, the PBEsol cell parameter is slightly underestimating the experimental lattice constant 4.003 Å extrapolated to zero Kelvin [95]. The tetragonal c/a ratio is overestimated by around 1.5% with respect to the experimental values. The displacements of the oxygen and titanium ions from the ideal perovskite structure are close to those of the LDA calculation, but take larger values compared to experimental values. This overestimation can on the one hand be related to the overestimation of the c cell parameter, which favours larger shifts of the Ti and

O along this axis. On the other hand, the Ti displacement shows a wide spread in the experimentally determined values. In the orthorhombic and rhombohedral phases, the cell parameters are close to experiment, although slightly overestimating them. The atom displacements are also in good agreement except for the Ti in orthorhombic phase, where its value is 1.8 times larger then the experimental one. The globally observed overestimation of structural properties suggests that the PBEsol functional may enhance repulsion between ions. In conclusion, our results concerning PBEsol derived structural properties are in good agreement with literature values.

Table 3.3: Cell parameters, angles and atom displacement in the four phases of BaTiO$_3$

Cubic phase	PBEsol (this work)	LDA[94]	Expt.[96]	Expt. [95] 0 K
a[Å]	3.985	3.943	4.012	4.003
V[Å^3]	63.290			
Tetragonal phase			[95] at 320 K	Expt.[97]
a[Å]	3.968	3.994	3.994	3.986
c/a	1.0261	1.011	1.011	1.010
Δ_{Ti}	0.0168	0.0143	0.0215	0.015
Δ_{O1}	-0.0316	-0.0307	-0.0233	-0.023
Δ_{O2}	-0.0187	-0.0187	-0.0100	-0.014
V[Å^3]	64.115			
Orthorhombic phase			[95] at 230 K	
a[Å]	3.961	3.984	3.984	
b[Å]	5.683	5.674	5.674	
c[Å]	5.696	5.692	5.692	
Δ_{Ti}	0.0141	0.013	0.0079	
Δ_{O1}	-0.0236	-0.023	-0.0233	
Δ_{O2}	-0.0156	-0.016	-0.0146	
Δ_{O3}	-0.0129	-0.014	-0.0145	
V[Å^3]	64.306			
Rhombohedral phase			Expt. [98]	Expt.[95] at 15 K
a[Å]	4.007	4.001	4.001	4.003
α [$\circ$]	89.85	89.87	89.87	89.84
Δ_{Ti}	-0.0122	-0.011	-0.013	-0.013
Δ_{O1}	0.0117	0.013	0.011	0.011
Δ_{O2}	0.0192	0.019	0.018	0.019
V[Å^3]	64.346			

Stabilization energies

The comparison of the energy of the optimized structures gives the relative stability between the phases at zero Kelvin. The cubic structure is taken as reference and the energy differences are reported in table 3.4. The energetics of the phases point out that the most stable structure corresponds to the lowest symmetry structure, the rhombohedral phase, followed by the orthorhombic structure and then the tetragonal structure. This result is consistent with experimental and theoretical expectations.

Our PBEsol calculations are compared to the PBEsol calculations of Vielma and Schneider [49] and to hybrid PBE0 [4] calculations from Evarestov *et al.* [99]. Our PBEsol energy differences are larger than those of Vielma and Schneider. The reason lies probably in the stronger break condition in the geometry optimization. Vielma and Schneider stopped relaxation, when the maximum force acting on the ions was less then 0.01 eV/Å . Here a break condition equals to 0.001 eV/Å was used and thus the results might be more precise. The hybrid PBE0 energy differences for the tetragonal phase is 13.84 meV/$BaTiO_3$ larger than our PBEsol value. Furthermore, the relative stabilization energy between phases are greater with the hybrid PBE0 functional.

Table 3.4: Energy differences of the ferroelectric phases of $BaTiO_3$ with respect to cubic phase in meV/$BaTiO_3$

Phase	PBEsol	PBEsol[49]	PBE0[99]
tetragonal	-19.9	-18.8	-33.7
orthorhombic	-25.0	-24.0	-42.5
rhombohedral	-26.7	-25.3	-44.1

Ferroelectric phonon mode

In the framework of displacive phase transition, the soft mode concept created by Cochran relates the ferroelectric instability to the lattice dynamics [100]. This concept supposes that, while approaching the transition temperature in cubic phase, there exists a special phonon mode, whose frequency ’softens’, i.e. converges to zero. The related vibration ’freezes’ and the frozen atomic displacements produces a crystal of another symmetry. As ferroelectricity is related to spontaneous appearance of polarization, a change in the optical phonon is expected, where the atoms displacements are out of phase. In fact, theoretical calculations and experimental measurements confirmed the existence of a Γ_{15} soft mode in $BaTiO_3$ [33]. [1]

For the calculation of the phonon modes, the energy E is expanded about the cubic structure up to the harmonic term:

$$E = E^{cubic} + \frac{1}{2} \sum_{\tau,\tau',\alpha,\beta} D^{\tau,\tau'}_{\alpha,\beta} \nu^{\tau}_{\alpha} \nu^{\tau'}_{\beta} \tag{3.4}$$

with E^{cubic} the energy of the perovskite structure, τ and τ' atom labels and where

$$D^{\tau,\tau'}_{\alpha,\beta} = \frac{\partial^2 E}{\partial \nu^{\tau}_{\alpha} \partial \nu^{\tau'}_{\beta}} \tag{3.5}$$

is the second derivative matrix, which is related to dynamical matrix at the Gamma point by factors of ionic mass. In the cubic structure, the displacement in a Cartesian direction α of any of the five sublattices will produce only forces laying on this same axis, i.e. all elements of $D^{\tau,\tau'}_{\alpha,\beta}$ for which $\alpha \neq \beta$ are zero. Hence, the 15x15 second derivative matrix reduces into three independent and identical 5x5 blocks for each Cartesian direction. Therefore, the eigenvalues of the second derivative matrix break into five set of modes, which are threefold degenerated. The normal modes of vibrations are solutions of the eigenvalue problem:

$$\sum_{\beta\tau'} D^{\tau,\tau'}_{\alpha,\beta} \zeta^{\tau'}_{\beta}(j) = \lambda(j) \zeta^{\tau'}_{\beta}(j) \tag{3.6}$$

where $\lambda(j)$ and $\zeta^{\tau'}_{\beta}(j)$ are the eigenvalue and eigenvector, respectively. The index j runs from 1 to 5. Among these normal modes, the soft mode is identified by an negative eigenvalue. This indicates a negative curvature of the energy surface and marks that the perfect perovskite structure is a saddle point of the energy surface.

The soft mode eigenvector was determined using the frozen phonon method [36]. In table 3.5 the calculated soft mode eigenvector are reported and compared to theoretical and experimental values.

Soft mode eigenvector components are in good agreement with experiment and the LDA calculation.

In conclusion, the previous calculations demonstrate that the PBEsol DFT calculations describe accurately the zero Kelvin properties of $BaTiO_3$. Therefore, these

---

[1] Experimental measurements of the soft mode frequency behaviour with temperature show an accordance with theoretical predictions above a hundred degrees above the Curie temperature. However, below this temperature deviation appears suggesting mixing of order-disorder behaviour.

Table 3.5: The Γ_{15} soft phonon mode eigenvector of cubic phase of $BaTiO_3$ at optimized lattice constant, i.e. for the PBEsol calculation a = 3.985 Å and for LDA a=3.946 Å . The eigenvectors are normalized to unity

Γ_{15}		Ba	Ti	O1	O2	O3
TO1	PBEsol	0.15	0.77	-0.19	-0.19	-0.55
	LDA[36]	0.20	0.76	-0.21	-0.21	-0.53
	Expt.[98]	0.22	0.76	-0.23	-0.23	-0.52

calculations can be used for DFT based modelling. In the following section, a further step towards DFT based modelling will be presented by introducing the concept of polarizable ions with nominal charges.

3.1.2 Use of nominal charges

$BaTiO_3$ is an insulator possessing a large band gap. On these grounds, it is attemptable to describe the atoms as close shelled, i.e. the electrons are bounded to their respective nucleus [101]. In fact, Kohn-Sham electronic band structure calculations showed that in cubic phase, $BaTiO_3$ can nearly be considered as ionic, which sets of bands are globally composed of well separated. However, there is some admixture of Ti 3d character to the O 2p bands. In ferroelectric phases the mixing between O 2p and Ti d bands is enhanced. The mixture between Ti 3d and O 2p is often referred as O 2p-Ti 3d hybridization. [94]. In the classical Shell Model, presented in section 1.3, the hybridization between ions are related on the one hand to a static charge transfer and on the other hand to induced dipole moments. Thereby, the ionic charges appear as free parameters of the model. Once the static ionic charge is determined, these are kept fixed in all phases and thus cannot describe change in charge due to eventual charge transfer between ions going from the cubic to the ferroelectric phases. The question is now whether it is necessary to introduce parameters for static charges or if nominal charged ions, which would be expected in a purely ionic picture of the crystal (+2 for Ba, +4 for Ti, -2 for O), represent a good approximation. In other terms, the question can be reformulated: is it possible to imitate the effect of hybridization only through polarization of dipolar order of nominal charged ions? To answer this question, at least partially, the concept of polarizable nominal charged ions is introduced into the DFT calculation. Within this concept of nominal charged ions, key quantities such as stabilization energy, Born effective charge and polarization are calculated and compared to complete electronic structure DFT calculations.

Stabilization energy

The final aim of this work is to apply the PIM to ferroelectric $BaTiO_3$. In the PIM the ions are treated as closed shelled ions with nominal charges. Furthermore, polarizability of the ions up to dipolar order of the electron cloud is taken into account.

In the following study, the coulomb part of the relative stabilization energy between phases are determined using the PIM interaction potential but with dipole moments extracted from DFT. The extraction of dipole moments is carried out using a Wannier function analysis from the Kohn-Sham (KS) wave functions. To recall, the *ab initio* calculations are performed in the plane wave formalism, where each KS wavefunction is non-localized and periodic in space. In order to calculate dipoles associated to each ion, localized orbitals around the ions are needed. Therefore, a Wannier function transformation of the KS wavefunctions is realized [102]. The Maximally Localized generalized Wannier Function (MLWF) are determined by unitary transformation of KS wave functions [79]:

$$w_n(\mathbf{r}) = \sum_{m=1}^{J} U_{nm} \left|\phi_m\right\rangle \tag{3.7}$$

where the sum runs over all J KS wave functions $|\phi_m\rangle$ and where U_{nm} is the unitary transformation. The unitary transformation U_{nm} is determined so that the condition of maximally localized generalized Wannier function is verified. This condition is approved, when the spread of the Wannier functions Ω is minimized:

$$\Omega = \sum_{n=1}^{J} (\langle r^2 \rangle_n - \langle \mathbf{r} \rangle_n^2). \tag{3.8}$$

Then the dipole moment component of an ion I along the α Cartesian axis is calculated from the Wannier center positions r_n. Each Wannier center is occupied by two electrons and the expression of the dipole moment component is given by:

$$\mu_\alpha^I = -2 \sum_{n=1}^{J} r_n^\alpha. \tag{3.9}$$

Once the dipole moments are extracted from DFT, they are employed for the determination of the different contributions to the relative stabilization energies, if one considers the ions to be classical and interacting via the PIM interaction potential. The coulomb part of this interaction model is calculated using the Ewald summation formula explicated in section 2.1.5. To remind, the precision of the calculation of Coulomb interaction with the Ewald summation formula depend on the value of the smearing parameter κ. Therefore, the convergence of the charge-charge energy in a 3x3x3 and 7x7x7 supercell is first tested by varying κ from its default value in the program 5.6 to 13.4.[2] The cut-off distance of the real space sum is chosen within the minimum image convention. The results of the charge-charge interaction energy as a function of κ is plotted in figure 3.1.

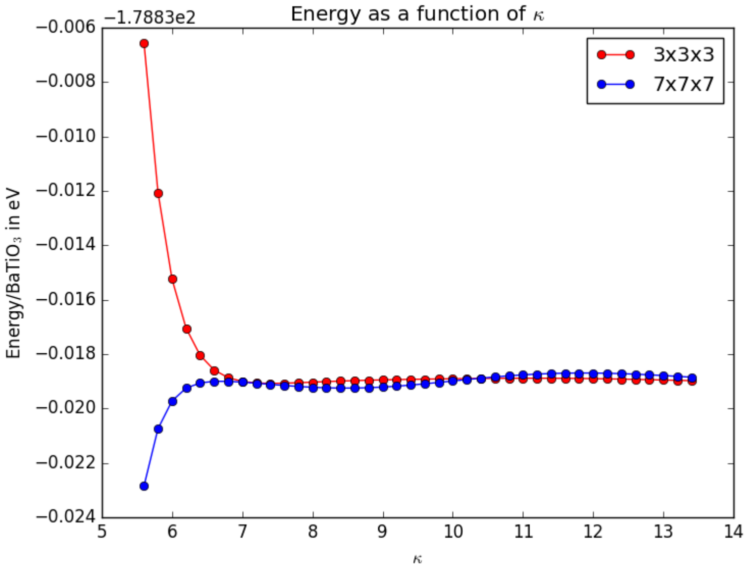

Figure 3.1: Convergence of the charge-charge interaction term as a function of eta in a 3x3x3 and 7x7x7 supercell.

Several remarks can be done. First, as expected the larger simulation cell present a faster convergence. For both simulation cell sizes, convergence of the Ewald summation is achieved for κ equals 6.8. A zoom on higher κ values shows that the energy oscillates around an mean energy value of -178.849 eV/BaTiO$_3$ with an maximum amplitude of 0.0003. Even if one would prefer higher precision in energy, such an numerical error bar is acceptable, as the theoretical energy difference between phases are in the order of meV/BaTiO$_3$. Second, the energies at the default κ value of 5.6 give rise to an energy difference between the 3x3x3 and 7x7x7 supercells of 0.016 eV/BaTiO$_3$. To conclude, in energetically very sensitive materials, such as BaTiO$_3$, passing from a 3x3x3 to a 7x7x7 supercell changes the energetics when κ parameter is not well chosen and may even lead to a wrong sequence of phase transition. Therefore, throughout the work a κ value of 7 is taken, even if this makes calculations slower compared to calculations with default κ value.

---

[2] If the charge-charge term converges, it can be assumed that dipole interactions are converged as well, as it decreases faster.

For the geometry optimized structured determined in section 3.1.1, the different electrostatic energy contributions the PIM given by equations 2.20 and 2.18 are calculated. Thus, the total electrostatic energy is given by:

$$U_{Elec} = \underbrace{\sum_{i<j} q_i \mathbf{T}_{ij} q_j}_{Charge-Charge} + \underbrace{\sum_{i,j} \left(q_i \mu_j^{\alpha} - q_j \mu_i^{\alpha}\right) \mathbf{T}_{ij}^{\alpha}}_{Charge-Dipole} - \underbrace{\sum_{i,j} \mu_i^{\alpha} \mu_j^{\beta} \mathbf{T}_{ij}^{\alpha\beta}}_{Dipole-Dipole} .$$

Note, that in the previous expression the damping term is omitted, as short range effects are inherent to the DFT extracted dipole moments.

Table 3.6: Electrostatic energy contributions in the four phases of $BaTiO_3$ in meV/$BaTiO_3$

Phase	Charge-Charge	Charge-dipole	Dipole-dipole	Total
cubic	-178.894			-178.894
tetragonal	-178.849	-1.743	-0.063	-180.655
orthorhombic	-178.812	-2.224	-0.081	-181.117
rhombohedral	-178.804	-2.366	-0.093	-181.263

In table 3.6 the results are listed. The total electrostatic energy follows the phase transition sequence. Looking at the different contributions to the total electrostatic energy, it can be noticed that the charge-charge contribution destabilizes the ferroelectric phases. In a rigid ionic model in the cubic phase, a displacement of the titanium ion towards the oxygen ion suggested by the soft mode displacement pattern would not appear, as short range repulsion would necessarily increase. The inclusion of dipole moments is thus mandatory. In fact, it is the charge-dipole interaction that mainly lowers the energy and, with a smaller contribution, the dipole-dipole interaction. Even if from the electrostatic interaction point of view the inclusion of dipoles favours ferroelectric phases, the appearance of the correct phase transition sequence depends further on the cost term in the polarization energy and the short range repulsion. The accurate description of the latter is a very challenging task in the development of a PIM for $BaTiO_3$.

Born effective charge

The Born effective charge appears in perovskite ferroelectrics as a key concept to relate electronic and structural properties. The Born effective charges are useful to analyse spontaneous polarization results and are central to the LO-TO optical phonon splitting in polar crystals. The Born effective charge of atom κ for periodic solids is defined as the change in polarization per unit cell volume Ω caused by its displacement in direction α under zero external field $E = 0$. The tensor components of the Born effective charge are given by:

$$Z^*_{\kappa,\alpha\beta} = \Omega \frac{\delta P_\beta}{\delta \tau_{\kappa,\alpha}}\Big|_{E=0}. \tag{3.10}$$

The Born effective charge can be decomposed in two contributions. First, a static charge term caused by the displacement of the ions. Second, a dynamical contribution due to a change in electronic distribution.

$$Z^*_{\kappa,\alpha\beta} = Z_\kappa + \Omega \frac{\delta P^{el}_\beta}{\delta \tau_{\kappa,\alpha}}\Big|_{E=0} \tag{3.11}$$

where Z_κ is the static charge of atom κ and P^{el} the electronic contribution to the polarization. King-Smith and Vanderbilt derived an expression for the change in electronic polarization in terms of the valence band wave functions between an initial and a final state. Therefore, the valence band wave functions are given in terms of Wannier functions $W_n^\lambda(r)$. Thereby, the electronic polarization in a state λ takes the following expression [103]:

$$\mathbf{P}^\lambda = (f\ q_e/\Omega) \sum_{n=1}^{M} \int |W_n^\lambda(r)|^2 dr \tag{3.12}$$

where f is the occupation number of states in the valence band (in spin generated systems $f = 2$). q_e is the electron charge and M the number of occupied bands. Thus, the change in polarization between an initial and a final state is related to the displacement of the center of the Wannier functions. Within this approach, Zhong, King-Smith and Vanderbilt calculated the Born effective charge of $BaTiO_3$ in cubic phase [104].

While King-Smith and Vanderbilt describe the change in polarization by means of change of the barycentre of Wannier functions over the whole calculation cell, here the Born effective charge includes only changes in dipole moments, i.e. no higher multipoles are considered and no charge transfer between ions is allowed. Thus, ions are treated as nominal charged and close shelled polarizables at dipolar order. This presumes that for any state λ the Wannier centres are first attributed to each ionic species and then the dipole moment is calculated using the method described in the previous section. The Born effective charge in the closed shell polarizable ion picture becomes:

$$Z^*_{\kappa,\alpha\beta} = Z_\kappa + \sum_i \frac{\delta \mu_i^\beta}{\delta \tau_{\kappa,\alpha}}\Big|_{E=0}. \tag{3.13}$$

In the cubic structure of $BaTiO_3$, the barium and the titanium have isotropic charge tensors. The oxygen atoms are located at the face centres. Thus, there exists two inequivalent directions for the oxygen atoms, one parallel and one perpendicular to the Ti-O bond. The associated effective charge components are labelled $Z^*_{O\|}$ and $Z^*_{O,\perp}$, respectively.

The Born effective charge calculated by equation 3.13 with the dipole moments μ extracted from PBEsol calculations. In table 3.7 the Born effective charges are reported and compared to the King-Smith and Vanderbilt DFT calculations (LDA), experimental (Expt.) and Shell Model (SM) values.

Table 3.7: Born effective charges of $BaTiO_3$ in cubic structure
$a = 4.00$ Å in units of the elementary charge

	Z^*_{Ba}	Z^*_{Ti}	$Z^*_{O,\perp}$	$Z^*_{O,\|}$
Nominal	+2	+4	-2	-2
Expt. [105]	+2.9	+6.7	-2.4	-4.8
LDA [104]	+2.75	+7.16	-2.11	-5.56
this work	+2.71	+6.52	-2.11	-5.47
SM [46]	+1.93	+6.45	-2.3	-3.79

The approximated Born effective charges in the close shell ionic picture (table 3.7 'this work') are comparable with experimental and King-Smith and Vanderbilt results. Interesting to note is that the here derived Born effective charges are slightly better than the Shell Model values. This result points out that static charge transfer as presumed in the Shell Model is not necessary for the description of Born effective charges. To conclude, the main contribution to the change in electronic structure by displacement of an ion from its ideal cubic positions can be described in good approximation with nominal charged polarizable ions.

Polarization density of a unit cell

In this section, the polarization densities of the geometry optimized structure are calculated. The ionic part of the contribution to the polarization density is defined as the difference of the positive and negative barycentre of charges. On figure 3.2 a schematic representation of $BaTiO_3$ unit cell is given [106].

The origin of the unit cell lies in one of the barium atoms. The shape of the unit cell is delimited by the lines linking the eight barium ions at the corners. Each barium atom accounts to the unit cell polarization density with a weigh of $\omega = 1/8$ and the oxygen ions on the faces of the unit cell with a weight of $1/2$. The titanium

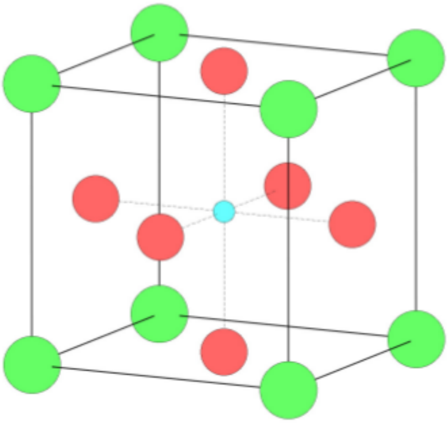

Figure 3.2: Unit cell of $BaTiO_3$; at the corner the barium ions in green, in the centrer the titanium in blue and on the faces the oxygen ions in red.

ion lies completely in the unit cell and has thus a weight of one. Hence, the ionic contribution to the polarization density per unit cell is given by:

$$\mathbf{P}_{ion} = \frac{1}{\Omega} \sum_{i=1} \omega_i (q_i \mathbf{r}) \tag{3.14}$$

where i runs over the fifteen atoms of the unit cell represented in the figure above and that contribute with a weight ω_i to the polarization density. The electronic contribution is formulated in terms of dipole moments and the total expression of the polarization density becomes:

$$\mathbf{P} = \frac{1}{\Omega} \sum_{i=1} \omega_i (q_i \mathbf{r}_i + \mathbf{d}_i). \tag{3.15}$$

In table 3.8, the calculated polarization densities are listed and compared to DFT calculations, Shell Model polarizations and experimental values. The sequence of the spontaneous polarization is the same for the LDA, Shell Model (SM) and the in 'this work' derived values. That is to say, the polarization density is decreasing from the rhombohedral to the cubic phase. It can be noticed that the in 'this work' calculated polarization presents a similar order of magnitude as the polarization taking the full electronic structure into account (LDA). While, the SM polarization density calculated from Molecular Dynamics simulations at finite temperature are lower by approximately 30%. The experimentally derived polarizations do not follow the previously mentioned order. For a deeper discussion, one should look at the experimental measurement techniques (and related error bars) and experimental conditions (temperature etc.), at which the measurement were carried out, but this is beyond the scope of this thesis. The concern of this section was again the verification, if nominal charges and dipoles are sufficient to capture ferroelectricity. As the Born effective charges were well described within this approximation, at least as well as other models, it is not surprising that comparable polarization densities are obtained compared to full electronic structure calculations.

Table 3.8: Polarization density in the three geometry optimized ferroelectric structures of $BaTiO_3$ in C/m^2

Phase	this work	LDA[107]	SM[46]	Expt.
tetragonal	0.29	0.29	0.17	0.27^a 0.26^b 0.23^c
orthorhombic	0.31	0.33	0.20	0.36^d
rhombohedral	0.32	0.35	0.23	$0.34^{e,f}$
a:[108] b:[109]	c:[110] d:[111]	e:[112] f:[98]		

3.2 Fitting procedure

In this section, first, the general procedure, which was successfully applied to alkaline earth oxides (see. section 2.2), is used for a first attempt of parametrization of a PIM for $BaTiO_3$. In the second section an analytical fitting procedure is introduced including the fit on energy differences. In the last part of this chapter, a DIPPIM and a DAIM are derived for $BaTiO_3$.

3.2.1 General fitting procedure

In this section the parametrization of a PIM for $BaTiO_3$ following the general procedure described in section 2.2 is applied. Three configurations at different local environments corresponding to different thermodynamic phases, i.e. cubic, tetragonal and rhombohedral phase, are used. Each of these configurations include 625 atoms. The atoms were displaced from their literature positions using short *ab initio* MD calculations at high temperature. The *ab initio* calculations were carried out with VASP using the Projector Augmented-Wave method (PAW) and the HSE06 for the exchange correlation functional [2].[3] The Brillouin Zone integration was performed using a 1x1x1 Monkhorst-Pack (MP) k-point mesh within the automatic mesh generation. The plane-wave cutoff was set to 500 eV. The break condition was set to 10^{-6}. The parameters of the short range repulsion and polarization term were fitted on the DFT stresses and forces using the global fitting procedure described in sec. 2.2.1.

The developed potential was tested at 0 K for the energy surface along the ferrolectric mode displacements, see figure 3.3. The figure shows that the model is not able to reproduce the ferroelectric phonon instabilities and therefore the extrema at the ideal cubic positions is the global minimum of the energy surface.

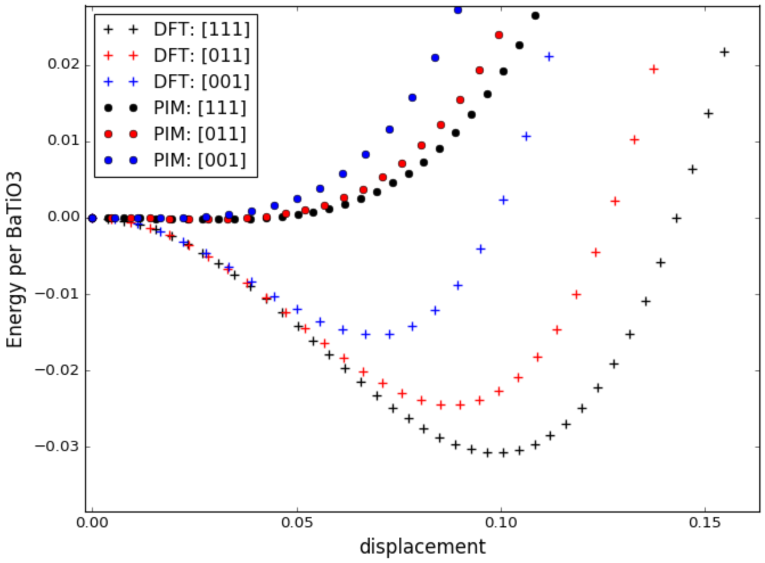

Figure 3.3: Total energy in eV as a function of the ferrolelectric mode displacements in cubic phase with cell parameter $a = 4.00$ Å along [001], [011] and [111] directions.

Molecular Dynamics calculations using the PIM have been carried out at atmospheric pressure in the NPT ensemble. A bottom up approach was used starting from the rhombohedral structure of a 5x5x5 supercell from 50 K to 250 K. As expected from the 0 K energy surface along the ferroelectric modes displacement, the MD calculations lead to a cubic structure with zero average polarization. Over the

---

[3] The DFT calculations were carried out with the HSE06 exchange correlation functional, because it presents good structural and electronic properties for $BaTiO_3$ (see discussion 1.1.6). However, the computational cost of the HSE06 exchange correlation functional is high. At the initial stage of the thesis great computational resources were available. Later on, we decided to change to the PBEsol exchange correlation functional, as it presents satisfying properties and is computationally less expensive.

temperature range no phase transition can be observed and the only effect of temperature is given by the expansion of the lattice parameters with increasing temperature, see figure 3.4.

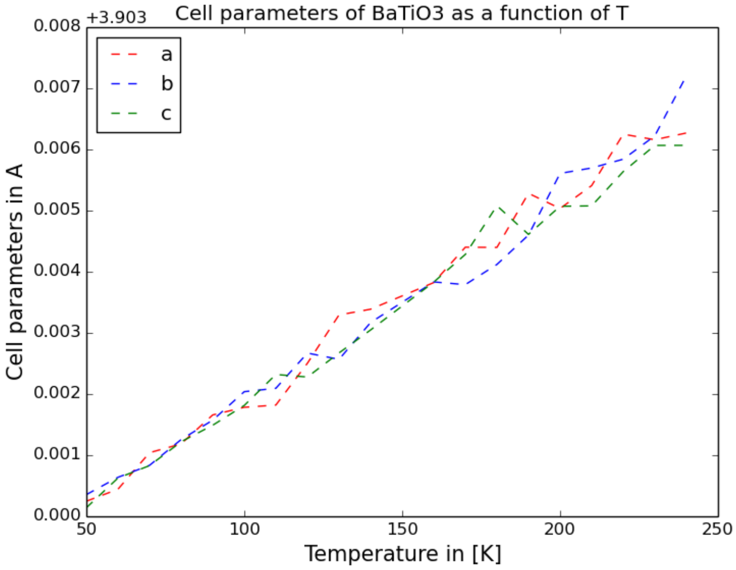

Figure 3.4: Cell parameters in Å as a function of temperature.

This first attempt of derivation of a reliable PIM for ferroelectric $BaTiO_3$ shows the challenge this task constitutes. Indeed, in $BaTiO_3$ the structural changes are related to channelling small energy differences in the order of some meV (see table 3.4). The total objective function after minimization takes a value of χ^2 =0.126. Even if for some oxides materials the order of magnitude of the χ^2-value is reasonable, such as metal oxides [113], it might be not precise enough to capture the delicate small energy differences in $BaTiO_3$. Furthermore, the failure of the parametrization with the general fitting procedure may be due to the choice of an inappropriate reference configuration, in which the ions are too strongly displaced from their equilibrium positions. Therefore, the force acting on the ions may point out in directions favouring the cubic phase instead of pointing towards the ferroelectric equilibrium positions. In addition, in the global fitting procedure, where parameters are derived in one minimization process, the occurrence compensation errors is common. Therefore, the separate identification of the origin of the errors on the parameters is difficult to achieve.

3.2.2 Modified fitting procedure

Inclusion in the fit of the energy difference

It has been pointed out that the correct description of the energy surface at 0 K leads to a right order of phase transition at finite temperature (cf. discussion about DFT-based models in chapter 1). The fit on energy difference is included to assure the accurate description of the potential surface. The total objective functions is extended with the following energy contribution:

$$A_E\left(\{\chi\}\right) = \frac{\sum_A \left|\left(E^{A,PIM}\left(\{\chi\}\right) - E_r^{PIM}\left(\{\chi\}\right)\right) - \left(E^{A,DFT} - E_r^{DFT}\right)\right|^2}{\sum_A \left|E^{A,DFT} - E_r^{DFT}\right|^2} \tag{3.16}$$

where A runs over the number of configurations and the index r labels the reference energy.

Beside the fact that the inclusion of the fit on energy differences should ensure the correct description of the energy surface, it also allows to propose a new procedure for developing PIMs. This new procedure can be divided into two steps. First, the parameters appearing in the short range repulsive part are derived from the short range forces. The short range forces are obtained by subtracting the electrostatic forces from the total DFT forces. The electrostatic forces are the charge-charge, charge-dipole and dipole-dipole forces. The dipole moments extracted from DFT calculations are used for the interaction including dipole moments. The determination of the short range parameters can be realized either with an analytical fit (cf. next section) or with the non-gradient simplex method (cf. section 2.1.5). In the second step, the damping parameters and polarizabilities are fitted on the DFT extracted dipoles and on the energy difference, while the short range parameters derived in the first part of the fitting procedure are kept constant. Due to the fact that short range parameters and nominal ionic charges are fixed, the residue energy difference is related to the dipole interaction terms. Therefore, in contrast to the common separated fitting procedure (cf. section 2.2.2), the inclusion of the fit on energy differences reduces possible compensation errors caused by wrong separation between asymptotic and short range induced dipoles (cf. section 2.1.4).

Short range parameters and the analytical fit

In this section the method of the derivation of short range parameters using the analytical fitting procedure is presented. Even if in the case of $BaTiO_3$ the analytical fitting procedure is only partially successful, the procedure is detailed in the following because this fitting procedure could find application in less complex ionic materials. Special configurations are required for the analytical fit, in which the contributions to the short range forces are known. Three successive analytical fits are necessary to determine the short range parameters of $BaTiO_3$ in a decoupled way. One analytical fit for the Ti-O parameters and another analytical fit for the Ba-O parameters are carried out on the short range forces acting on titanium and barium ions, respectively. The forces acting on the oxygen ions are a function of the Ti-O, Ba-O and O-O parameters. Therefore, the O-O parameters are fitted on the short range forces acting on the oxygen, once the Ti-O and Ba-O short range parameters are known.

Ti-O interaction

The short range parameter are separately fitted on different sets of configurations. The set of configurations of the ferroelectric soft mode in [001] direction for different amplitudes of displacement are used in a unit cell of cell parameter equal to 3.985 Å and 4.02 Å for the short range interaction parameters between titanium and oxygen. In these configurations, only the z-components of the forces are non zero due to symmetry. The titanium ion is placed in the oxygen cage. Therefore, the total short range force F^{SR}_{Ti-O} is given by the four oxygen ions perpendicular to the Ti-O bond $O_\perp$ plus the two oxygen ions parallel to the Ti-O bond. The oxygen with the shorter bond is labelled $O_{\parallel,1}$ and the other involved in the longer bond $O_{\parallel,2}$. The total short range force acting on the titanium is given by:

$$F^{SR}_{Ti} = F^{SR}_{Ti,O_{\parallel,1}} + F^{SR}_{Ti,O_{\parallel,2}} + 4\, F^{SR}_{Ti,O_\perp}. \tag{3.17}$$

Taking the Born-Mayer potential into account 2.9, the force components of the Cartesian coordinates α take the following expression:

$$F^{\alpha}_{i,j} = a^{ij} \frac{\mathbf{r}^{\alpha}_{ij}}{r_{ij}} A^{ij} e^{-a^{ij} r_{ij}}. \tag{3.18}$$

The fit on the short range force given in eq. 3.17 is performed using the Trust Region Reflective least-squares algorithm with bounds on the variables as implemented in the SciPy library of Python [114]. The fit results in a parameter for the steepness of the repulsion wall of $a^{ij} = 1.100$ and the strength parameter $A^{ij} = 55.400$ with a standard deviation error of 0.032 and 2.23, respectively. In figure 3.5 the result of the fit is shown.

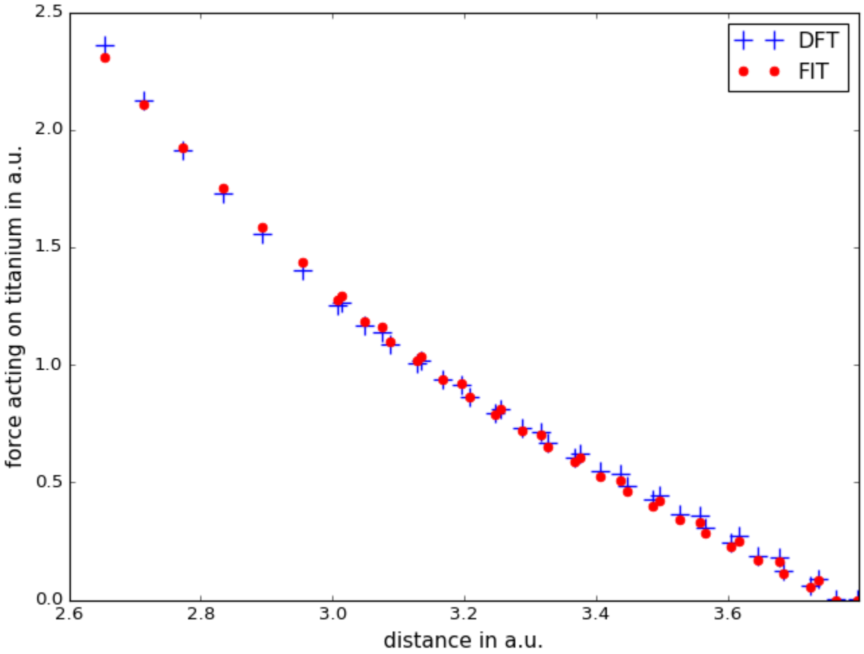

Figure 3.5: Short range force acting on titanium due to the nearest oxygen ions plotted versus the Ti-O distance in the shortest bond.

Ba-O interaction

In $BaTiO_3$ the barium ion is surrounded by 12 oxygen ions. In this subsection, a set of short range parameters of the Ba-O interaction is determined with an analytical fit. Therefore 20 configurations were created, including a wide range of Ba-O distances. The analytical fit leads to a parameter for the steepness of the repulsion wall of $a^{ij} = 1.77$ and the strength parameter $A^{ij} = 133.38$ with a standard deviation error of 0.008 and 4.00, respectively. The result of the fit is shown in figure 3.6.

O-O interaction

The force acting on the oxygen ion results from interactions with the three ion species. The repulsion parameters between oxygen ions are determined through a fit on forces, while the Ti-O and Ba-O parameters derived in the previous sections are kept constant. The ferroelectric soft mode displacement in [001]-direction for different amplitudes are used again as reference configurations. The fit is proceeded by minimizing the objective function given by the expression 2.27. After minimization a χ^2-value equals 156.62 is reached. This enormous χ^2-value reflects

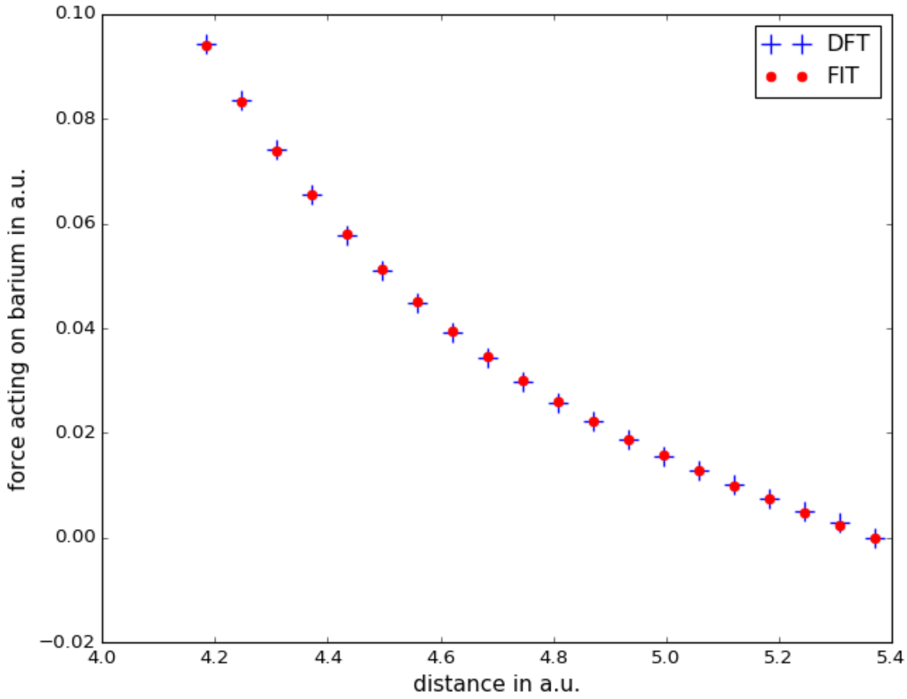

Figure 3.6: Born Mayer short range force acting on barium due to the nearest oxygen ions plotted versus the shortest Ba-O distance.

the impossibility of finding reliable parameters for the O-O short range interaction within this approach. The origin of this large χ^2-value can be explained in the following. As an example, a configuration with soft mode displacements in [001]-direction is considered. The total DFT force acting on the oxygen ion, which is involved in the Ti-O chain, can be decomposed in its different contributions. The contribution due to short range interactions with the two neighbouring Ti, is 1.700 a.u. and the total electrostatic force -1.013 a.u..The contribution due to interactions with barium is negligible small (-0.005). Adding up both contributions, a total force of 0.687 a.u. arises, which is far too high compared to the total force determined with DFT, 0.127 a.u.. The inclusion of the O-O repulsion term would even enlarge the excess in short range repulsion. Thus, it is the large excess in short range repulsion that leads to a large χ^2-value.

Furthermore, it has to be kept in mind that in the PIM the ions are treated as polarizable point charges without spatial extension. As a consequence of this approximation short-range repulsion takes place at inter-ionic distances. However, from a physical point of view, the short range repulsion occurs between electrons due to the Pauli exclusion principle. In order to estimate the order of magnitude of the correction to the inter-ionic distance, the induced dipole moments $\mu_i^z = q_i dr^z = -2\sum_{n=1}^{J} r_n$ is divided by the charge of the Wannier centre q_i. This gives the separation dr_i^z between the barycentre of positive and negative charge of the dipole moment centred on ion i. For ion species with low polarizability, as titanium, the distance dr_{Ti}^z is two order of magnitude smaller than the inter-ionic distance. For the highly polarizable oxygen ion, dr_O^z equals 0.47 a.u., which represent a non negligible correction to the inter-ionic distance of 4.52 a.u. (O-Ti$_1$) and 3.00 a.u. (O-Ti$_2$). In fact, by introducing this correction in distances the excess in short range repulsion can be reduced noticeably. In figure 3.7 the short-range force acting on the oxygen ion of the TiO chain is plotted. The results of the fit with short-range repulsion taking place at inter-ionic distances lies above the DFT short-range forces, while the fit with short-range forces arising between the barycentre of electrons gives closer accordance with DFT.

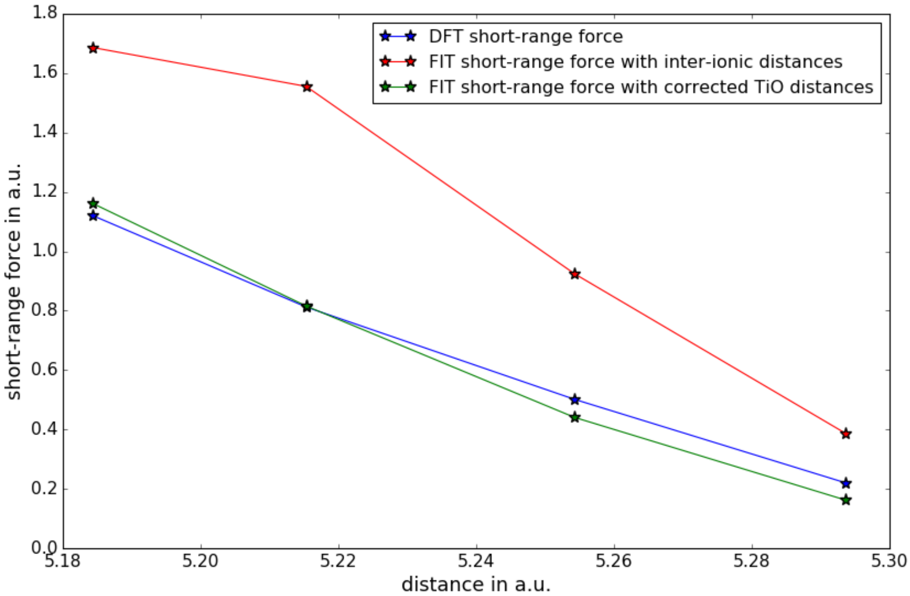

Figure 3.7: Born Mayer short range force acting on the oxygen ion due to the nearest neighbour interaction plotted versus the longest O-O distance.

This example demonstrates, that in the case of BaTiO$_3$ the spatial extension of the dipole moment has an important impact on the precise description of the short-range repulsion term.

As in the PIM asymmetric correction with respect to the nucleus of the short range repulsion due to spatial extension of the dipole moment are not taken into account, in the following compensation errors between polarization and short range term of the potential are allowed in order to achieve the best global description of

$BaTiO_3$. [4] Therefore, the Global fitting procedure explained in sec. 2.2.1 is used, but additional the fit on energy differences is included.

3.2.3 Polarization part

In the following, the polarization term is discussed. Three different fits were performed. First, a fit only on the dipole moments. Second, a fit on dipole moments and energy differences and third, a fit on dipole moments and energy differences allowing compensation errors between short range and polarization term. The set of configurations includes 6 different amplitudes of soft mode displacement along the three directions and 6 additional different displacement amplitudes along the [001]-direction at different volume. Furthermore, 3 configurations at the geometry optimized structures are used. In addition 11 configurations, which have been previously employed in the analytical fit for the BaO and OO short range parameters, are included in the set of reference configurations.

The first fit is independent on the short range term and the determination of the polarization part is carried out by minimizing the objective function given by 2.29. The χ^2-value after the minimization process equals 0.05. Such a small χ^2-value means that the error in PIM dipole moments is small compared to the DFT dipoles. Hence, the use of constant polarizability, i.e. linear relation between induced dipole and local field, can be considered as reasonable, at least in the range of reference configurations.

The second fit is carried out on dipoles moments and energy differences and therefore dependent on the short range term. The resulting the χ^2-value is not satisfying and equals 0.77. This may be due to the large excess in short range repulsion of the forces acting on the oxygen ion, as discussed in the previous section 3.2.2.

In the third fit, the short range parameters for the BaO-interaction are kept fixed to the analytical determined parameters in sec. 3.2.2. Furthermore, the polarizabilities of barium and oxygen and the OBa damping parameters are kept fixed to the values determined by the first fit using the dipole objective function. Thus, only the short range parameters between OTi and OO and Ti polarizabilities and OTi damping parameters are free parameters in this fit. The additional freedom in these parameters allows compensation errors between the short-range and the polarization term in the TiO interactions. As starting guess of the parameters for the short range term, the in section 3.2.2 analytically determined parameters are taken and

---

[4] The PIM program offers the possibility to introduce spatial deformability of the electron cloud, see section 2.1.3. However, in this correction the deformed electron cloud is centred on the ion.

for the polarization parameters the first fit parameters are used. The fit is carried out on forces, stresses, dipole moments and energy differences with a weight factor of s_2=0.5 between forces and stresses and s_3=0.1 for energy differences. The form of the total objective function is given by:

$$\chi^2 = \left[\frac{1}{2}\left(A_D + \frac{A_F + s_2 A_S}{1+s_2}\right) + s_3 A_E\right]\frac{1}{(1+s_3)}. \tag{3.19}$$

After minimization a total χ^2-value of 0.120 is reached. The force contribution to the total χ^2-value is 0.127 and the contribution of stresses, dipole moments and energy differences are 0.114, 0.134 and 0.038, respectively. In the following, this interaction potential will be referred as the DIPPIM and the parameters are given in table 3.9. In the next chapter 4, the zero temperature properties of this DIPPIM will be presented.

Table 3.9: Parameters of the DIPPIM in atomic units

	O-O	O-Ba	O-Ti
B^{ij}	10.01	133.4	74.9
a^{ij}	2.930	1.770	1.665
b_D^{ij}	1.586	2.018	2.054
c_D^{ij}	1.043	0.892	1.615
c_D^{ji}		-.489	-.304

	O	Ba	Ti
α	11.10	7.98	2.02

3.2.4 DAIM

In the previous section, it has been pointed out that, because of the omission of finite size effects, compensation is allowed in order to reach the best global fit. In the prospect to get a potential that fit as close as possible to the reference data, in this work a DAIM potential is developed, which has been presented in subsection 2.1.3. Taking the same set of configuration as in the previous section, it was shown that the objective function could be significantly reduced, especially in stress. Thus, the introduction of deformability up to dipolar order for the oxygen ion helps to reproduces more closely the interactions between ions in $BaTiO_3$. Several different DAIM models have been developed by varying the different input ingredients in the fitting procedure, i.e. weight factors and set of configurations. In this thesis, the most satisfying model among all developed DAIM models is presented and is referred as the DAIMO model in the following. The set of reference configurations includes beside the soft model displacement amplitudes (12 configurations per directions), 3 MD configurations at 50 K, 100 K and 150 K around the minima in the displacement curves. Configurations including random displacements in the three ferroelectric phases (2 per phase), 1 MD configuration at rhombohedral phase and finally 1 configuration obtained during a NPT MD calculation with another DAIM model for which this structure presented instabilities. For this model, the total objective function takes a χ^2-value of 0.110. The force contribution to the objective function is 0.184, the stress contribution and energy difference contribution 0.036 and 0.054, respectively. The parameters of the DAIMO model are given in the table 3.10.

Table 3.10: Parameters of the DAIMO model in atomic units

	O-O	O-Ba	O-Ti
B^{ij}	23.4	357.3	136.2
a^{ij}	1.735	1.868	1.835
b_D^{ij}	2.046	1.726	1.840
c_D^{ij}	1.046	2.968	1.526
c_D^{ji}		-.810	-3.123

	O	Ba	Ti
α	15.89	13.71	0.441
D	1.735		
β	1.195		
η	12.87		
C	0.009		

3.3 Parenthesis about the dipole-dipole damping

In this section a modified interaction potential will be introduced, which is able to avoid dipole-dipole collapse between high polarizable species, the so-called 'Polarization catastrophy'. In fact, Molecular Dynamics calculations performed with a potential involving high polarizabilities for oxygen and barium show the appearance of non physical collapse between the two ions species due to auto-induced dipole moments. Even if in the here presented DAIMO model the collapse does not arise, in the following a tool to avoid auto-induced dipole-dipole collapse is presented, which has been included in the Molecular Dynamics source code during the thesis. In fact, similar effects of dipole-dipole collapse have been observed in other studies of co-workers. Therefore, in the PIM exists the possibility to add an additional Gaussian-like repulsion term, which acts as a steep repulsion wall at short ion distance to avoid unphysical collapse [115] [116]. Here the avoiding of collapse is realized by a damping of the dipole-dipole interaction in a similar way as the damped charge-dipole interaction by means of of Tang-Toennies damping functions $f_n^{ij}(r_{ij})$ given in expression 2.19. Thereby, the distance, at which the damping of the dipoles occurs, are taken to be the same for anions and cations, i.e. $b^{ij} = b^{ji}$, and the strength parameter of the damping is set to 1. The damped dipole-dipole interaction is given by the following expression:

$$U^{\mathrm{dip-dip}} = -\sum_{i,j} \mu_i^{\alpha} \mu_j^{\beta} f_4^{ij}(r_{ij} \mathbf{T}_{ij}^{\alpha\beta}). \tag{3.20}$$

Although if in the final DAIMO potential, which has been presented in this thesis, the inclusion of dipole-dipole damping is not necessary, the dipole-dipole damping is a useful tool to avoid auto-induced dipole-dipole collapse. In fact in the case of a previously derived old DAIM model with high polarizabilities for barium and oxygen, the obviation of such collapse effects by the damping of the dipole-dipole interaction was found to be efficient.

3.3.1 Conclusion

In the first part of this chapter it has been investigated, whether the use of closed shelled and polarizable ions with nominal charge is appropriate to reproduce key quantities of ferroelectric $BaTiO_3$. It has been shown by comparing the Born effective charges and the polarization densities, that the error introduced by describing the system with nominal charged ions is comparable to other modelling methods, such as the Shell Model, and are in satisfied agreement with DFT. Furthermore, the expression of the PIM interaction potential has been employed to study the electrostatic energy using the DFT extracted dipoles at the geometry optimized structures. The calculation reveals that the main electrostatic contribution to the stabilization of the ferroelectric phases are given by the charge-dipole interaction and with a smaller portion by the dipole-dipole interaction. On the basis of these results, it seems reasonable to attempt modelling of $BaTiO_3$ using nominal charged and polarizable ions. Motivated by the previous results, the second part of this chapter deals with the development of a PIM for ferroelectric $BaTiO_3$. First, the general fitting procedure as described in literature was shown to lead to a potential favouring the paraelectric cubic phase. Therefore, a new fitting procedure has been introduced including the fit of energy differences and separated treatment of short and long-range forces reducing possible compensation errors during parametrization. Application of this fitting procedure brings to light that, for a precise description of the short range repulsive forces, the asymmetric size effects of the electron cloud with respect to the nucleus are necessary. As such effects are not included in the DIPPIM, compensation errors were allowed in the parametrization procedure. Two different types of PIMs have been derived, a DIPPIM and a DAIMO potential. The DAIMO model includes deformation up to dipolar order and reduces the objective function further, especially for the stress tensor.

Chapter 4

Accuracy of the model

Contents

IN the previous chapter a DIPPIM and a DAIMO interaction potential for $BaTiO_3$ have been developed. In the present chapter the quality of both potentials is examined. In the first section the ability to reproduce zero temperature properties is investigated, i.e. the ferroelectric soft mode displacement, bulk modulus and geometry optimization. In the second section, finite temperature properties are evaluated using Molecular Dynamics simulations. The latter give access to the macroscopic properties as a function of temperature which can be compared to experimental findings.

4.1 Zero temperature properties

In this section zero temperature properties of both the DIPPIM model and the DAIMO model developed in the previous chapter (3) are compared to the reference *ab initio* calculations.

4.1.1 Ferroelectric phonon mode

In figure 4.1 and 4.2 the ferroelectric phonon mode displacements along the [001]-, [011]- and [111]-directions are plotted with the DIPPIM and DAIMO models, respectively. Both models lead to ferroelectric instabilities in the cubic phase along the three directions. The correct order of energy depth are obtained for both models, i.e. lowest energy along the [111]-direction followed by the [011]- and [001]-direction. The deepness of the energy curves obtained by the DIPPIM model are in good agreement and diverges only slightly from the DFT values with a maximum error of 0.001 eV/$BaTiO_3$. The position of the minimum is slightly shifted to smaller Ti displacements with a maximum error of -0.002 Å . In the case of the DAIMO model, the differences with the reference calculations are more pronounced, i.e. the maximum error equals 0.014 eV/$BaTiO_3$ for the depth and 0.007 Å for the position of the minima.

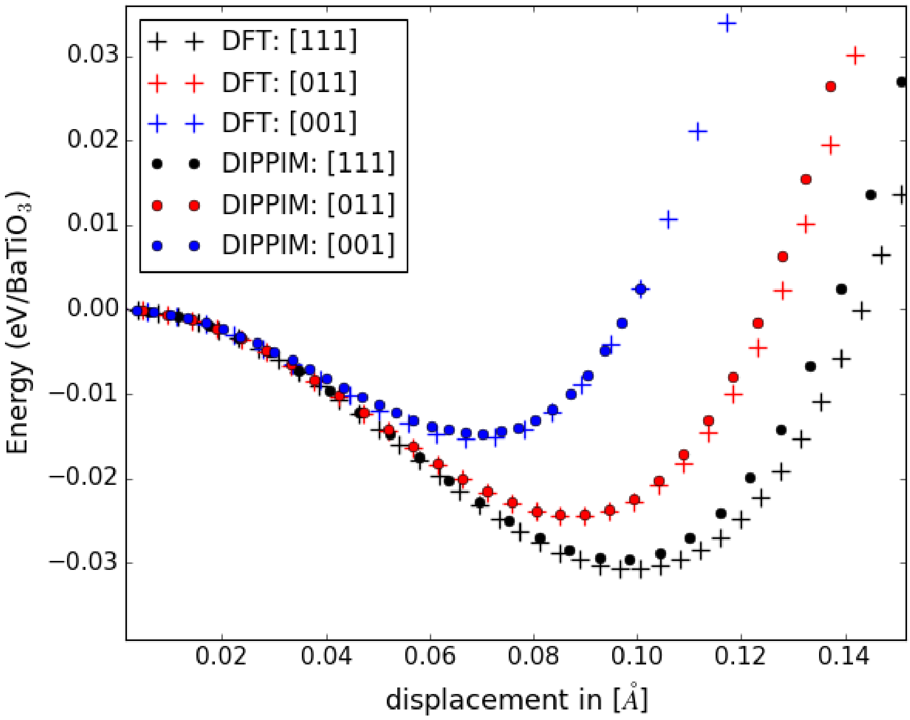

Figure 4.1: The Energy in eV per $BaTiO_3$ as a function of the Ti displacement relative to Ba in Å in cubic structure with $a = 4.00$ Å . The DFT calculations are denoted with the cross symbol and the DIPPIM model determined energies with dots.

Since the polarization in ferroelectrics is known to be strongly coupled to the stress, the behaviour of the stress tensor components are additionally examined

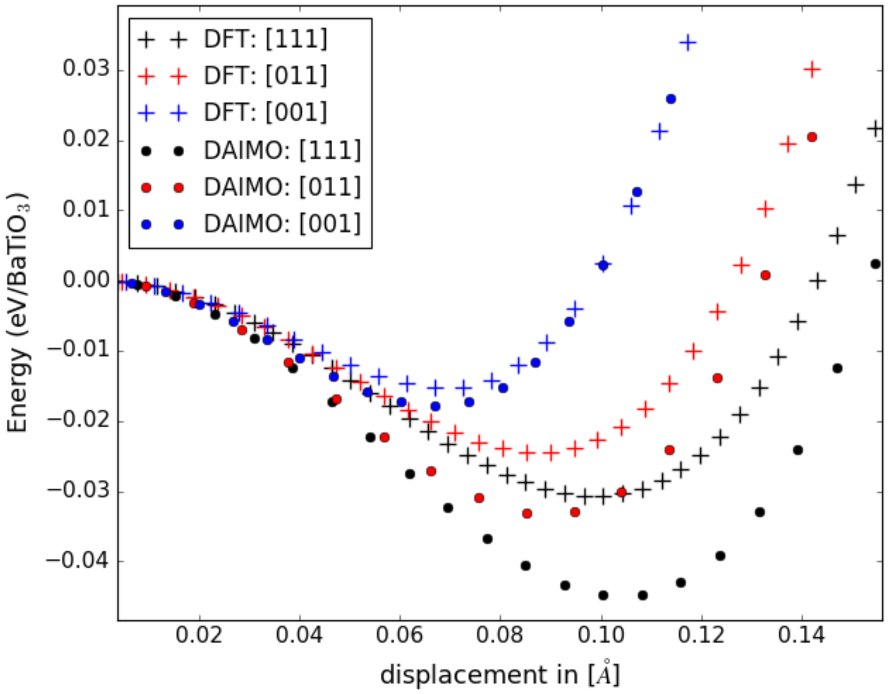

Figure 4.2: The Energy in eV per BaTiO$_3$ is shown as a function of the Ti displacement relative to Ba in Å in the cubic structure with $a = 4.00$. The DFT calculations are denoted with the cross symbol and the energies determined by the DAIMO model with dots.

as a function of atomic displacements. The soft mode patterns along the [001]-direction calculated by the DIPPIM and the DAIMO model are given in figures 4.3 and 4.4, respectively. In the [001]-soft mode displacement pattern, the titanium ion is subsequently approached towards the oxygen ion along the [001]-direction , thus creating an increasing zz-stress tensor component. At the same time, the yy- and xx stress tensor components increase together slightly. For the DIPPIM model, all diagonal components are shifted down by an amount of -0.6 GPa compared to DFT and the zz-stress tensor component increases more steeply than the DFT one. In contrast, the stress tensor components determined by the DAIMO model are in good agreement with DFT over this range of displacement amplitudes. The off-diagonal stress components lead with both models to values close to zero and are in accordance with DFT.

The stress tensor components arising for a soft mode displacement in [011]-direction are plotted in figure 4.5 and figure 4.6. The zz- and yy- stress tensor components are superposed and increase noticeably with the displacement amplitude, while the xx- stress tensor component increases less steeply. In the case of the DIPPIM model, the slopes of the diagonal components are again steeper than the DFT

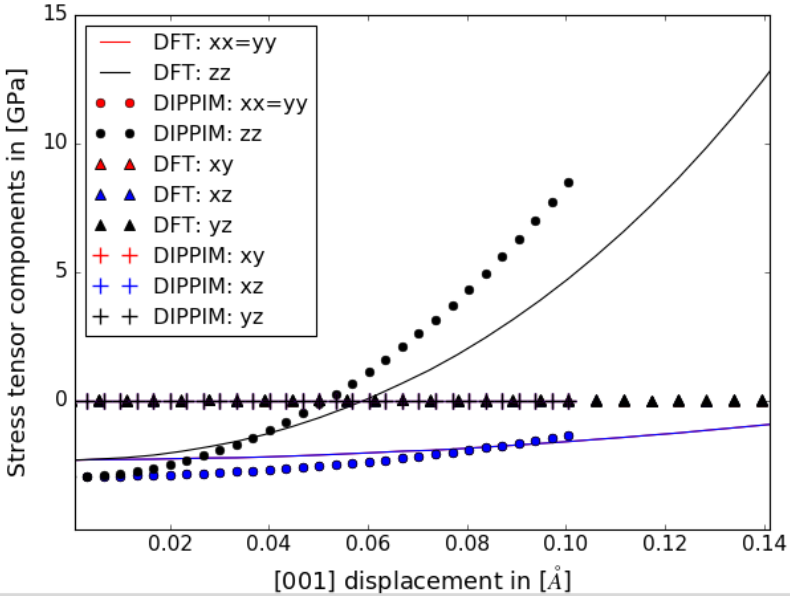

Figure 4.3: DIPPIM stress tensor components in GPa as a function of the Ti displacement relative to Ba in the [001]-direction in Å in cubic structure with $a = 4.00$ Å . The xx- and yy-stress tensor components are superposed.

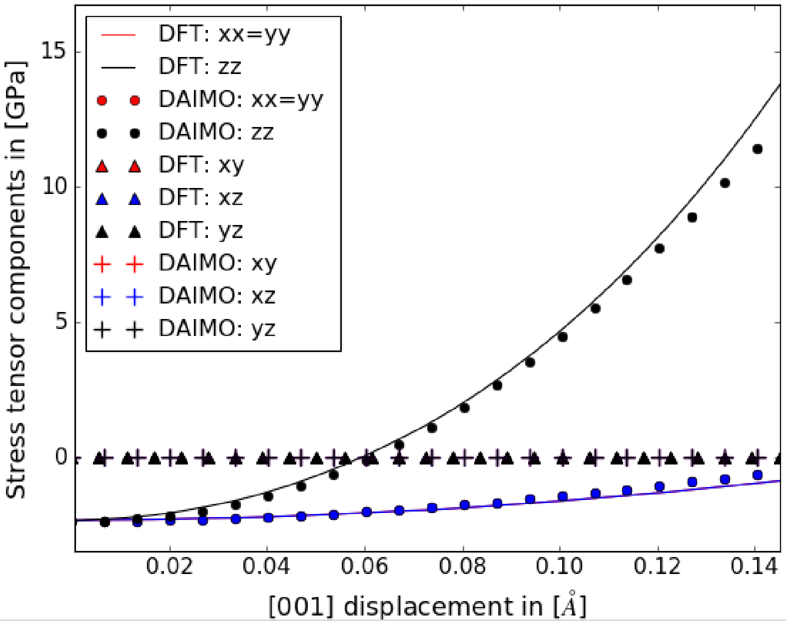

Figure 4.4: DAIMO stress tensor components in GPa as a function of the Ti displacement relative to Ba in the [001]-direction in Å in cubic structure with $a = 4.00$. The xx- and yy-stress tensor components are superposed.

predicted ones. The yz-component increases with larger displacement amplitudes, while the DFT yz-stress component remains close to zero. The DAIMO results of the diagonal and odd-diagonal stress tensor components are again in good agreement with DFT.

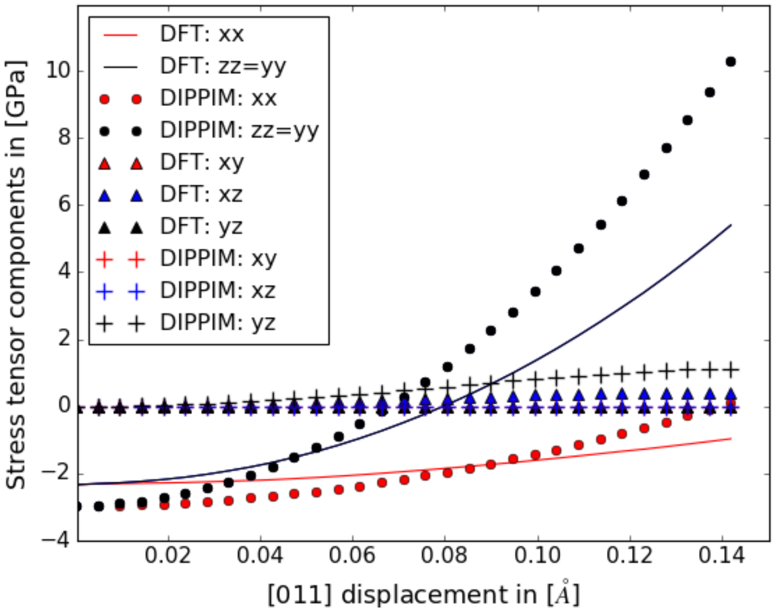

Figure 4.5: DIPPIM stress tensor components in GPa as a function of the Ti displacement relative to Ba in the [011]-direction in Å in cubic structure with $a = 4.00$ Å . The yy- and zz-stress tensor components are superposed.

In figures 4.7 and 4.8 the stress tensor components for the soft mode displacement pattern along [111]-direction are presented. In this case, the three diagonal stress tensor components are similar. The off-diagonal stress components decreases with increasing displacement amplitude. Once again, the DAIMO shows a behaviour close to the DFT calculations, while the DIPPIM is less accurate.

In conclusion, the DIPPIM model reproduces accurately the energy surface for the different soft mode displacements at a fixed volume. However, the associated stress tensor components diverge from the values predicted by DFT. The diagonal stress tensor components are shifted by -0.6 GPa suggesting that effectively this energy slopes would arise under application of positive external pressure. In the case of the DAIMO model, the sequence of energy minima in [001]-, [011]- and [111]-directions are correctly obtained, but the deepness of the energy minima is overestimated. This might enhance the effect of ferroelectric instabilities in the cubic phase. For an ideal interaction model, both stress tensor and energy slope should be well reproduced at the same time.

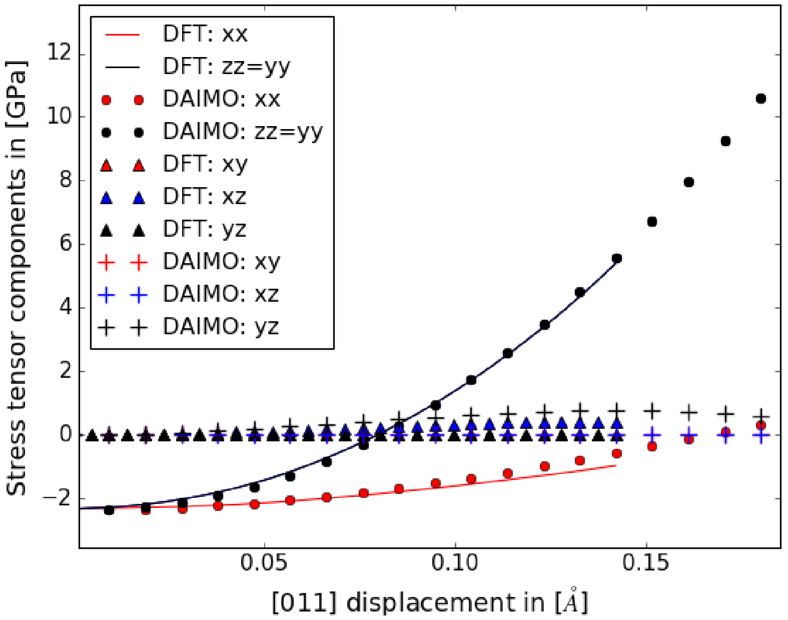

Figure 4.6: DAIMO stress tensor components in GPa as a function of the Ti displacement relative to Ba in the [011]-direction in Å in cubic structure with $a = 4.00$ Å . The yy- and zz-stress tensor components are superposed.

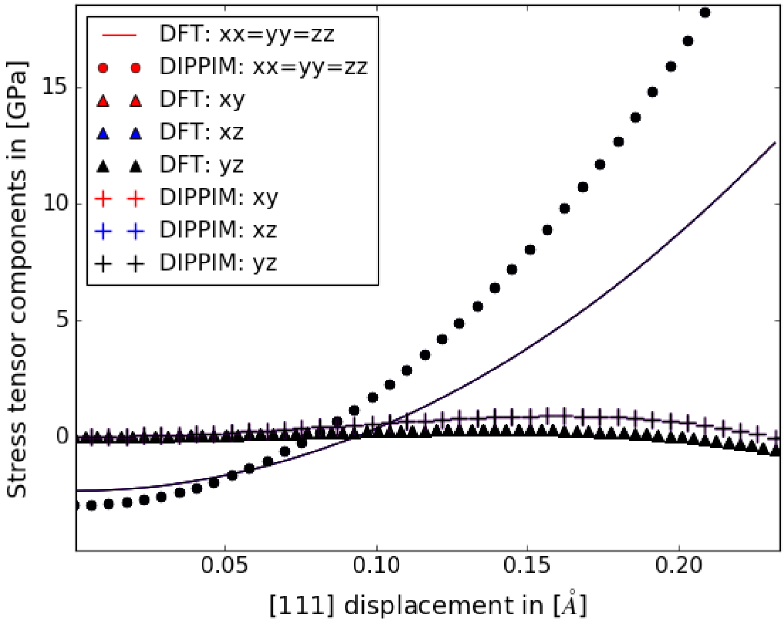

Figure 4.7: DIPPIM stress tensor components in GPa as a function of the Ti displacement relative to Ba in the [111]-direction in Å in cubic structure with $a = 4.00$ Å . The xx-, yy- and zz-stress tensor components are superposed.

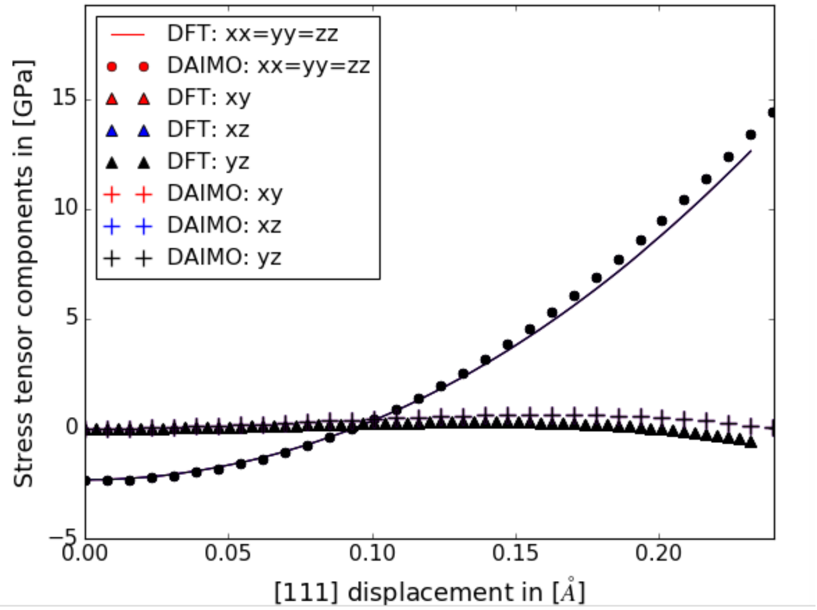

Figure 4.8: DAIMO stress tensor components in GPa as a function of the Ti displacement relative to Ba in the [111]-direction in Å in cubic structure with $a = 4.00$ Å . The xx-, yy- and zz-stress tensor components are superposed.

4.1.2 Born effective charge

4.1.3 Geometry optimization program

The aim is to perform geometry optimization under symmetry consideration, i.e. only the relevant degrees of freedom are relaxed by minimizing the total energy. The shape of the simulation cell is defined by the cell vectors $\mathbf{a} = a\,\mathbf{v}_1$, $\mathbf{b} = b\,\mathbf{v}_2$ and $\mathbf{c} = c\,\mathbf{v}_3$. $\mathbf{v}_1$, $\mathbf{v}_2$ and $\mathbf{v}_3$ are the unitary cell vectors, i.e. $\|\mathbf{v}_1\| = \|\mathbf{v}_2\| = \|\mathbf{v}_3\| = 1$, between which the angles α, β and γ are formed, see figure 4.9.

The input file 'restart1.dat' of the program contains the cell parameter a, b and c, the unitary cell vectors, $\mathbf{v}_1$, $\mathbf{v}_2$ and $\mathbf{v}_3$ and the positions of the atoms, which are given in the coordinate system defined by the unitary cell vectors ($\mathbf{v}_1$, $\mathbf{v}_2$, $\mathbf{v}_3$).

Cell parameters

Four different cases have to be considered for the three cell parameters a, b and c:

1. $a = b = c$
2. $a \neq b = c$
3. $a = b \neq c$

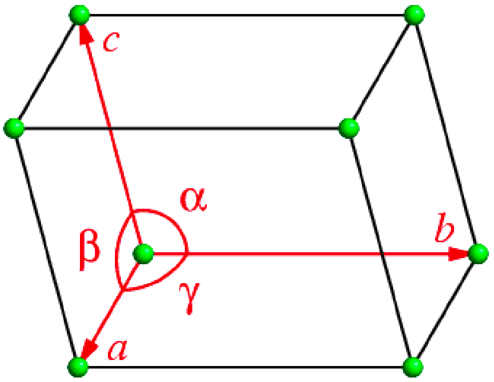

Figure 4.9: Cell shape. [117]

4. $a \neq b \neq c$.

Only one degree of freedom is associated to the first case. The new cell parameters are obtained by adding an amount δ_1, i.e. $a' = b' = c' = a + \delta_1$. The value of δ_1 is determined by minimizing the energy of the system with the Nelder-Mead algorithm as implemented in the Open Source Scientific Tools for Python (SciPy) [118], [119]. The optimization is performed in a similar way for the other cases, whereby the second and third cases include two degrees of freedoms and the fourth case three degrees of freedom.

The coordinates of the atoms have to be rescaled by $\mathbf{S} = (a'/a, b'/b, c'/c)$ after changes in the cell parameters. Thus, the new coordinates of the atoms are $\mathrm{x}' = \mathrm{x}\,\mathrm{S}$, where x is the atom position matrix.

Cell angles

The three angles α, β and γ are related to the unitary cell vectors, given in Cartesian coordinates, by the scalar product:

$$\mathbf{v}_1 \cdot \mathbf{v}_2 = \mathbf{v}_{1,x}\mathbf{v}_{2,x} + \mathbf{v}_{1,y}\mathbf{v}_{2,y} + \mathbf{v}_{1,z}\mathbf{v}_{2,z} = \cos(\gamma)\,. \tag{4.1}$$

There exists four cases, which are enumerated below:

1. $\alpha = \beta = \gamma$
2. $\alpha \neq \beta = \gamma$
3. $\alpha = \beta \neq \gamma$

4. $\alpha \neq \beta \neq \gamma$.

The procedure for changing angles according to the four cases (1.-4.) is exemplary presented for the first case: $\alpha = \beta = \gamma$. The angle is changed by an amount δ, i.e. $\gamma' = \gamma + \delta$. In the program, the first unitary cell vector $\mathbf{v}_1$ is kept fixed for any change in angles, while the remaining two unit cell vectors are changed so that the given condition is verified. The two components $v_{2,y}$ and $v_{2,z}$ are chosen to be fixed for the second unitary cell vector $\mathbf{v}_2$. The third component $v_{2,x}$ is determined by using equation 4.1 to assure that the angle between $\mathbf{v}_1$ and $\mathbf{v}_2$ is γ':

$$v_{2,x} = \frac{1}{v_{1,x}}(\cos(\gamma') - v_{1,y}v_{2,y} - v_{1,z}v_{2,z}). \tag{4.2}$$

The third unitary vector $\mathbf{v}_3$ is determined in order to fulfill the two equations $\mathbf{v}_1 \cdot \mathbf{v}_3 = \cos(\gamma')$ and $\mathbf{v}_2 \cdot \mathbf{v}_3 = \cos(\gamma')$. This set of two equations include three unknown $v_{3,x}$, $v_{3,y}$ and $v_{3,z}$. Therefore, the third component $v_{3,z}$ is chosen to be fixed. The remaining two components are obtained by solving this set of equations. The amounts of δs are associated to the change in angles and are again optimized by minimizing the energy.

Atomic positions

The atomic positions are given in the coordinate system defined by the unitary cell vectors ($\mathbf{v}_1$, $\mathbf{v}_2$, $\mathbf{v}_3$). If an atom is occupying a Wyckoff position, it belongs to a group of atoms in the cell, which are related to each other by particular symmetry operations. Its position can only be changed by conserving these symmetry relations. In the optimization program, the related degrees of freedom have to be entered by hand. There exist useful Crystallography tables that give the Wyckoff positions for different space groups, for example the Bilbao Crystallographic Server [120].

This practice is more precisely explained for the example of the rhombohedral phase of space group $R3m$: The program detects automatically the rhombohedral cell shape, i.e. $a = b = c$ and $\alpha = \beta = \gamma$. For both, cell parameters and angles, the variables δ_a and δ_α are automatically introduced. However, the degrees of freedom for the atom positions under conservation of their Wyckoff position have to be included by hand in a file called 'unitcell.dat'. The content of this file is shown in table 4.1 in the case of a rhombohedral unit cell :

In the first three lines the ion coordinates of the oxygen ions are given. The oxygen ions occupy the Wyckoff positions $3bm$. Therefore, their ion coordinates are related to two degrees of freedom, $\delta_{w,1}$ and $\delta_{w,2}$. The barium is chosen to be

Table 4.1: Content of the unitcell.dat file for rhombohedral phase

Atom	x	y	z
O1	x1	x1	z1
O2	z1	x1	x1
O3	x1	z1	x1
Ba	0.	0.	0.
Ti	z5	z5	z5

the origin of the coordinate system and thus remains unchanged, i.e. no degree of freedom is associated. Titanium occupies the highest symmetry position $1a3m$ and has therefore only one degree of freedom associated, $\delta_{w,3}$.

In the program, the variables related to the cell parameters, cell angles and positions can be optimized separately or at the same time. For the latter, the energy of the system is a function of all degrees of freedom: $E(\delta_a, \delta_\alpha, \delta_{w,1}, \delta_{w,2}, \delta_{w,3})$.

Results of the geometry optimization

After geometry optimization, it was verified that all forces on the ions are less than 0.001 eV/Å , which corresponds to the break condition in the geometry optimization of the DFT calculations carried out with VASP (see section 3.1.1). In table 4.2 the structural results of the geometry optimization of the four phases of $BaTiO_3$ are presented.A look at the structural results can give insight into the accuracy of the DIPPIM and DAIMO models.

The cubic phase is well reproduced by the DIPPIM model. The DAIMO model overestimated the cell parameter by 0.4 % .

The tetragonal phase shows good agreement in the cell shape with both models, even though the c/a ratio is slightly overestimated by the DIPPIM model. However, the DIPPIM model does not accurately reproduce the relative atomic displacements. The titanium displacement is overestimated by 0.008 c and the oxygen displacement by nearly the same amount leading to similar Ti-O bond lengths. The BaO and BaTi bond lengths are less well described within the DIPPIM model, as oxygen and titanium are shifted along the c-axes with respect to barium. In contrast, the DAIMO model leads to a good accordance with the reference PBEsol atom displacements.

For both models the cell shape as well as the relative displacements in the orthorhombic phase are similar to the DFT optimized results. With the DIPPIM model the b and c parameters are slightly overestimated and thus a greater cell volume is obtained. This means that with the models the positions of the energy minimum for the orthorhombic phase is in good agreement with DFT. However, this does not imply a correct relative stabilization energy.

In the rhombohedral phase the DIPPIM results coincide less well with the reference calculations. The cell parameters are overestimated by 0.6 % resulting in a too large cell volume. Furthermore the atomic displacements are overestimated for each ionic species. The agreement in cell shape and atomic displacements is satisfying with the DAIMO model.

Table 4.2: Cell parameters, angles and atom displacement in the four phases of $BaTiO_3$

Cubic phase	DIPPIM	DAIMO	PBEsol
a[Å]	3.985	4.001	3.985
V[Å^3]	63.301	64.426	63.290
Tetragonal phase			
a[Å]	3.971	3.971	3.968
c/a	1.0287	1.025	1.0261
Δ_{Ti}	0.0245	0.0173	0.0168
Δ_{O1}	-0.0236	-0.0307	-0.0316
Δ_{O2}	-0.0108	-0.0211	-0.0187
V[Å^3]	64.392	64.183	64.115
Orthorhombic phase			
a[Å]	3.963	3.965	3.961
b[Å]	5.714	5.684	5.683
c[Å]	5.714	5.716	5.696
Δ_{Ti}	0.0144	0.0147	0.0141
Δ_{O1}	0.0235	-0.0245	-0.0236
Δ_{O2}	-0.0156	-0.0175	-0.0156
Δ_{O3}	-0.0126	-0.0149	-0.0129
V[Å^3]	64.697	64.390	64.306
Rhombohedral phase			
a[Å]	4.033	4.010	4.007
α [$\circ$]	89.711	89.79	89.85
Δ_{Ti}	-0.0149	-0.0130	-0.0122
Δ_{O1}	0.0144	0.0135	0.0117
Δ_{O2}	0.0250	0.0210	0.0192
V[Å^3]	65.609	64.486	64.346

In table 4.3 the related energetics obtained by the DIPPIM for each geometry optimized structures are listed. First, it is to notice, that the stabilization energies predict the tetragonal phase to be the most stable one followed by the orthorhombic, rhombohedral and cubic phase. It is thus not in agreement with the expected phase transition sequence (rhombohedral, orthorhombic, tetragonal, cubic). However, the total electrostatic energy gives the right order, but relative stabilization energies are much weaker than the results given by the DFT geometry optimized structures with extracted dipoles. In order to identify the origin of the weakening ferroelectric stabilization, the different contributions to the total electrostatic energy are discussed in the following. The q-q interaction follows the same tendency but intensifies the energy differences between the optimized structures. This gives more weight to the destabilization of ferroelectric phases. To remind, DFT extracted dipole moments include both asymptotic and short range contributions, while the DIPPIM potential has to include an extra interaction term due to the short range effects, which are only considered in the charge-dipole interaction term (see section 2.1.4). Thus, the q-μ term with DFT extracted dipole moments are compared to the q-μ interaction term including the damping function for short range correction. In contrast to the q-q interaction term, the q-μ term lowers energy for ferroelectric phases. However, the lowering is much less pronounced within the DIPPIM model. Nevertheless, the μ-μ interaction is not able to overcome the deficit in energy stabilisation given by the q-μ term. Hence, the electrostatic interactions are not strong enough with respect to the short range repulsion (Rep) to ensure the right order of stabilization energy. This reflects again the delicate balance between short range and long range interactions. Furthermore, the correct energetic description of the model also depends on the correct repartition between asymptotic and short range induced dipoles. In fact, the right order of the phase transitions arises subtracting the energy related to the short range induced dipoles (SR(q-μ)) from the total energy (Total), see last column in table 4.3. Even if the obtained relative energies are too large, it shows the sensitivity of the division of the different contributions to the dipole moment on the energy. For this reason, the modified fitting methodology including energy differences as described in section 3.2.2 represents an interesting tool to avoid compensation errors between asymptotic and short range contribution to the dipole moment.

In conclusion, the DIPPIM model is not able to reproduce the right order of relative stabilization energies. This shows that the reproduction of ferroelectric instabilities in the cubic phase (see section 4.1.1) does not represent a sufficient condition for successful modelling of ferroelectrics. With this DIPPIM model no further studies at finite temperature are presented, as the zero temperature properties are not

Table 4.3: The total DIPPIM interaction energy at the optimized structures is decomposed in its different sub-terms in table 4.3. These are the charge-charge (q-q), charge-dipole (q-μ), dipole-dipole (μ-μ), the short range correction to the charge-dipole interaction (SR(q-μ)), the polarization energy (Polar), the total electrostatic energy (Elec), short range repulsion (Rep), the total energy (Total: Elec + Short range repulsion) and finally the total energy minus the SR(q-μ) term. The energies are given in meV/$BaTiO_3$.

Phase	q-q	q-μ	μ-μ	SR(q-μ)	Polar	Elec	Rep	**Total**	Total-SR(q-μ)
cubic									
DIPPIM	-178.884					-178.884	30.490	**-148.395**	
'PBEsol'	-178.894					-178.894			
tetragonal									
DIPPIM	-178.546	-1.261	-0.270	0.755	1.045	-179.031	26.860	**-152.171**	-152.926
'PBEsol'	-178.849	-1.743	-0.063			-180.655			
orthorhombic									
DIPPIM	-178.462	-1.599	-0.347	0.948	1.344	-179.064	26.896	**-152.168**	-153.117
'PBEsol'	-178.812	-2.224	-0.081			-181.117			
rhombohedral									
DIPPIM	-178.229	-1.900	-0.528	2.145	1.478	-179.179	27.015	**-152.163**	-154.309
'PBEsol'	-178.804	-2.366	-0.093			-181.263			

satisfying.

In table 4.4 the relative stabilization energies obtained with DAIMO taking the cubic phase as reference are listed. The order of phase transition is reproduced with the DAIMO model. The relative stabilization energies are overestimated compared to the PBEsol values. Summing up, the zero temperature properties of the DAIMO model are satisfying and seems to incorporate the necessary ingredients to reproduce ferroelectricity.

Table 4.4: Energy differences of the ferroelectric phases of $BaTiO_3$ with respect to cubic phase in meV/$BaTiO_3$

Phase	DAIMO	PBEsol	PBE0[99]
tetragonal	-23.5	-19.9	-33.7
orthorhombic	-35.6	-25.0	-42.5
rhombohedral	-44.3	-26.7	-44.1

4.1.4 Bulk modulus

The phase transition in $BaTiO_3$ involve changes of the cell shape. Thus, the PIM interaction potentials should be able to describe correctly the change in energy accompanied with the deformation of the cell shape. This can be quantified by evaluation of the elastic constants and bulk modulus.

The elastic constants of a material c_{ij} relate the stress tensor σ_i to the strain tensor ϵ_i:

$$\sigma_i = \sum_j c_{ij}\epsilon_j. \tag{4.3}$$

The Voigt notation has been employed in the previous expression.[1] The elastic constants represent the stiffness of the material since the stress tensor is associated to the force and the strain tensor characterizes the amount of deformation.

The bulk modulus B expresses the incompressibility of a material to uniform compression and is defined as the infinitesimal change in pressure with respect to the infinitesimal relative change in volume:

$$B = -\Omega\frac{\partial p}{\partial \Omega}. \tag{4.4}$$

---

[1] The Voigt notation is a convention that reduced the order of a symmetric tensor (for details see for example [121]).

It is possible to express the bulk modulus as a function of the elastic constants by the linearisation of the equation 4.4:

$$B = \sigma \frac{\mathit{\Omega}}{\mathit{\Delta\Omega}} \tag{4.5}$$

with the finite change in volume $\mathit{\Delta\Omega}$. The magnitude of the applied hydrostatic stress tensor is σ. Since the stress is uniform, the stress tensor is given by:

$$\sigma = (\sigma\ \sigma\ \sigma\ 0\ 0\ 0)^T. \tag{4.6}$$

The resulting strain tensor is also uniform for the cubic phase structure:

$$\epsilon = (\epsilon\ \epsilon\ \epsilon\ 0\ 0\ 0)^T \tag{4.7}$$

and thus the relative finite change in volume can be written as:

$$\frac{\mathit{\Delta\Omega}}{\mathit{\Omega}} = 3\epsilon. \tag{4.8}$$

The relative finite change in volume 4.8 is inserted in the expression of the linearised bulk modulus 4.5. Furthermore, σ is expressed as a function of elastic constants 4.3, whereat in cubic phase c_{12} equals c_{13}:

$$B = \frac{1}{3}(c_{11} + 2c_{12}). \tag{4.9}$$

The linear relation between strain and stress 4.3 is employed for the calculation of the elastic constants. Therefore, the cubic cell structure optimized in the previous section is used and is strained by a small amount of positive and negative values. Then, the resulting stress tensor is determined and the elastic constants are extracted.

In the cubic phase, three different deformations are carried out for independent determination of the three independent elastic constants $c_{11} = c_{22} = c_{33}, c_{12} = c_{13}, c_{23}$ and $c_{44} = c_{55} = c_{66}$. The results of the calculations of the elastic constants and bulk modulus in the cubic phase are listed in table 4.5. The experimentally determined elastic constants differ from the DFT values and furthermore the different E_{XC}-functionals lead to different results. However, the global tendency is respected, i.e. the highest elastic constant is c_{11}, followed by c_{44} and c_{12}.

The elastic constants are not in good agreement with the reference PBEsol values for both the DIPPIM and DAIMO. The DIPPIM overestimates the c_{11} and c_{44}, but underestimates the c_{12}. Nevertheless, the results for the bulk modulus is in better agreement with the PBEsol value. That means that the effect of uniform pressure is better described by the DIPPIM than the separated effect of contraction and expansion of a single cell parameter. In the case of the DAIMO, all elastic constants are overestimated by around 60 GPa in comparison to the PBEsol predictions. As a direct consequence the bulk modulus is also overestimated by a similar amount and the incompressibility of the system is increased.

Table 4.5: Elastic constants and bulk modulus in GPa in the cubic structure

	c_{11}	c_{12}	c_{44}	B_0
Expt. [112]	255	82	108	140
LDA [107]	305	106	128	172
B3LYP [29]	298	116	145	176
PBEsol	318	113	127	181
PIM	387	95	196	192
DAIMO	383	158	196	233

4.2 Finite temperature properties

The zero temperature calculation revealed that the DAIMO model follows the right order of stabilization energy and shows ferroelectric instabilities in the cubic phase according to the soft mode concept. In order to further investigate if the DAIMO model is able to reproduce ferroelectricity at finite temperature, MD calculations are carried out. In the first part of the chapter the basics of Molecular Dynamic (MD) simulations are reviewed. In the second part, MD simulations are performed to obtain the phase transitions and related quantities, i.e. transition temperatures, polarization density and cell parameter as a function of temperature.

4.2.1 Basics of MD simulation and ensembles

In Molecular Dynamics simulations the macroscopic properties of a system are explored through simulations at the microscopic scale. Thereby, the ergodic hypothesis relates the time average of the instantaneous value of a physical quantity to its macroscopic value. The time evolution of the system is realized by numerical integration of Newton's second law: $\mathbf{F} = m\mathbf{a}$. The force $\mathbf{F}$ can be written as the negative gradient of the potential energy. Thus, the equation of motion for a classical interacting particle i at position $\mathbf{r}_i$ is given by:

$$\mathbf{a}_i m_i = \mathbf{F}_i = -\frac{\partial U(\mathbf{r}_i)}{\partial \mathbf{r}_i}. \tag{4.10}$$

There exist many different algorithms that have been developed for the numerical resolution of equation 4.10. The main idea of the algorithms consists in discretizing the time t in small stages δt. Starting from the force at time t, the acceleration of the particle is determined and related to the positions and velocities at time t in order to get an estimation of the positions and velocities at subsequent time $t + \delta t$. The force is assumed to be constant during a time step. In this thesis, the Leapfrog Verlet algorithm is used (for details of the derivation see for example [122]).

$$\mathbf{v}_i(t + \frac{\delta t}{2}) = \mathbf{v}_i(t - \frac{1}{2}\delta t) + \mathbf{a}(t)\delta t \tag{4.11}$$

$$\mathbf{r}_i(t + \delta t) = \mathbf{r}_i(t) + \mathbf{v}_i(t + \frac{1}{2}\delta t)\delta t. \tag{4.12}$$

If the dynamics are ergodic, the sampling of the phase space corresponds to the micro-canonical ensemble (NVE), in which the number of particles, volume and total energy are conserved.

In the NVT ensemble the system is coupled to an external heat bath, i.e. thermostat. One of the most commonly used algorithms is the Nos$\acute{e}$-Hoover thermostat [123]. Thereby, an additional degree of freedom for the heat bath is introduced. This additional degree of freedom is coupled to the kinetic energy so that the average temperature is constant. The modified equations of motion with the Nos$\acute{e}$-Hoover thermostat are given by:

$$m\mathbf{a}_i = -\frac{\partial U(\mathbf{r}_i)}{\partial \mathbf{r}_i} - \mathbf{p}_i \frac{p_\eta}{Q}. \tag{4.13}$$

This equation contains a friction term additionally to the potential derived force, which should control the kinetic energy. The average temperature fluctuates around the temperature of the heat bath T_{ext}. The time dependence of the additional degree of freedom η is given by:

$$\dot{p}_\eta = \sum_{i=1}^{3N} \frac{|\mathbf{p}_i^2|}{m_i} - 3Nk_B T_{ext} \tag{4.14}$$

$$\frac{d\eta}{dt} = \frac{p_\eta}{Q} \tag{4.15}$$

where Q stands for the effective mass associated to the thermostat. The effective mass is proportional to the square of the relaxation time τ, which is an input parameter that gives the strength of the coupling between the system and the thermostat. If a small value for τ is chosen, then the derivative of η is large according to equation 4.15. In turn, this increases the friction term in equation 4.13. Thus, the system is considered to be strongly coupled to the thermostat in this case.

Even if the Nosé-Hoover thermostat has been widely employed, it does not verify the hypothesis of ergodicity for low dimensional systems. For this reason, in this work Molecular Dynamic simulations have been performed using the approach of Martyna *et al.* [124]. The method of Martyna *et al.* modifies the algorithm of Nosé-Hoover to assure ergodicity in order to produce a canonical distribution by increasing the dimensionality of the system. The idea is to extend the dynamic of Nosé-Hoover to a chain of thermostats by introducing new system variables. The thermostat chains (M) couple the system to a first thermostat η_1, which is in equilibrium with the system, while successive thermostats η_j are at equilibrium with the next thermostat in the chain η_{j+1}. The equations of motion with the technique of Martyna *et al.* become:

$$\mathbf{a}_i = -\frac{\partial U(\mathbf{r}_i)}{\partial \mathbf{r}_i} - \mathbf{p}_i \frac{p_{\eta_1}}{Q_1} \tag{4.16}$$

$$\frac{d\eta_j}{dt} = \frac{p_{\eta_j}}{Q_j} \tag{4.17}$$

$$\dot{p}_{\eta_1} = \left(\sum_i^{N_{df}} \frac{\mathbf{p}_i^2}{m_i} - N_{df} k_B T \right) - p_{\eta_1} \frac{p_{\eta_2}}{Q_2} \tag{4.18}$$

$$\dot{p}_{\eta_j} = \left[\frac{p_{\eta_{j-1}}^2}{Q_{j-1}} - k_B T \right] - p_{\eta_j} \frac{p_{\eta_{j+1}}}{Q_{j+1}} \tag{4.19}$$

$$\dot{p}_{\eta_M} = \left(\frac{p_{\eta_{M-1}}^2}{Q_{M-1}} - k_B T \right) \tag{4.20}$$

and the Hamiltonian is

$$H_{NVT} = U + \sum_{i=1}^{N_{df}} \frac{\mathbf{p}_i^2}{2m_i} + \frac{p_\eta^2}{2Q} + N k_B T \eta_1 + \sum_{j=2}^{M} k_B T \eta_j . \tag{4.21}$$

In the present implementation of the thermostat of Martyna *et al.* two chains are used.

Typical conditions of experimental measurements are constant temperature and pressure. In statistical mechanics this conditions are described in the isothermal-isobaric ensemble (NPT). Therefore, Martyna *et al.* couples the previously introduced thermostat with a barostat of momentum p_ϵ and the equation of motion becomes:

$$\mathbf{a}_i = -\frac{\partial U(\mathbf{r}_i)}{\partial \mathbf{r}_i} - \mathbf{p}_i \frac{p_\epsilon}{W} - \mathbf{p}_i \frac{p_\eta}{Q} \tag{4.22}$$

where the change in volume is related to the momentum p_ϵ as follows:

$$\frac{dV}{dt} = \frac{dV p_\epsilon}{W}. \tag{4.23}$$

The derivative of the momentum p_ϵ for a given set of internal, P_{int}, and external, P_{ext}, pressures is:

$$\dot{p}_\epsilon = dV\left(P_{\text{int}} - P_{\text{ext}}\right) - \frac{p_\eta p_\epsilon}{Q}. \tag{4.24}$$

The thermostat parameters is given by:

$$\frac{d\eta}{dt} = \frac{p_\eta}{Q}. \tag{4.25}$$

Finally, the equations of the chain of length M are given by:

$$\dot{p}_{\eta_1} = \sum_{i=1}^{N} \frac{\mathbf{p}_i^2}{m_i} + \frac{p_\epsilon^2}{W} - \left(N_{df} + 1\right) k_B T. \tag{4.26}$$

The Hamiltonian for this ensemble is:

$$H_{NPT} = \sum_{i=1}^{N} \frac{\mathbf{p}_i^2}{2m_i} + \frac{p_\epsilon^2}{2W} + \frac{p_\eta^2}{2Q} + U + \left(N_{df} + 1\right) k_B T \eta + P_{\text{ext}} V. \tag{4.27}$$

4.2.2 DAIM Molecular Dynamics

Super-cell size

As highlighted by different authors, the ferroelectric instability in the cubic phase can only arise for Ti-O chains with a length greater than the critical correlation length. The correlation length for $BaTiO_3$ was estimated to equal four times the unit cell parameter. [46] [94]

As a consequence of this matter of fact, the finite temperature simulation of bulk $BaTiO_3$ using periodic boundary conditions needs a careful choice of the super cell size. At finite temperature, thermal fluctuations might break correlation by switching the direction of the polarization of one of the unit cells in the chain. Periodic boundary conditions replicate this decorrelation in the images. For a 3x3x3 super cell, this means that already one non correlated unit-cell break ferroelectricity because of the impossibility to form a chain equal or greater than the critical correlation length.

In order to determine the super-cell size, Molecular Dynamics in the NPT ensemble for different super cell sizes have been carried out. The calculation were performed at atmospheric pressure and at a temperature of 50K, for which rhombohedral phase is expected to be stable. All calculations were started with the 0K geometry optimized rhombohedral structure (see section 4.1.3). For the study of the dependence of super cell size the time step has been set to 16.537 a.u (0.4 fs) and the thermostat and barostat coupling constants are 0.2ps and 4ps, respectively. During the simulation, the structure remains rhombohedral independent of the cell shape with three equal polarization density components. This means, that at 50K thermal fluctuations are not strong enough to overcome the energy barrier for decorrelation. In figure 4.10, the evolution of one the polarisation density components over time and for different super super-cell sizes are plotted. The effect of coupling to the thermostat lead to oscillations in polarization density.

For any super-cell size the polarization component fluctuates around 0.20 $\mathrm{C/m^2}$. In the 3x3x3 super-cell, the fluctuations of the polarization density are very important and take values between 0.16 $\mathrm{C/m^2}$ and 0.23 $\mathrm{C/m^2}$. Strong fluctuations are as well present in all output quantities of the MD simulation, i.e. temperature, pressure, cell parameters etc. The intensity of fluctuations decreases with increasing super-cell size. For instance, a 7x7x7 super-cell size is used for MD calculations for which, at least at 50K, the amplitude of fluctuations are reasonable. Furthermore calculations with a 7x7x7 super-cell are less computational expensive than calculations with a 9x9x9 super-cell.

Polarization density

The polarization density of the simulation cell is calculated by taking the average of the polarization densities over the unit cells. To remind, the expression for the polarization density of a unit cell introduced in sec. 3.1.2 is:

$$\mathbf{P} = \frac{1}{\Omega} \sum_{i=1} \omega (q_i \mathbf{r}_i + \mathbf{d}_i). \tag{4.28}$$

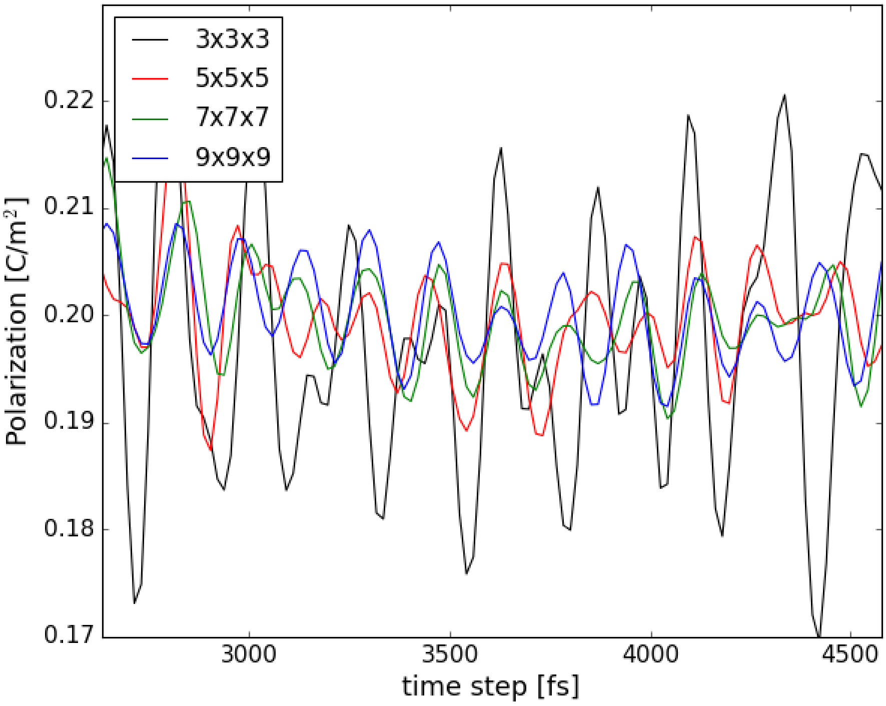

Figure 4.10: Polarization density component in C/m^2 as a function of the time in fs at 50K.

In order to obtain the evolution of the polarization density, MD calculations were carried out employing the NPT ensemble at external atmospheric pressure. The time step were set to 0.4 fs. The thermostat and barostat coupling constants were set to 0.2 ps and 4 ps, respectively. A 7x7x7 super-cell was used with periodic boundary conditions. Over a temperature range between 30 K to 250 K, every 10 K the system was simulated. The system was equilibrated for 2 ps and followed by a simulations run of 12 ps at each temperature. In figure 4.11 the three components of the mean polarization are plotted as a function of temperature. The cell lattice constants are displayed in figure 4.12. At low temperature all three mean polarization components are non zero and almost equal. Furthermore, the three lattice parameters are also almost identical indicating that the structure is rhombohedral at low temperature. As the system is heated up to 120 K, the polarization density decreases slightly and continuously, while the cell parameters increase at the same time due to thermal expansion. The cell parameters start to diverge slightly from 120 K to 160 K and the slope of the polarization density decrease is a bit steeper. Nonetheless, the structure can still be considered to be rhombohedral as the divergence of cell parameters and polarization components are small. Between 160 K and 210 K, the behaviour in cell parameters and polarizations is diffuse. The cell parameters can no longer be considered to be equal and they fluctuate between 4.002 Å and 4.023 Å . Over this range of temperature, the polarization density goes almost to zero, but presents strong fluctuations, too. Hence, in this range of temperature it is not possible to clearly identify a phase. By further increase of temperature above 210 K, an average paraelectric cubic phase is reached, whose cell parameters are again almost equal and with the polarization density components close to zero.

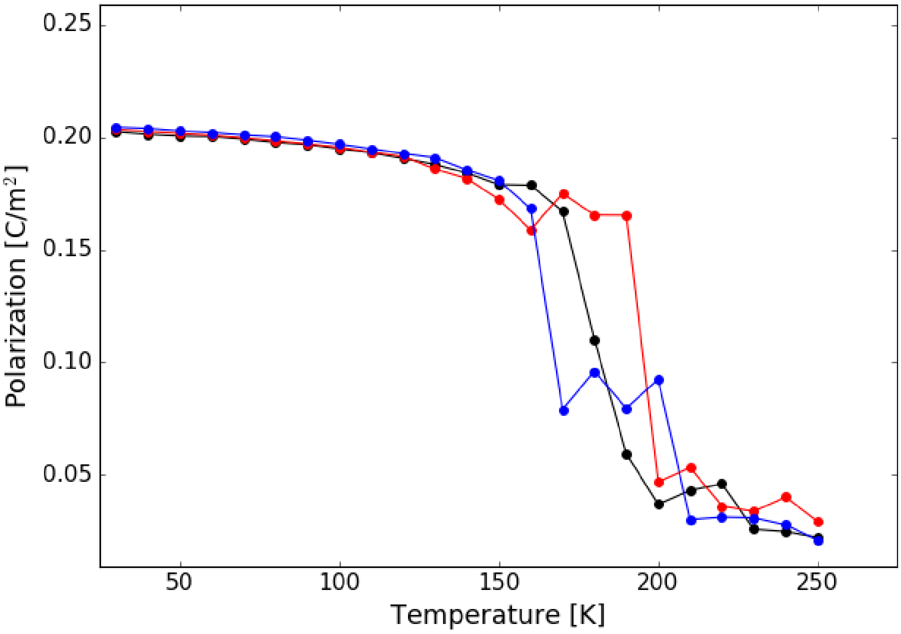

Figure 4.11: Polarization density components in C/m^2 as a function of temperature.

In the temperature range of 160 K and 210 K, it is not possible to clearly identify a phase. Possible reasons for the strong fluctuations might be i) too short simulation time ii) size of the simulation cell iii) coupling to the barostat and thermostat or iv) inherent to the interaction potential. In order to study the dependence on simulation run time, the length of the simulation time was increased from 12 ps to 27.16 ps for the temperature 190 K. The results for the polarization components for the 12 ps are 0.059 C/m^2, 0.165 C/m^2 and 0.080 C/m^2 and for the 27.16 ps run 0.074 C/m^2, 0.102 C/m^2 and 0.081 C/m^2. The average cell parameters are in the 12 ps case 4.007 Å , 4.020 Å and 4.010 Å and in the 27.16 ps case 4.011 Å , 4.012 Å and 4.015 Å . Thus, the results of the 12 ps and the 27.16 ps simulation time differ from each other. In both cases no clear identification of the phase at this temperature is possible. In figure 4.13 an extract of the evolution of the three polarization components as a function of time at 190 K is given.

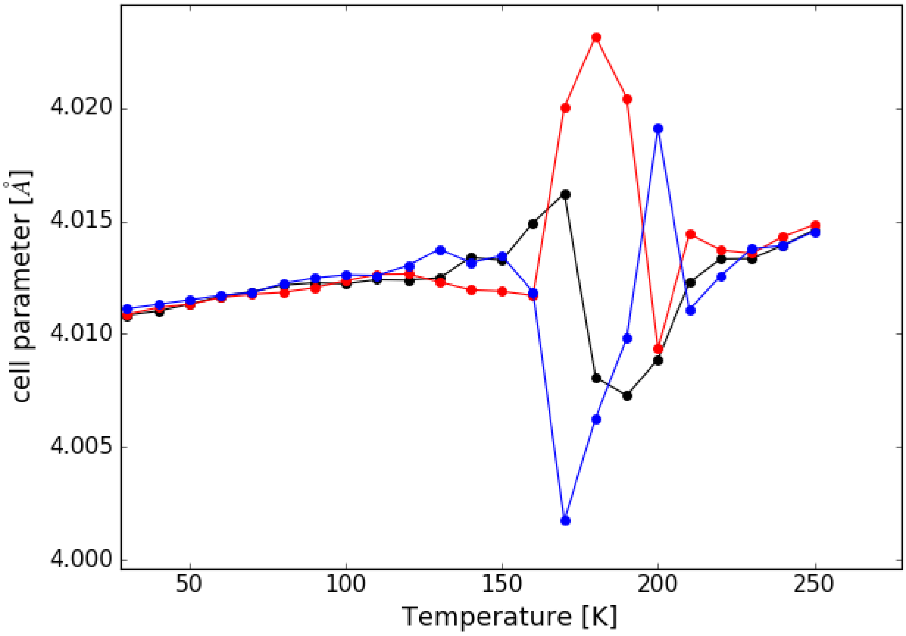

Figure 4.12: Cell parameters in Å as a function of the temperature.

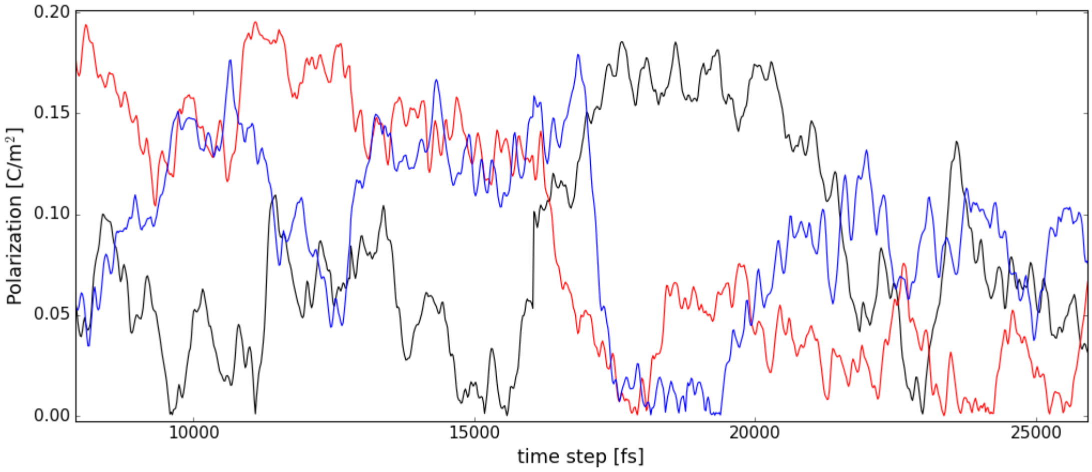

Figure 4.13: Polarization density components in $\mathrm{C/m^2}$ as a function of the time in fs at 190K.

The polarization components present strong fluctuations and at different times the system switches between tetragonal or orthorhombic-like states with one or two polarization components of values much lower than the others. Furthermore, the following tendency can be observed: the value of the polarization is accompanied with small tetragonal and orthorhombic-like distortions, see figure 4.14. Thereby, the simulation cell distorts along different axes at different time steps and it seems that the axis are exchanged.

To identify, whether the strong fluctuation is due to an inherent inaccuracy in

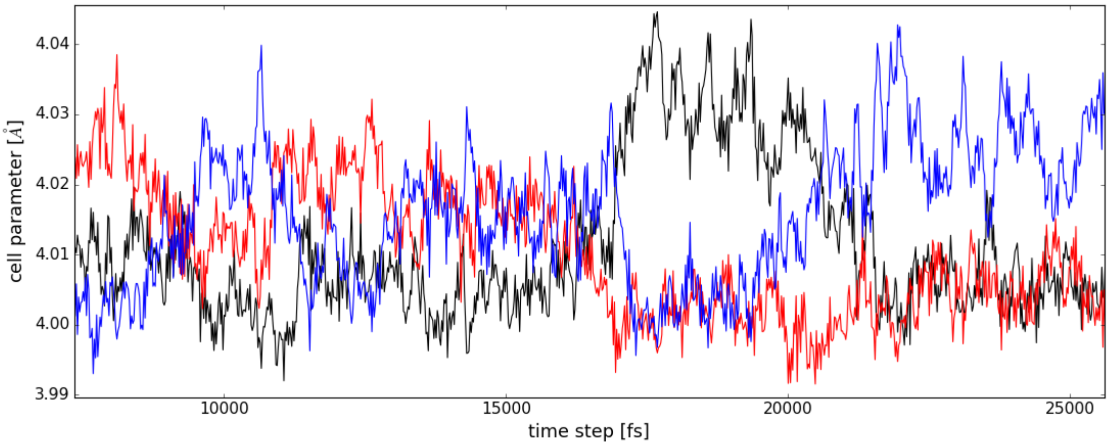

Figure 4.14: cell parameters in Å as a function of the time in fs at 190K.

the model or due to the simulation conditions, the dependency on other quantities, such as super-cell size, coupling of the system to the thermostat and barostat, need further investigation.

4.3 Conclusion

In summary, the DIPPIM and the DAIMO potentials lead to ferroelectric instabilities in the cubic phase. The models describe either very accurately the energy slopes or the associated stress tensor evolution, but none of them both quantities at the same time. The elastic constants in the cubic phase are worse described with the DIPPIM. The DAIMO model reproduces the correct tendency of the elastic constants but increases the incompressibility of the material. The geometry optimization demonstrated, that the DIPPIM predicts the tetragonal phase to be the most stable. It has been pointed out that this is due to a wrong description of the delicate balance between short range and long range interaction terms. An additional reason may be the incorrect repartition between asymptotic and short range contributions to the dipole moment. In the case of the DAIMO, the right order of stabilization energies between the various phases was obtained and structural properties were in satisfying agreement with the references values. Then, finite temperature MD simulations have been performed with the DAIMO model. The results show, that the model predicts the rombohedral phase to be stable at low temperature until 160 K. In the temperature range between 160 K and 210 K the structure fluctuates strongly and no phase can be clearly identified. Above 210 K the structure stabilizes in the paraelectric cubic phase.

Chapter 5

Conclusion and prospects

Ferroelectric based compounds present a wide range of outstanding properties which are of fundamental and industrial interest. The heart of the thesis was the development of a Polarizable Ion Model for $BaTiO_3$, a prototype perovskite ferroelectric.

In the first chapter of the thesis, the three most common simulation techniques for ferroelectrics have been reviewed: the Density Functional Theory, the Effective Hamiltonian approach and the Shell model. The discussion about the current modelling techniques of $BaTiO_3$ highlights two main points. First, the Density Functional Theory (DFT) was successful for the determination of several ferroelectric properties at atomic scale. However, DFT calculations are usual restricted to zero-temperature calculations, small sized systems and short time-scale simulations. Nevertheless, the fact that in general the DFT calculations are very accurate and can be obtained even when experimental measurement are not available, makes DFT attractive for the development of second principle methods. The second point to emphasis is that second principle methods, whose set of parameters are fully derived from first principle calculations, have been successfully applied to ferroelectric compounds. Thus in the last decades, second principle methods, such as the Effective Hamiltonian approach and the Shell model, were able to be simulate the correct phase transition sequence and a wide range of other ferroelectric properties at finite temperature and larger time and length scales. The success of second principle methods, demonstrated that the zero Kelvin energy surface obtained with DFT, include the necessary ingredients to capture ferroelectric properties even at finite temperature. Nevertheless, the Effective Hamiltonian approach and the Shell model presents similar restrictions, which makes them hardly applicable to the investigation of defects and surface effects. The arguments given above supports the objective to develop a new family of interaction potentials fully derived from DFT calculations, but with the aim to be able to simulate more easily complex ferroelectric based compounds by employing nominal charged ions.

In the second chapter, the Polarizable Ion Model (PIM) was presented. A special consideration was given on the importance of a precise description of polarization effects in ionic oxides. It has been highlighted that both asymptotic and short-range effects to the many-body induced dipoles play a crucial role. The advantage of the PIM model is that these many-body effects are explicitly included in the model. Then, the methodology of parametrization of PIM models in literature was explained by means of some representative literature examples for PIM models. The discussion about the literature PIM models points out that the PIM model is suitable for simple alkaline earth oxides and is able to reproduce quantitatively the complex pressure driven phase transition in BaO and to provide additional insight in the transition mechanism at atomic level. Furthermore, it has been pointed out that the reproduction of phase transitions sequence presents a very challenging task for systems with small energy differences between phases at the order of some meV per chemical unit formula. In fact, an example in literature for a PIM model for TiO_2 has been reviewed and shown not to be able to achieve the correct order of stabilization energies.

The development of a Polarizable Ion Model was the subject of the third chapter. In the first section of the third chapter, a convergence test was carried out for the identification of the technical settings for accurate DFT calculation using the PBEsol Exchange-correlation functional as implemented in VASP. Then several zero temperature properties were calculated and compared to experimental and theoretical findings. The PBEsol functional was shown to reproduce the correct order of relative stabilization energies between phases, structural properties and the ferroelectric phonon mode. Therefore, the PBEsol functional seems to be adapted for the parametrization of a PIM model for ferroelectric $BaTiO_3$.

The main motivation of the PIM model consists in the use of nominal charged ions making such types of potential more transferable. Furthermore, the ions are considered to be polarizable up to dipolar order. To remind, a purely nominal charged ionic description of $BaTiO_3$ would lead to the ideal paraelectric perovskite structure. As a consequence, ferroelectricity within the PIM model can only be achieved through the polarizability of the ions. In the following section the hypothesis was tested. Therefore, several key quantities were calculated under the use of the nominal charged ions. The foregoing investigation led to the conclusion that the error introduced by simplifying the system under application of this hypothesis is acceptable and of the same order than the Shell Model, which in contrast to the PIM model includes a static charge transfer. In the second part of this chapter, it was revealed that the actual fitting procedure as described in literature favours the paraelectric phase of $BaTiO_3$. Therefore, a new two-step fitting procedure for $BaTiO_3$ including energy differences was proposed. The first step consists in an analytical fit on the short-range forces in particular chosen configuration. In a second step, the separated parametrization of the polarization term is performed by a fit on DFT extracted dipoles and energy differences. This separated fitting procedure could reduce compensation errors between short-range repulsion forces and the polarization term. In addition, the inclusion of the energy differences in the fit may minimize compensation errors between the asymptotic and short-range effects to the induced dipoles. During the application of this modified fitting procedure it has been demonstrated that for an accurate representation of the short-range forces in $BaTiO_3$ asymmetric size effects of the electron cloud with respect to the nucleus are necessary. As such size effects are not included in the polarization ion model, finally compensation errors in the fitting procedure between short-range and long-range interactions are allowed by fitting the set of parameters at the same time. In addition, the fit on the energy surface of the ferroelectric soft mode displacement pattern in [001], [011] and [111] directions has been included in order to better quantify the ferroelectric instabilities in the cubic phase.

Two PIM models based on DIPPIM and DAIM (in the following referred as DAIMO) potential type have been developed. The accuracy of these two models is discussed in the fourth chapter. It has been shown that both models present ferroelectric instabilities in cubic phase. But none of this models describes at the same time accurately the energy curves and stress tensor components associated to the ferroelectric soft mode displacement. Geometry optimization at zero temperature reveals that the DAIMO model reproduces the correct order of relative phase stabilization energies, while the DIPPIM model predicts the tetragonal phase to be the most stable. It has been highlighted, that the erroneous order of phase stabilization with the DIPPIM model is due to the incapability to reproduce the delicate balance between short-range repulsion and long-range forces. Thus, the inclusion of deformability in the DAIMO model helps to reproduce this balance. Finite temperature calculations with the DAIMO model reveals that the rhombohedral phase is stable up to 160K. In the range of temperature between 160K and 210K strong fluctuations in polarization density and cell parameters are observed and no well-defined phase can be distinguished. From 210K on, the average paraelectric cubic phase is reached.

General prospects The potential developed in this work is able to reproduce at least the ferroelectric rhombohedral phase. Therefore, this potential can be envisaged for example to be applied to the investigation of polarization at the surface of rhombohedral $BaTiO_3$ slabs and for the study of the effect of oxygen vacancies in rhombohedral phase. Furthermore, in order to identify the origin of the impossibility of stabilization of the orthorhombic and tetragonal phase further studies would be necessary. In addition, it could be imagined to introduce asymmetric size effects of the electron cloud with respect to the nucleus in the Polarizable Ion Model, by correcting the distance at which Pauli repulsion forces between ions occurs.

Appendix A

Conclusion et perspectives

Les composés à base de matériaux ferroélectriques possèdent un grand nombre de propriétés exceptionnelles intéressantes tant d'un point de vue fondamental qu'industriel. Le coeur de cette thèse est le développement d'un modèle d'ions polarisables pour le prototype ferroélectrique $BaTiO_3$.

Dans son premier chapitre, les trois techniques de calcul des ferroélectriques les plus courantes ont été exposées : La théorie de la fonctionnelle de la densité (DFT), l'approche des Hamiltoniens effectifs et le modèle Shell. La discussion sur ces techniques met en évidence les points suivants : Même si le coût de calcul élevé de la DFT la limite en général à des systèmes de petite taille, à température nulle et sur des temps de calculs courts, elle permet de déterminer avec grande précision plusieurs propriétés ferroélectriques à l'échelle atomique, même quand des mesures expérimentales ne sont pas disponibles. Cela en fait un outil intéressant pour dériver d'autres modèles qui, eux, pourront élargir son champ d'action à des systèmes plus grands, des températures finies et des calculs plus longs. En effet, des Hamiltoniens effectifs et des modèles Shell, issus de la DFT, ont pu simuler correctement la séquence de transition de phase, et il a ainsi pu être démontré que la surface d'énergie à zéro Kelvin obtenue avec la DFT inclue les ingrédients nécessaires à l'obtention des propriétés ferroélectriques à température finie. Néanmoins, l'approche des Hamiltoniens effectifs et le modèle Shell présentent tous deux des restrictions les rendant difficilement applicables à l'étude des défauts et des effets de surface. Ces constatations appuient la volonté de développer une nouvelle famille de potentiels d'interaction basée sur le modèle d'ions polarisables (PIM) et entièrement dérivée des calculs DFT, mais dans le but de simuler plus facilement des systèmes complexes à base de matériaux ferroélectriques, grâce à l'utilisation des ions avec des charges nominales.

Dans le deuxième chapitre le modèle d'ions polarisables (PIM) est présenté. Une attention particulière a été accordée à l'importance d'une description précise des effets de polarisation dans les oxydes ioniques. L'avantage du PIM est que des effets à plusieurs corps sur les dipôles induits sont inclus. Ensuite, la méthodologie de paramétrisation des PIMs utilisée dans la littérature a été présentée au moyen de quelques exemples représentatifs. La discussion sur les PIMs souligne que ce type de modèle convient aux oxydes de métaux alcalino-terreux simples et est capable de reproduire quantitativement la transition de phase complexe sous pression de BaO et permet de fournir des informations sur le mécanisme de transition de phase au niveau atomique. En outre, un exemple issu de la littérature pour le composé TiO_2 a été réexaminé. Pour celui-ci le PIM n'a pas été en mesure de reproduire l'ordre correct des énergies de stabilisations entre ces différentes phases. Cela a permis de souligner que la reproduction de la séquence de transitions de phase se révèle être une tâche difficile pour des systèmes avec de petites différences d'énergie entre les phases de l'ordre de quelques meV par unité de formule chimique.

Le développement d'un modèle d'ions polarisables a fait l'objet du troisième chapitre. Dans la première section de ce dernier, un test de convergence a été réalisé pour l'identification des paramètres techniques pour les calcul DFT en utilisant PBEsol comme approximation de la fonctionnelle d'échange-corrélation telle qu'elle est mise en oeuvre dans VASP. Puis plusieurs propriétés ont été calculées à température nulle et comparées aux valeurs expérimentales et théoriques. Les calculs DFT avec PBEsol reproduisent correctement l'ordre des énergies de stabilisation relatives entre les phases, les propriétés structurales et les modes phonon ferroélectriques. Par conséquent, l'approximation PBEsol semble être adaptée pour la paramétrisation d'un PIM pour $BaTiO_3$. Une des principales motivations de la modélisation avec PIM est d'utiliser des ions avec des charges nominales pour être plus transférable. De plus dans le PIM ces ions sont considérés comme polarisables jusqu'à l'ordre dipolaire. Il est connu qu'une description purement ionique avec des charges nominales de $BaTiO_3$ conduirait à une structure idéale pérovskite présentant un comportement paraélectrique. En conséquence, il a été fait l'hypothèse que le comportement ferroélectrique dans le PIM ne peut être atteint que par la polarisabilité des ions. Cette hypothèse a été testée dans la section qui suit. Plusieurs quantités clés ont été calculées via l'utilisation des ions polarisables avec des charges nominales. Cette étude a conduit à la conclusion que l'erreur introduite par la simplification du système en application de cette hypothèse est acceptable et du même ordre que le modèle Shell, qui en contraste avec le PIM comprend un transfert de charge statique. Dans la deuxième partie du chapitre, il a été révélé que la procédure de paramétrisation telle qu'elle est décrite dans la littérature favorise la phase paraélectrique de $BaTiO_3$. Une nouvelle procédure d'ajustement en deux étapes a été proposée pour $BaTiO_3$ incluant les différences d'énergie. La première étape consiste á un ajustement analytique sur les forces à courte portée dans des configuration particulières. La deuxième étape constitue la paramétrisation du terme de polarisation effectuée par un ajustement sur les dipôles extraits des calculs DFT et les différences d'énergie. Cette procédure d'ajustement séparée pourrait réduire d'éventuelles erreurs de compensation entre les forces de répulsion à courte portée et le terme de polarisation. En outre, l'inclusion des différences d'énergie dans l'ajustement peut minimiser les erreurs de compensation entre la contribution asymptotique et la contribution due aux effets à courte portée dans les dipôles induits. Lors de l'application de cette procédure d'ajustement, il a été trouvé que pour une représentation exacte des forces dans $BaTiO_3$, une modélisation des effets de taille du nuage d'électrons, asymétrique par rapport au noyau, est nécessaire. Enfin, étant donné que de tels effets ne sont pas inclus dans le PIM, des erreurs de compensation dans la procédure d'ajustement entre courte portée et les interactions à longue portée sont autorisées en ajustant simultanément l'ensemble des paramètres. En outre, l'ajustement sur la surface d'énergie liée au mode phonon ferroélectrique dans les directions [001], [011] et [111] a été inclus afin de mieux quantifier les instabilités ferroélectriques dans la phase cubique.

Deux modèles PIM de type DIPPIM et DAIM (nommé par la suite DAIMO) ont été développés. L'évaluation de leur précision fait l'objet du quatrième chapitre. Il a été montré que ces deux modèles présentent les instabilités caractéristiques ferroélectriques dans la phase cubique. L'optimisation de la géométrie à température nulle révèle que le modèle DAIMO reproduit l'ordre correct des énergies de stabilisation relatives entre les phases, tandis que le modèle DIPPIM prédit que la phase tétragonale sera la plus stable. Il a été relevé que l'ordre erroné de la stabilisation des phases avec le DIPPIM est dû à l'incapacité de reproduire l'équilibre délicat entre répulsion à courte portée et forces à longue portée. C'est l'inclusion de la déformabilité dans le DAIMO qui aide à reproduire cet équilibre. Les calculs à température finie avec le modèle DAIMO révèlent que la phase rhomboédrique sera stable jusqu'à 160 K. Dans la gamme de température allant de 160 K à 210 K, de fortes fluctuations de la polarisation et des paramètres de maille sont observées bien qu'aucune phase bien définie ne puisse être distinguée. C'est à partir de 210 K que la phase cubique paraélectrique est obtenue.

Perspectives générales Le potentiel développé dans ce travail est capable de reproduire au moins la phase rhomboédrique ferroélectrique. Par conséquent, ce potentiel peut être envisagé par exemple pour l'étude de la polarisation à la surface de dalles $BaTiO_3$ rhomboédriques ainsi que pour l'étude de l'effet des lacunes d'oxygène dans la phase rhomboédrique. En outre, afin d'identifier l'origine de l'impossibilité de la stabilité de la phase orthorhombique et de la phase tétragonale des investigations supplémentaires seront nécessaires. De plus, on pourrait imaginer introduire des effets de taille du nuage électronique, asymétrique par rapport au noyau, dans le modèle d'ions polarisables en corrigeant la distance à laquelle les forces de répulsion de Pauli entre les ions se produit.

Bibliography

[1] D. I. Bilc et al. "Hybrid exchange-correlation functional for accurate prediction of the electronic and structural properties of ferroelectric oxides". In: *Phys. Rev. B* 77 (16 2008), p. 165107.

[2] Aliaksandr V. Krukau et al. "Influence of the exchange screening parameter on the performance of screened hybrid functionals". In: *The Journal of Chemical Physics* 125.22 (2006), p. 224106. eprint: `http://dx.doi.org/10.1063/1.2404663`.

[3] F. James and M. Roos. "Minuit - a system for function minimization and analysis of the parameter errors and correlations". In: *Computer Physics Communications* 10.6 (1975), pp. 343 –367. ISSN: 0010-4655.

[4] John P. Perdew, Matthias Ernzerhof, and Kieron Burke. "Rationale for mixing exact exchange with density functional approximations". In: *The Journal of Chemical Physics* 105.22 (1996), pp. 9982–9985. eprint: `https://doi.org/10.1063/1.472933`.

[5] M. Born and R. Oppenheimer. "Zur Quantentheorie der Molekeln". In: *Annalen der Physik* 389.20 (1927), pp. 457–484. ISSN: 1521-3889.

[6] P. Hohenberg and W. Kohn. "Inhomogeneous Electron Gas". In: *Phys. Rev.* 136 (3B 1964), B864–B871.

[7] W. Kohn and L. J. Sham. "Self-Consistent Equations Including Exchange and Correlation Effects". In: *Phys. Rev.* 140 (4A 1965), A1133–A1138.

[8] R. P. Feynman. "Forces in Molecules". In: *Phys. Rev.* 56 (4 1939), pp. 340–343.

[9] Mathieu Salanne. "Modelisation atomique de sels fondus fluores a haute temperature." In: *PhD thesis, UNIVERSITÃĽ PARIS VI* (2006).

[10] D. M. Ceperley and B. J. Alder. "Ground State of the Electron Gas by a Stochastic Method". In: *Phys. Rev. Lett.* 45 (7 1980), pp. 566–569.

[11] John P. Perdew, Kieron Burke, and Matthias Ernzerhof. "Generalized Gradient Approximation Made Simple". In: *Phys. Rev. Lett.* 77 (18 1996), pp. 3865–3868.

[12] John P. Perdew et al. “Restoring the Density-Gradient Expansion for Exchange in Solids and Surfaces”. In: *Phys. Rev. Lett.* 100 (13 2008), p. 136406.

[13] Zhigang Wu and R. E. Cohen. “More accurate generalized gradient approximation for solids”. In: *Phys. Rev. B* 73 (23 2006), p. 235116.

[14] M. Shishkin, M. Marsman, and G. Kresse. “Accurate Quasiparticle Spectra from Self-Consistent GW Calculations with Vertex Corrections”. In: *Phys. Rev. Lett.* 99 (24 2007), p. 246403.

[15] P. J. Stephens et al. “Ab Initio Calculation of Vibrational Absorption and Circular Dichroism Spectra Using Density Functional Force Fields”. In: *The Journal of Physical Chemistry* 98.45 (1994), pp. 11623–11627. eprint: `http://dx.doi.org/10.1021/j100096a001`.

[16] Jochen Heyd, Gustavo E. Scuseria, and Matthias Ernzerhof. “Hybrid functionals based on a screened Coulomb potential”. In: *The Journal of Chemical Physics* 118.18 (2003), pp. 8207–8215. eprint: `http://dx.doi.org/10.1063/1.1564060`.

[17] R. E. Cohen and H. Krakauer. “Lattice dynamics and origin of ferroelectricity in $\mathrm{BaTiO_3}$: Linearized-augmented-plane-wave total-energy calculations”. In: *Phys. Rev. B* 42 (10 1990), pp. 6416–6423.

[18] Ronald E. Cohen and Henry Krakauer. “Electronic structure studies of the differences in ferroelectric behavior of batio3 and PbTiO3”. In: *Ferroelectrics* 136.1 (1992), pp. 65–83.

[19] D. J. Singh and L. L. Boyer. “First principles analysis of vibrational modes in KNbO3”. In: *Ferroelectrics* 136.1 (1992), pp. 95–103. eprint: `http://dx.doi.org/10.1080/00150199208016069`.

[20] R. D. King-Smith and David Vanderbilt. “Theory of polarization of crystalline solids”. In: *Phys. Rev. B* 47 (3 1993), pp. 1651–1654.

[21] David Vanderbilt and R. D. King-Smith. “Electric polarization as a bulk quantity and its relation to surface charge”. In: *Phys. Rev. B* 48 (7 1993), pp. 4442–4455.

[22] W. Zhong, R. D. King-Smith, and David Vanderbilt. “Giant LO-TO splittings in perovskite ferroelectrics”. In: *Phys. Rev. Lett.* 72 (22 1994), pp. 3618–3621.

[23] Cohen Ronald E. Fu Huaxiang. “Polarization rotation mechanism for ultrahigh electromechanical response in single-crystal piezoelectrics”. In: *Nature* 403 (2000), pp. 1651–1654.

[24] Ronald E. Cohen. “Surface effects in ferroelectrics: Periodic slab computations for BaTiO3”. In: *Ferroelectrics* 194.1 (1997), pp. 323–342. eprint: `http://dx.doi.org/10.1080/00150199708016102`.

[25] Jorge Padilla and David Vanderbilt. “Ab initio study of BaTiO 3 surfaces”. In: *Physical Review B* 56.3 (1997), p. 1625.

[26] B. Meyer and David Vanderbilt. “Ab initio”. In: *Phys. Rev. B* 63 (20 2001), p. 205426.

[27] Ph. Ghosez, X. Gonze, and J.-P. Michenaud. “Coulomb interaction and ferroelectric instability of BaTiO3”. In: *EPL (Europhysics Letters)* 33.9 (1996), p. 713.

[28] Roman Wahl, Doris Vogtenhuber, and Georg Kresse. “$SrTiO_3$”. In: *Phys. Rev. B* 78 (10 2008), p. 104116.

[29] S Piskunov et al. “Bulk properties and electronic structure of SrTiO3, BaTiO3, PbTiO3 perovskites: an ab initio HF/DFT study”. In: *Computational Materials Science* 29.2 (2004), pp. 165 –178. ISSN: 0927-0256.

[30] S. Tinte et al. “Applications of the generalized gradient approximation to ferroelectric perovskites”. In: *Phys. Rev. B* 58 (18 1998), pp. 11959–11963.

[31] Ph. Ghosez, X. Gonze, and J.-P. Michenaud. “Ferroelectrics and Related Substances”. In: *edited by K. H. Hellwege and A. M. Hellwege, Landolt-BÃűrnstein* New Series, Group III, Vol. 3,Springer-Verlag, Berlin (1996).

[32] Lixin Cao, E. Sozontov, and J. Zegenhagen. “Cubic to Tetragonal Phase Transition of SrTiO3 under Epitaxial Stress: An X-Ray Backscattering Study”. In: *physica status solidi (a)* 181.2 (2000), pp. 387–404. ISSN: 1521-396X.

[33] Y Luspin, J L Servoin, and F Gervais. “Soft mode spectroscopy in barium titanate”. In: *Journal of Physics C: Solid State Physics* 13.19 (1980), p. 3761.

[34] W. Zhong, David Vanderbilt, and K. M. Rabe. “Phase Transitions in $BaTiO_3$ from First Principles”. In: *Phys. Rev. Lett.* 73 (13 1994), pp. 1861–1864.

[35] W. Zhong, David Vanderbilt, and K. M. Rabe. “First-principles theory of ferroelectric phase transitions for perovskites: The case of BaTiO_3”. In: *Phys. Rev. B* 52 (9 1995), pp. 6301–6312.

[36] R.D.King-Smith and David anderbilt. “First-principles investigation of ferroelectricity in perovskite compounds”. In: *Phys. Rev. B* 49 (9 1994), p. 5828.

[37] Silvia Tinte et al. “Quantitative analysis of the first-principles effective Hamiltonian approach to ferroelectric perovskites”. In: *Phys. Rev. B* 67 (6 2003), p. 064106.

[38] J. Padilla, W. Zhong, and David Vanderbilt. “First-principles investigation of 180 domain walls in BaTiO3”. In: *Phys. Rev. B* 53 (10 1996), R5969–R5973.

[39] L. Bellaiche, Alberto García, and David Vanderbilt. “Finite-Temperature Properties of PbZrTiO3 Alloys from First Principles”. In: *Phys. Rev. Lett.* 84 (23 2000), pp. 5427–5430.

[40] Emad Almahmoud et al. “Properties of $\mathrm{Pb(Zr,Ti)O_3}$ ultrathin films under stress-free and open-circuit electrical boundary conditions”. In: *Phys. Rev. B* 70 (22 2004), p. 220102.

[41] Igor A. Kornev, Huaxiang Fu, and Laurent Bellaiche. “Properties of ferroelectric ultrathin films from first principles”. In: *Journal of Materials Science* 41.1 (2006), pp. 137–145. ISSN: 1573-4803.

[42] Ivan Naumov, L Bellaiche, and Huaxiang Fu. “Unusual Phase Transition in Ferroelectric Nanodisks and Nanorods”. In: 432 (Mar. 2005), pp. 737–40.

[43] Ivan Naumov and Huaxiang Fu. “Spontaneous Polarization in One - Dimensional Pb(ZrTi)O3 Nanowires”. In: 95 (Jan. 2006), p. 247602.

[44] Huaxiang Fu and L. Bellaiche. “Ferroelectricity in Barium Titanate Quantum Dots and Wires”. In: *Phys. Rev. Lett.* 91 (25 2003), p. 257601.

[45] Kenny B. Lipkowitz and Donald B. Boyd. “Reviews in Computational Chemistry Volume 18”. In: (2002).

[46] S Tinte et al. “Atomistic modelling of BaTiO 3 based on first-principles calculations”. In: *Journal of Physics: Condensed Matter* 11.48 (1999), p. 9679.

[47] M. Sepliarsky et al. “Atomic-level simulation of ferroelectricity in perovskite solid solutions”. In: *Applied Physics Letters* 76.26 (2000), pp. 3986–3988. eprint: `http://dx.doi.org/10.1063/1.126843`.

[48] S Tinte et al. “Ferroelectric properties of Ba x Sr 1âĹŠ x TiO 3 solid solutions obtained by molecular dynamics simulation”. In: *Journal of Physics: Condensed Matter* 16.20 (2004), p. 3495.

[49] J. M. Vielma and G. Schneider. “Shell model of BaTiO3 derived from ab-initio total energy calculations”. In: *Journal of Applied Physics* 114.17 (2013), p. 174108. eprint: `http://dx.doi.org/10.1063/1.4827475`.

[50] M. Sepliarsky et al. “Ferroelectric phase transitions and dynamical behavior in KNbO3/KTaO3 superlattices by molecular-dynamics simulation”. In: *Journal of Applied Physics* 91.5 (2002), pp. 3165–3171. eprint: `http://dx.doi.org/10.1063/1.1435826`.

[51] M. Sepliarsky et al. "Long-ranged ferroelectric interactions in perovskite superlattices". In: *Phys. Rev. B* 64 (6 2001), p. 060101.

[52] H.-M. Christen et al. "Long-range ferroelectric interactions in KTaO3/KNbO3 superlattice structures". In: *Applied Physics Letters* 72.20 (1998), pp. 2535–2537. eprint: `http://dx.doi.org/10.1063/1.121411`.

[53] A. Asthagiri et al. "Advances in First-Principles Studies of Transducer Materials". In: *Ferroelectrics* 333.1 (2006), pp. 69–78. eprint: `http://dx.doi.org/10.1080/00150190600695750`.

[54] V. Ravikumar, D. Wolf, and V. P. Dravid. "Ferroelectric-Monolayer Reconstruction of the $SrTiO_3$ (100) Surface". In: *Phys. Rev. Lett.* 74 (6 1995), pp. 960–963.

[55] G. Charlton et al. "Surface relaxation of SrTiO3(001)". In: *Surface Science* 457.1-2 (2000), pp. L376 –L380. ISSN: 0039-6028.

[56] J. Padilla and David Vanderbilt. "Ab initio study of SrTiO3 surfaces". In: *Surface Science* 418.1 (1998), pp. 64 –70. ISSN: 0039-6028.

[57] J. Padilla and David Vanderbilt. "Ab initio". In: *Phys. Rev. B* 56 (3 1997), pp. 1625–1631.

[58] S. Tinte and M. G. Stachiotti. "Atomic-level simulation of ferroelectricity in BaTiO3 ultrathin films". In: *Integrated Ferroelectrics* 38.1-4 (2001), pp. 91–100. eprint: `http://dx.doi.org/10.1080/10584580108016921`.

[59] M. Sepliarsky et al. "Polarization reversal in a perovskite ferroelectric by molecular-dynamics simulation". In: *Applied Physics Letters* 79.26 (2001). eprint: `http://dx.doi.org/10.1063/1.1428122`.

[60] S Tinte et al. "Ferroelectric properties of Ba x Sr 1- x TiO 3 solid solutions obtained by molecular dynamics simulation". In: *Journal of Physics: Condensed Matter* 16.20 (2004), p. 3495.

[61] Simon R. Phillpot, Susan B. Sinnott, and Aravind Asthagiri. "Atomic-Level Simulation of Ferroelectricity in Oxides: Current Status and Opportunities". In: *Annual Review of Materials Research* 37.1 (2007), pp. 239–270. eprint: `https://doi.org/10.1146/annurev.matsci.37.052506.084206`.

[62] Samia Faiz Gurmani. "Modeling of mineral-melt interfaces:an atomic scale view on partially molten rocks". In: (2012), p. 33. eprint: `http://d-nb.info/1027308228/34`.

[63] K. T. Tang and J. Peter Toennies. “An improved simple model for the van der Waals potential based on universal damping functions for the dispersion coefficients”. In: *The Journal of Chemical Physics* 80.8 (1984), pp. 3726–3741. eprint: `http://dx.doi.org/10.1063/1.447150`.

[64] Andres Aguado et al. “Multipoles and interaction potentials in ionic materials from planewave-DFT calculations”. In: *Faraday Discuss.* 124 (0 2003), pp. 171–184.

[65] N C Pyper. “A theory of the relative stabilities of the cubic phases ofagnesium and calcium oxides”. In: *Journal of Physics: Condensed Matter* 8.30 (1996), p. 5509.

[66] MARK WILSON. “Many-Body Effects in Ionic Systems”. In: *PhD thesis, Keble College, Oxford* (1994).

[67] P. W. Fowler and P. A. Madden. “In-crystal polarizabilities of alkali and halide ions”. In: *Phys. Rev. B* 29 (2 1984), pp. 1035–1042.

[68] A. D. Buckingham. “Permanent and Induced Molecular Moments and Long-Range Intermolecular Forces”. In: (), pp. 107–142.

[69] Carmen Domene et al. “Short-Range Contributions to the Polarization of Cations”. In: *The Journal of Physical Chemistry A* 105.16 (2001), pp. 4136–4142. eprint: `http://dx.doi.org/10.1021/jp004173m`.

[70] P. W. Fowler and P. A. Madden. “Fluctuating dipoles and polarizabilities in ionic materials: Calculations on LiF”. In: *Phys. Rev. B* 31 (8 1985), pp. 5443–5455.

[71] Patrick Jemmer et al. “Dipole and quadrupole polarization in ionic systems: Ab initio studies”. In: *The Journal of Chemical Physics* 111.5 (1999), pp. 2038–2049. eprint: `http://dx.doi.org/10.1063/1.479472`.

[72] Gilles Leborgne. “Introduction a la methode du gradient conjugue”. In: (2006). eprint: `www.isima.fr/leborgne`.

[73] Daan Frenkel and Berend Smit. *Understanding Molecular Simulation*. 2nd. Orlando, FL, USA: Academic Press, Inc., 2001. ISBN: 0122673514.

[74] P. P. Ewald. “Die Berechnung optischer und elektrostatischer Gitterpotentiale”. In: *Annalen der Physik* 369.3 (1921), pp. 253–287. ISSN: 1521-3889.

[75] Thomas M. Nymand and Per Linse. “Ewald summation and reaction field methods for potentials with atomic charges, dipoles, and polarizabilities”. In: *The Journal of Chemical Physics* 112.14 (2000), pp. 6152–6160. eprint: `http://dx.doi.org/10.1063/1.481216`.

[76] S. W. de Leeuw, J. W. Perram, and E. R. Smith. “Simulation of Electrostatic Systems in Periodic Boundary Conditions. I. Lattice Sums and Dielectric Constants”. In: *Proceedings of the Royal Society of London A: Mathematical, Physical and Engineering Sciences* 373.1752 (1980), pp. 27–56. ISSN: 0080-4630. eprint: `http://rspa.royalsocietypublishing.org/content/373/1752/27.full.pdf`.

[77] AndrÃl’s Aguado and Paul A. Madden. “Ewald summation of electrostatic multipole interactions up to the quadrupolar level”. In: *The Journal of Chemical Physics* 119.14 (2003), pp. 7471–7483. eprint: `http://dx.doi.org/10.1063/1.1605941`.

[78] AndrÃl’s Aguado, Leonardo Bernasconi, and Paul A. Madden. “A transferable interatomic potential for MgO from ab initio molecular dynamics”. In: *Chemical Physics Letters* 356.5 (2002), pp. 437 –444. ISSN: 0009-2614.

[79] Nicola Marzari and David Vanderbilt. “Maximally localized generalized Wannier functions for composite energy bands”. In: *Phys. Rev. B* 56 (20 1997), pp. 12847–12865.

[80] Alfio Lazzaro and Lorenzo Moneta. “MINUIT package parallelization and applications using the RooFit package”. In: *Journal of Physics: Conference Series* 219.4 (2010), p. 042044.

[81] Samuel T. Weir, Yogesh K. Vohra, and Arthur L. Ruoff. “High-pressure phase transitions and the equations of state of BaS and BaO”. In: *Phys. Rev. B* 33 (6 1986), pp. 4221–4226.

[82] Dario Corradini et al. “DFT-based polarizable force field for TiO 2 and SiO 2”. In: *Modelling and Simulation in Materials Science and Engineering* 23.7 (2015), p. 074005.

[83] T. MITSUHASHI and O. J. KLEPPA. “Transformation Enthalpies of the TiO2 Polymorphs”. In: *Journal of the American Ceramic Society* 62.7-8 (1979), pp. 356–357. ISSN: 1551-2916.

[84] Alexandra Navrotsky, John C. Jamieson, and Ole J. Kleppa. "Enthalpy of Transformation of a High-Pressure Polymorph of Titanium Dioxide to the Rutile Modification". In: *Science* 158.3799 (1967), pp. 388–389. ISSN: 0036-8075. eprint: `http://science.sciencemag.org/content/158/3799/388.full.pdf`.

[85] X. J. Han et al. "Polarizable interatomic force field for TiO_2 parametrized using density functional theory". In: *Phys. Rev. B* 81 (13 2010), p. 134108.

[86] M. C. Payne et al. "Iterative minimization techniques for ab initio total-energy calculations: molecular dynamics and conjugate gradients". In: *Rev. Mod. Phys.* 64 (4 1992), pp. 1045–1097.

[87] Matthew D. Segall Chris J. Pickard et al. Clark Stewart J. "First principles methods using CASTEP". In: *Zeitschrift fÃijr Kristallographie - Crystalline Materials.* 220(5/6) (2009), pp. 567–570.

[88] M. Wilson et al. "Molecular dynamics simulations of compressible ions". In: *The Journal of Chemical Physics* 104.20 (1996), pp. 8068–8081. eprint: `http://dx.doi.org/10.1063/1.471523`.

[89] MARK WILSON and PAUL A. MADDEN. "A generic ionic potential for the alkaline-earth oxides and the anomalous crystal structure of ZnO". In: *Molecular Physics* 90.1 (1997), pp. 75–84. eprint: `http://www.tandfonline.com/doi/pdf/10.1080/002689797172886`.

[90] G Peckham. "The phonon dispersion relation for magnesium oxide". In: *Proceedings of the Physical Society* 90.3 (1967), p. 657.

[91] P. E. Blöchl. "Projector augmented-wave method". In: *Phys. Rev. B* 50 (24 1994), pp. 17953–17979.

[92] G. Kresse and D. Joubert. "From ultrasoft pseudopotentials to the projector augmented-wave method". In: *Phys. Rev. B* 59 (3 1999), pp. 1758–1775.

[93] Hendrik J. Monkhorst and James D. Pack. "Special points for Brillouin-zone integrations". In: *Phys. Rev. B* 13 (12 1976), pp. 5188–5192.

[94] Philippe Ghosez. "First-principle study of the dielectric and dynamical properties of barium titanate". In: *PhD thesis, UNIVERSITE CATHOLIQUE DE LOUVAIN* (1997).

[95] G. H. Kwei et al. "Structures of the ferroelectric phases of barium titanate". In: *The Journal of Physical Chemistry* 97.10 (1993), pp. 2368–2377. eprint: `http://dx.doi.org/10.1021/j100112a043`.

[96] H.F. Kay and P. Vousden. “XCV. Symmetry changes in barium titanate at low temperatures and their relation to its ferroelectric properties”. In: *The London, Edinburgh, and Dublin Philosophical Magazine and Journal of Science* 40.309 (1949), pp. 1019–1040. eprint: http://dx.doi.org/10.1080/14786444908561371.

[97] G. Shirane, H. Danner, and R. Pepinsky. “Neutron Diffraction Study of Orthorhombic $BaTiO_3$”. In: *Phys. Rev.* 105 (3 1957), pp. 856–860.

[98] A. W. Hewat. “Structure of rhombohedral ferroelectric barium titanate”. In: *Ferroelectrics* 6.1 (1973), pp. 215–218. eprint: http://dx.doi.org/10.1080/00150197408243970.

[99] Robert A. Evarestov and Andrei V. Bandura. “First-principles calculations on the four phases of BaTiO3”. In: *Journal of Computational Chemistry* 33.11 (2012), pp. 1123–1130. ISSN: 1096-987X.

[100] W. Cochran. “Crystal stability and the theory of ferroelectricity”. In: *Advances in Physics* 9.36 (1960), pp. 387–423. eprint: http://dx.doi.org/10.1080/00018736000101229.

[101] Annette Bussmann-Holder. “The polarizability model for ferroelectricity in perovskite oxides”. In: *Journal of Physics: Condensed Matter* 24.27 (2012).

[102] E.I. Blount. “Formalisms of Band Theory”. In: *Solid State Physics* 13 (1962), pp. 305 –373. ISSN: 0081-1947.

[103] R. D. King-Smith and David Vanderbilt. “Theory of polarization of crystalline solids”. In: *Phys. Rev. B* 47 (3 1993), pp. 1651–1654.

[104] W. Zhong, R. D. King-Smith, and David Vanderbilt. “Giant LO-TO splittings in perovskite ferroelectrics”. In: *Phys. Rev. Lett.* 72 (22 1994), pp. 3618–3621.

[105] J. D. Axe. “Apparent Ionic Charges and Vibrational Eigenmodes of $BaTiO_3$ and Other Perovskites”. In: *Phys. Rev.* 157 (2 1967), pp. 429–435.

[106] Fig.6.2.(b) J. Fallon. *Multiscale theory and simulation of barium titanate.*

[107] J. J. Wang et al. “Lattice, elastic, polarization, and electrostrictive properties of BaTiO3 from first-principles”. In: *Journal of Applied Physics* 108.3 (2010), p. 034107. eprint: http://dx.doi.org/10.1063/1.3462441.

[108] Gen Shirane and Akitsu Takeda. “Transition Energy and Volume Change at Three Transitions in Barium Titanate”. In: *Journal of the Physical Society of Japan* 7.1 (1952), pp. 1–4.

[109] H. H. Wieder. “Electrical Behavior of Barium Titanatge Single Crystals at Low Temperatures”. In: *Phys. Rev.* 99 (4 1955), pp. 1161–1165.

[110] M. Fechner, S. Ostanin, and I. Mertig. “Effect of the surface polarization in polar perovskites studied from first principles”. In: *Phys. Rev. B* 77 (9 2008), p. 094112.

[111] T. Mitsui et al. “Landolt-Bornstein Numerical Data and Functional Relationships in Science and Technology”. In: *Springer Verlag* (1981).

[112] Don Berlincourt and Hans Jaffe. “Elastic and Piezoelectric Coefficients of Single-Crystal Barium Titanate”. In: *Phys. Rev.* 111 (1 1958), pp. 143–148.

[113] Mario Burbano. “Computer modelling of metal oxides, [thesis],Trinity College (Dublin, Ireland). School of Chemistry”. In: (2014), p. 240.

[114] Mary Ann Branch, Thomas F. Coleman, and Yuying Li. “A Subspace, Interior, and Conjugate Gradient Method for Large-Scale Bound-Constrained Minimization Problems”. In: *SIAM Journal on Scientific Computing* 21.1 (1999), pp. 1–23. eprint: `https://doi.org/10.1137/S1064827595289108`.

[115] Dario Marrocchelli et al. “The construction of a reliable potential for GeO2 from first-principles”. In: 107 (Jan. 2010).

[116] Michael J Castiglione, Mark Wilson, and Paul A Madden. “Polarization effects in the simulation of lead (II) fluoride”. In: *Journal of Physics: Condensed Matter* 11.46 (1999), p. 9009.

[117] In: ().

[118] J. A. Nelder and R. Mead. “A Simplex Method for Function Minimization”. In: *The Computer Journal* 7.4 (1965), p. 308.

[119] Eric Jones, Travis Oliphant, Pearu Peterson, et al. *SciPy: Open source scientific tools for Python*. [Online; accessed <today>]. 2001–.

[120] M.I. Aroyo et al. “Crystallography online: Bilbao crystallographic server”. In: *Bulgarian Chemical Communications* 43.2 (2011). cited By 109, pp. 183–197.

[121] C. Kittel. “introduction to solid state physics, Wiley, New York, USA”. In: (1996).

[122] M.P. Allen and D.J. Tildesley. *Computer Simulation of Liquids*. Oxford Science Publ. Clarendon Press, 1989. ISBN: 9780198556459.

[123] William G. Hoover. “Canonical dynamics: Equilibrium phase-space distributions”. In: *Phys. Rev. A* 31 (3 1985), pp. 1695–1697.

[124] Glenn J. Martyna, Michael L. Klein, and Mark Tuckerman. “Nose-Hoover chains: The canonical ensemble via continuous dynamics”. In: *Journal of Chemical Physics* 97.4 (1992), pp. 2635–2643. ISSN: 0021-9606.

université
PARIS-SACLAY

ÉCOLE DOCTORALE
INTERFACES
Approches Interdisciplinaires :
Fondements, Applications et Innovation

Titre : Développement du modèle d'ion polarisable pour la modélisation de $BaTiO_3$

Mots clés : modèle d'ion polarisable, ferroélectriques, échelle nanoscopique

Résumé : Les composés à base de matériaux ferroélectriques présentent un large éventail de propriétés d'un grand intérêt fondamental et industriel. Ils possèdent un couplage entre la polarisation, la contrainte, le champ électrique et la température et trouvent application dans les dispositifs à l'échelle nanométrique. Les ferroélectriques sont aujourd'hui par exemple déjà utilisés dans les condensateurs, les mémoires, les capteurs et les actionneurs. Afin de comprendre la relation entre leurs propriétés physiques exceptionnelles et leur structure, des méthodes numériques capables de simuler à l'échelle nanométrique sont souhaitées. Pour ce faire, le modèle d'ions polarisables (PIM) est appliqué, modèle dans lequel les ions sont considérés comme des espèces polarisables possédant des charges nominales. En regard des techniques de modélisation actuelles, l'utilisation de charges nominales devrait faciliter l'inclusion de diverses compositions et l'étude des défauts et des effets de surface. Les paramètres du PIM sont dérivés par une procédure d'ajustement sur des données de références obtenues par des calculs avec la théorie de la fonctionnelle de la densité (DFT). Pour une première étape vers la modélisation ferroélectrique avec PIM, l'accent est mis sur le développement d'un potentiel d'interaction pour le prototype ferroélectrique $BaTiO_3$. $BaTiO_3$ présente une séquence complexe de transition de phase (rhomboédrique, orthorhombique, tétragonale, cubique) qui est liée à de petites différences d'énergie de l'ordre de quelques meV/unité de formule. Pour cette raison, le développement d'un potentiel d'interaction pour $BaTiO_3$ nécessite une grande précision pour décrire correctement l'équilibre entre les interactions à courte et à longue portée. Il a été démontré au cours de ce travail que des effets asymétriques du nuage d'électrons par rapport au noyau seraient nécessaires pour une représentation précise des forces à courte portée. Puisque de tels effets ne sont pas inclus dans le PIM, des erreurs de compensation dans la procédure d'ajustement entre les interactions à courte et à longue portée sont permises afin d'obtenir le meilleur ajustement global. Le PIM développé pour $BaTiO_3$ reproduit plusieurs propriétés à température nulle. À température finie, le PIM prédit que la phase rhomboédrique sera stable jusqu'à 160K. Dans la plage de température comprise entre 160K et 210K, de fortes fluctuations de la polarisation et des paramètres de maille sont observées et aucune phase bien définie ne peut être distinguée. A partir de 210K, la phase cubique paraélectrique est atteinte. Le modèle PIM développé dans cette thèse peut être appliqué à des études à basse température dans la phase ferroélectrique rhomboédrique. Il peut donc être utilisé pour étudier les effets de surface ou des lacunes d'oxygène dans la phase rhomboédrique de $BaTiO_3$.

Title : Development of a polarizable ion model for barium titanate ($BaTiO_3$)

Keywords : polarizable ion model, ferroelectric, nanoscale

Abstract : Ferroelectric based compounds present a wide range of properties which are from great fundamental and industrial interest on nanoscale. Ferroelectric based compounds possesses strong coupling between polarization, stress, electric field and temperature and are nowadays already used in capacitors, memories, sensors, and actuators. In order to understand the relationship between microstructure and the outstanding properties, numerical methods able to simulate at nanoscale are disired.

For this propose, the Polarizable Ion Model (PIM) is employed that treats the ions as polarizable species with nominal charge. In comparison to current modelisation techniques, the use of nominal charges should facilitate the inclusion of various materials composition and the study of defect and surface effects. The pametrization of the model is derived by a fit on *ab initio* DFT reference calculations. For a first step towards ferroelectric modelling with PIM, the focus lies on the developpment of an interaction potential for the prototyp ferroelectric $BaTiO_3$. $BaTiO_3$ presents a complex phase transition sequence (rhombohedral, orthorhombic, tetragonal, cubic) that is related to small energy differences of the order of some meV/formula unit. Thus, the development of a reliable interaction potential requires high precision and a correct description of the balance between short range and long range interactions. It has been demonstrated during this work that for an accurate representation of the short range forces asymmetric size effects of the electron cloud with respect to the nucleus would be necessary. As such size effects are not included in the PIM, compensation errors in the fitting procedure between short range and long range interactions are allowed in order to obtain the best global fit. The developed PIM model reproduces several zero temperature properties of $BaTiO_3$. At finite temperature the PIM predicts the rhombohedral phase to be stable up to 160K. In the temperature range between 160K and 210K strong fluctuations in polarization and cell parameters are observed and no well-defined phase can be distinguished. From 210K on, the average paraelectric cubic phase is reached.

Université Paris-Saclay
Espace Technologique / Immeuble Discovery
Route de l'Orme aux Merisiers RD 128 / 91190 Saint-Aubin, France